DOI: 10.1002/ ((please add manuscript number))

Article type: Review

Broadband Metamaterial Absorber

Peng Yu^{1,5}, Lucas V. Besteiro^{1,2}, Yongjun Huang⁴, Jiang Wu¹, Lan Fu⁵, Hark H. Tan⁵, Chennupati Jagadish⁵,

Gary P. Wiederrecht⁶, Zhiming Wang^{1,*}, Alexander O. Govorov^{3,*}

¹Institute of Fundamental and Frontier Science, University of Electronic Science and

Technology of China, Chengdu 610054, P. R. China.

²Institut National de la Recherche Scientifique – Énergie, Materiaux Télécommunications,

Varennes J3X 1S2, Québec, Canada

³Department of Physics and Astronomy, Ohio University, Athens, OH 45701, USA

⁴School of Information and Communication Engineering, University of Electronic Science

and Technology of China, Chengdu 611731, P.R. China

⁵Department of Electronic Materials and Engineering, Research School of Physics and

Engineering, The Australian National University, Canberra, ACT 0200, Australia

⁶Center for Nanoscale Materials, Argonne National Laboratory, Lemont, IL 60439, USA.

*Corresponding author: zhmwang@uestc.edu.cn; govorov@ohio.edu

Keywords: metamaterial, absorber, broadband, photovoltaic, metasurface

The recent rise of metamaterials opens new opportunities for absorbers due to their designed

electrodynamic properties and effects, allowing the creation of materials with effective values of

permittivity and permeability that are not available in naturally occurring materials. Since their first

experimental demonstration in 2008, recent literature has offered great advances in metamaterial

perfect absorber (MMPA) operating at frequencies from radio to optical. Broadband absorbers are

indispensable in thermophotovoltaic, photodetection, bolometry and manipulation of mechanical

1

resonances. Although it is easy to obtain MMPA with single band or above, achieving broadband MMPA (BMMPA) remains a challenge due to the intrinsically narrow bandwidth of surface plasmon polaritons, localized surface plasmon resonances generated on metallic surfaces at nanoscale or high *Q*-factor in GHz region. To guide future development of BMMPA, we review the recent progress in the field: methods to create broadband absorption and their potential applications. The four mainstream methods to achieve BMMPA are introduced, including planar and vertical element arrangements, their welding with lumped elements and the use of plasmonic nanocomposites, accompanied by description of other, less common approaches. Following this, applications of BMMPA—solar photovoltaics, photodetection, bolometry and manipulation of mechanical resonances, are reviewed. Finally, challenges and prospects are discussed.

1. Introduction

Artificially-engineered materials, so-called metamaterials (MMs), demonstrate interesting electrodynamic properties, including negative refractive index,^[1] electromagnetic (EM) wave cloaking^[2] and inverse Doppler effect,^[3] that are not found in naturally occurring materials. By engineering this composite structured materials, MMs can be viewed as homogeneous mediums with an effective permittivity and permeability.^[4] As a particular subtype, MMs can be utilized as perfect absorbers, resulting in near unity absorbance over a small or a broad frequency band, while it can be crafted to overcome the thickness limitation of traditional quarter wavelength devices.^[5,6] The thickness of a metamaterial perfect absorber (MMPA) can be about ~25 times smaller than the resonance wavelength thickness of functional layers much smaller than their counterparts.^[7] The MMPA, coupled with the strong growth of its applications, has provided motivation for further development. Figure 1 summarizes some important publications in this field from 2008 to middle of 2017. Landy *et al.* first demonstrated a MMPA in the microwave regime utilizing a 2D MM electric ring resonator (ERR), in which electric and magnetic resonances match the impedance of free space, thus eliminating the reflection at the targeted wavelength.^[5] This seminal work has sparked research to extend the MMPA concept to other frequency regimes and to a variety of applications.

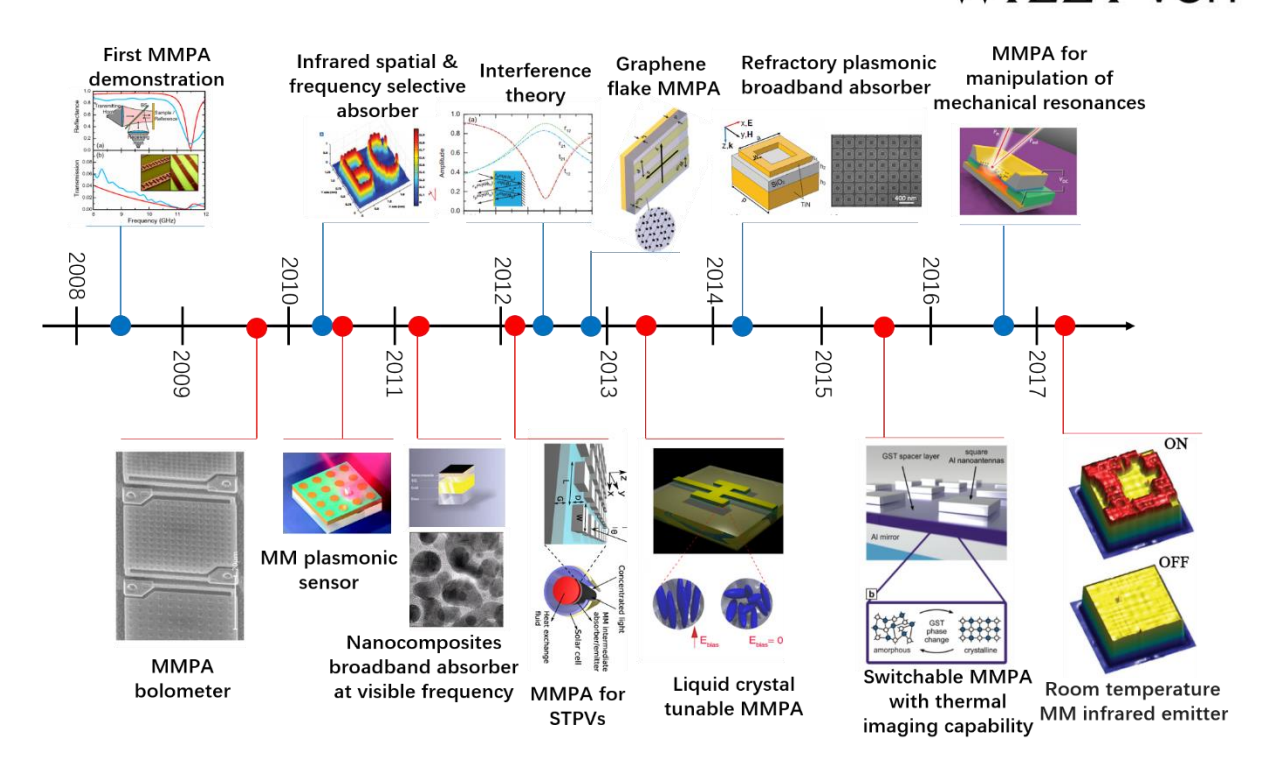


Figure 1. Selected representative publications on MMPA from 2008 to the middle of 2017. The publications are from Ref. [5, 8-17, 18], respectively along the time axis.

Since the first demonstration of MMPA,^[5] the advent of MMs has spawned extensive research into MMPAs over the last decade working from radio to optical spectrum range.^[19, 20-22] MMPAs have been demonstrated in applications, such as solar energy harvesting,^[6, 23, 24] biological sensing,^[10, 25, 26] thermophotovoltaics,^[12, 27] photodetection,^[28-30] creation of imaging devices,^[9, 20, 31] absorption filtering,^[32] etc. For practical applications, the MMPAs can be divided into two types: narrowband and broadband. Although MMPAs with customized single-band,^[5, 33, 34] dual-band,^[22, 35, 36] triple-band^[37] and more^[38, 39] have demonstrated discrete absorption peaks, broadband absorbers attract much interest in both civilian and military applications, such as photovoltaics (PV), bolometry, photodetection, stealth technology and mechanical manipulation, etc. Unfortunately, achieving broadband absorption, especially in the THz region (and higher frequencies), still remains a challenging task because the intrinsically narrow bandwidth of surface plasmon polaritons (SPPs) or localized surface plasmon resonances (LSPRs) generated on metallic surfaces at the nanoscale, which are exploited as a mechanism to obtain perfect absorption.^[40] In GHz or lower frequencies, the resonant

Q-factor is relatively high due to a small gap between resonators and back metallic film, from which results a narrow bandwidth. [50] Therefore, with a simple design, perfect absorption can be easily achieved at a single wavelength, but the design becomes complicated and difficult for absorbers with perfect absorption while achieving broadband absorption. Substantial progress has been made in developing broadband metamaterial perfect absorbers (BMMPAs), but the field remains immature. Previous reviews on metamaterial absorbers are mainly focused on absorbers working at different frequencies ranges; [41, 42] Watts et al. reviewed the theory behind perfect absorbers, along with details about their simulation and fabrication, and briefly discussed the applications of absorbers, including selective thermal emitters and spectrally sensitive detectors or sensors, but they do not put an emphasis on broadband metamaterials and their applications.^[7] Zhao et al. reviewed BMMPAs fabricated by adding multiple resonators and dendritic structures in an unit cell. [43] In order to provide a guide for future development, this review comprehensively focuses on a critique of the work in progress and applications of BMMPA. First, we review mainstream methods, by introducing BMMPA structures with planar and vertical resonators, lumped elements and plasmonic nanocomposites and followed by some unconventional methods to fabricate BMMPA, such as using complementary metamaterial (CMM) structures, space-filling, dielectric tailoring, cross-trapezoid resonators and resonator material tailoring. Subsequently, we review some key applications of the BMMPA, such as PV energy harvesting, photodetection, bolometer and manipulation of mechanical resonances. Finally, challenges and prospects of BMMPA will be discussed.

2. Typical structure for BMMPA

MMPAs are usually composed of three layers: the periodically-arranged metallic pattern, a dielectric spacer layer and a continuous metallic plate. The first patterned layer is critical in MMPA design because it can be tuned to fulfil the impedance-matching condition with the environment, achieving zero reflection at resonant frequencies; the second dielectric layer is a spacer used to dissipate the EM wave; the metallic ground layer blocks all incident EM waves. The perfect absorption can be theoretically described using effective-medium approximation, [44] equivalent circuit theory, [45] or

interference theory^[13, 46]—these are comprehensively reviewed in Ref.^[7, 41, 47]. The dominant mechanism of absorption is either dielectric loss in the second layer or Ohmic loss in the top pattern. In the case of Ohmic loss, the *Q*-factor is reduced due to an increase of the bandwidth of the absorption peak, a key consideration for devising BMMPA.^[41] A broadband response means that the device is able to absorb the entire EM frequencies that are illuminating the MMPA surface. In order to achieve panchromatic solar energy conversion, for instance, BMMPA is essential for light trapping in the solar cells.^[48]

So far, researchers have experimentally and computationally demonstrated four main techniques to realize BMMPAs. One method creates multiple resonances in each unit cell via tailoring the size of the patterns on the top layer (planar arrangement), as shown in figure 2(a). Multiple resonances will appear and by incorporating them into a unit cell and perfect absorptivity can be achieved. Specifically, if these resonances are close enough, they will superpose with each other to form broadband absorption. It is worth noting that although the interaction from neighbouring cells has a shifting effect on the resonant frequency, the coupling strength is extremely weak. [49] The second method to yield a broadband absorption is to stack multiple top layers in the vertical direction (vertical arrangement), as demonstrated in figure 2(b). One can use different dielectrics and metals as an individual bilayer and finally stack these bilayers to form an unabated broadband absorption spectrum by tuning the geometrical parameters simultaneously. Figure 2(c) illustrates the third approach to design BMMPA: by introducing lumped elements such as resistances, capacitances and diodes. The lumped elements they are welded to connect the different resonant modes together and consume EM energy—reduce the Q-factor. [50] In the fourth method, the metal-dielectric nanocomposites take advantage of the LSPR from metallic nanoparticles (NPs), as illustrated in figure 2(d). The metal-dielectric nanocomposite systems provide impedance matching of the medium to free space, multi-reflection of light between the layers and light trapping and absorption by NPs, realizing perfect light absorption covering from UV to NIR. In this section, we will describe four mainstream pathways to realize BMMPA, illustrated in

figure 2. Besides, less common methods are also reviewed, including CMM structures, space-filling, dielectric material tailoring, crossed trapezoidal resonators and material tailoring of top resonators.

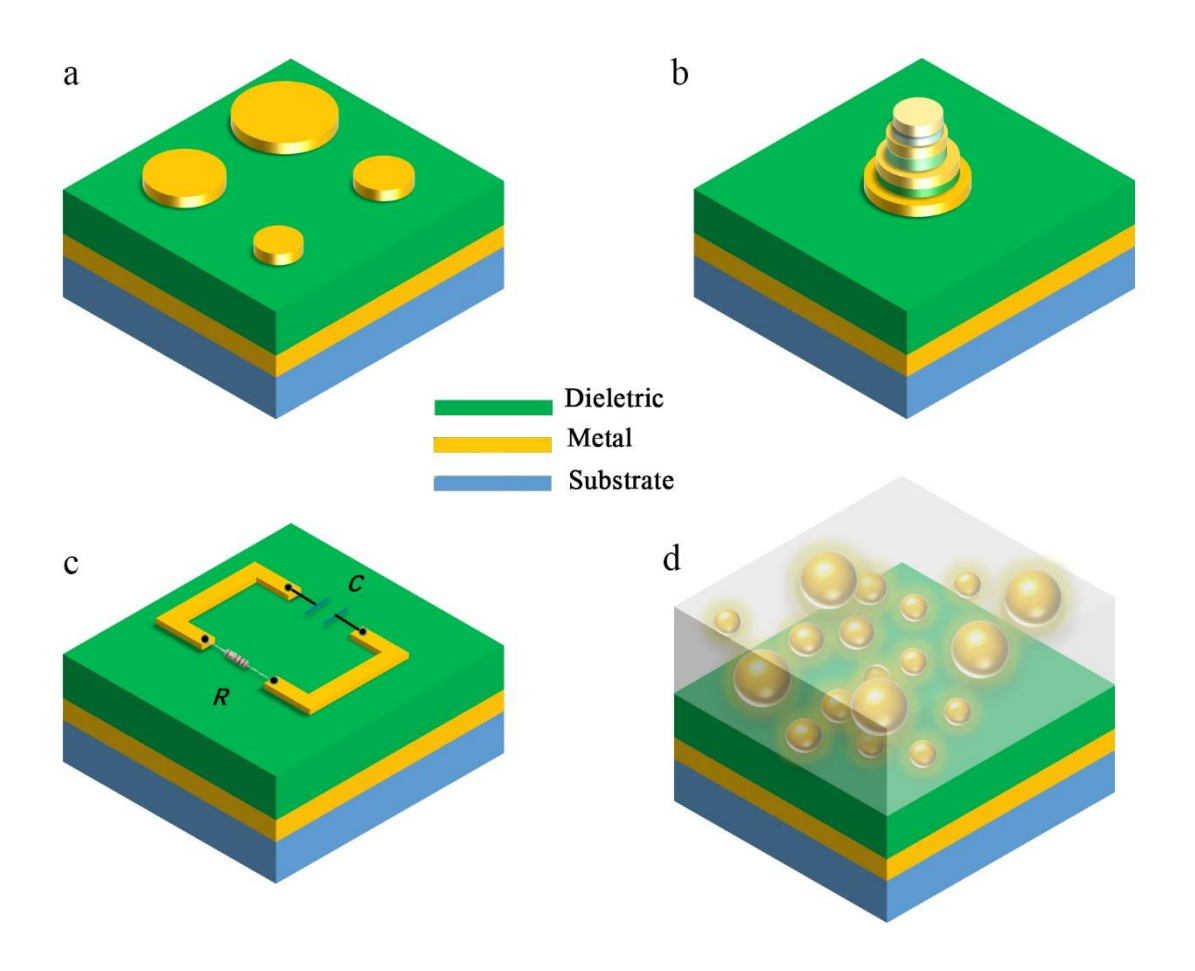


Figure 2. Conventional designs for BMMPAs. (a) Planar arrangement; (b) Vertical arrangement; (c) Welded with lumped elements; (d) Nanocomposites.

The prerequisite of BMMPA design is to provide multiple absorption bands. Therefore, it should be considered before realizing actual broadband absorption. Besides, higher order harmonics of a single resonance structure, [36] extraordinary optical transmission, [51] CMM structure [35] and Fabry-Perot-type cavity resonance in the dielectric [52] can be leveraged to achieve dual-band absorption and thus potential for BMMPA. Our previous work demonstrated that the snowflake-shaped MMPA shows multiband perfect absorption. [53] Therefore, recreating shapes found in nature with metals can also provide multiband perfect absorption, such as binary trees, [54,55] flowers [56] and leaves. [57] Based on the following discussion, we compose **table 1** to summarize the choice of metals and dielectrics in designing BMMPAs; only a few representative references are cited in the table.



Table 1 Metal and dielectric choice in BMMPA design

Metal		Dielectric	
Ag	[24, 26]	Ge [39, 78]	
Au	[6, 9, 10, 21, 29, 39, 58, 59]	Si [30]	
Cu	[37, 60, 61]	SiC [79]	
Al	[62]	ZnS [39, 80]	
Мо	[35]	FR-4 [37, 50, 54, 61, 81, 82]	
W	[63]	SiN [18] [83]	
Ti	[64]	GaAs [39]	
Pd	[65]	SiO ₂ [11, 35, 58, 60, 84]	
Cr	[66, 67]	Al ₂ O ₃ [6, 9]	
Ni	[68]	MgF ₂ [10, 29, 73]	
Та	[68]	Water [85]	
ITO	[69]	TMM4 [86]	
TiN	[16]	Kapton [21]	
AZO	[68]	Epoxy glass [87]	
Ta_2N_3	[70]	Polyimide [88] [59, 62, 89]	
Graphene	[14, 71-74]	Photoresist SU-8 [66]	
Black phosphorus	[75]	Benzocyclobutane [33]	
Nanocomposite	[11, 76]	Polydimethylsiloxane (PDMS) [90]	
$Ti_3C_2T_x$	[77]	Polytetrafluoroethylene (PTFE) [11, 76]	
		Polyethylene glycol terephthalate (PET) [69]	
		Liquid crystal 4'-n-pentyl-4-cyanobiphenyl [15]	

2.1 BMMPA with various architectures

2.1.1 BMMPA with planar arrangements

Placing different metallic resonators with different sizes along the horizontal direction allows broadband perfect absorption due to the mixing of multiple resonances as long as

 $\left|\omega_0^{(i+1)}-\omega_0^i\right|<\Delta\omega_0^{(i)}$.[91] By designing resonators in a unit cell to be replicated throughout the xy plane, it has a tangible effect on improving the bandwidth of MMPAs. Recent literature shows a great advance on BMMPAs operating at various frequencies. A BMMPA operating at mid-infrared using multiplexed cross resonators was theoretically and experimentally demonstrated, [58] as illustrated in figure 3(a), (b) and (c). Compared with its counterparts with one and two resonators, the BMMPA with four resonators in a unit cell demonstrates absorption above 50%, preserved in a range of 1.86 (2.98–4.84) μm, while that of the one and two resonators are only 0.64 and 0.86 μm, respectively. The Q-factor drops as the number of crosses in a single unit cell increases. The square metal patch (SMP) is a commonly used structure in designing BMMPA. [60, 63] A BMMPA with four squares demonstrates greater than 90% absorptivity and near perfect impedance matching to the free space in the frequency ranges of 6.24-7.04 THz. [63] Almost simultaneously, another group proposed a BMMPA with absorptivity greater than 90% in the same frequency range of 6.24-7.04 THz. [60] Using different metals, showing the flexibility of BMMPA design. A THz BMMPA based on three I-shaped resonators demonstrated a broad and flat absorption over a wide range of incidence angle for either transverse electric (TE) or transverse magnetic (TM) polarization. [59] The overall absorption spectrum is ascribed to the superposition of individual components.

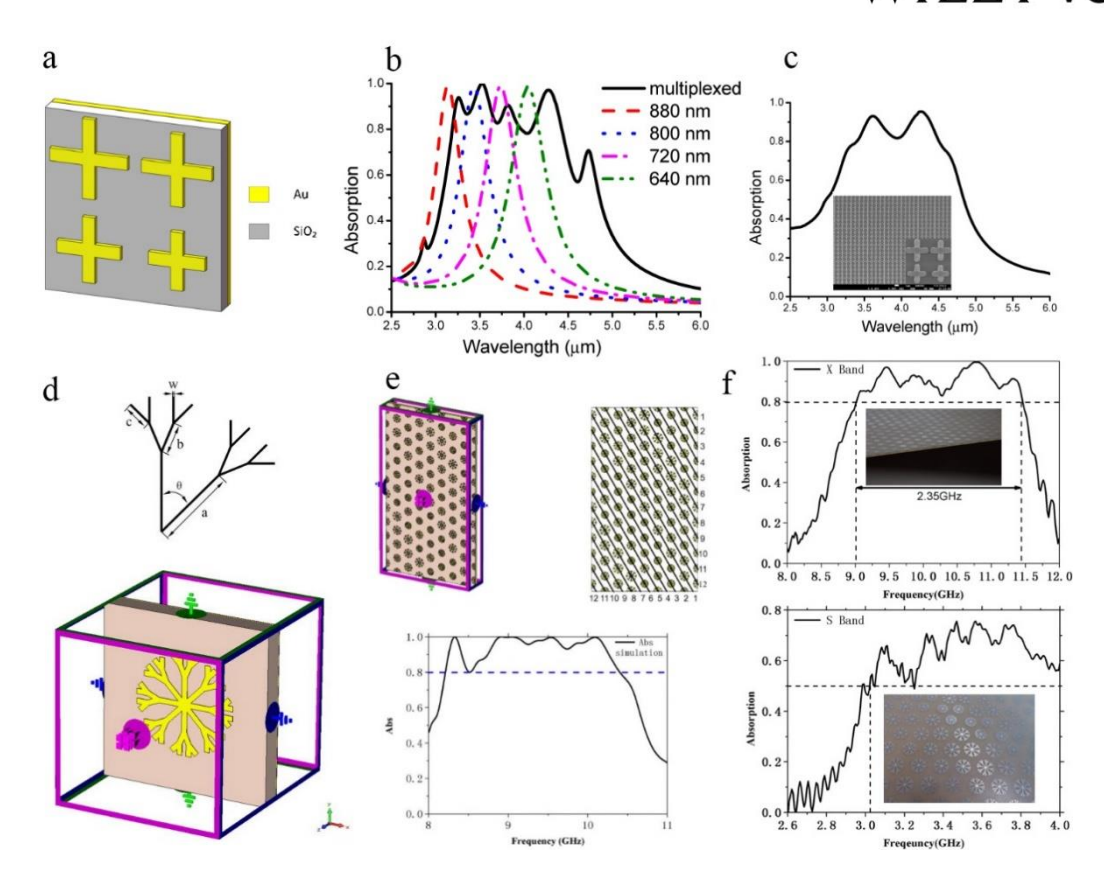


Figure 3. (a) Unit cell schematic diagram of four cross resonators. The gold layer is 100 nm thick for the ground plane and 60 nm for the metallic patterns. The SiO₂ dielectric layer is 190 nm; (b) Simulated absorption of multiplexed and four traditional non-multiplexed absorbers; (c) Measured absorption for multiplexed absorber. The inset is a SEM image of the multiplexed absorber. (d) Three-level dendritic structure and dendritic unit cell in the simulation model; (e) The schematic of the X-band absorber composed of twelve kinds of independent units and its simulation result; (f) The experimental results of the X-band and S-band absorbers. **a-c**: Reproduced from Ref. ^[58] with permission from Optical Society of America, copyright 2013. **d-f**: Reproduced from Ref. ^[54] with permission from AIP Publishing, copyright 2013.

Circular metallic patches (disks) with different sizes in a unit cell are able to obtain broadband absorption in the GHz region.^[87] Y. P. Lee *et al.* simulated cut wires with different lengths in a unit cell.^[34] They concluded that the narrow peak in GHz region was due to dielectric loss and the broad peak was due to Ohmic loss, elucidating two different mechanisms for energy dissipation. Conversely, rectangular hole arrays can be placed atop to obtain broadband absorption. A rectangular hole structure combined with a 90° anticlockwise rotation upon itself can excite mixed surface plasmons (SPs) at visible frequencies to support broadband absorption ^[92].

Metal dendrites can also be used on BMMPAs because the structure is composed of branches with different length and size in the xy plane, thus supporting multiple resonances. [54, 55, 69] Bao et~al. first proposed a method by employing dendritic branch structures of different sizes to achieve broadband absorptivity from 9.79 to 11.72 GHz. [55] With densely arranged hexagonal metal dendritic units having different sizes, a BMMPA with isotropic absorptivity, larger than 50% in the S-band, ranging from 3.02 to 4 GHz, and greater than 80% in the X-band, ranging from 9.05 to 11.4 GHz, has been demonstrated as shown in figure 3(d), (e) and (f). [54] Recently, a BMMPA based on windmill-shaped resonators was reported to achieve broadband absorption, in an approach which was different from the common size variation route, as shown in figure 4(a). [69] In this structure, ITO was introduced to be the top resonators' material, in order to tailor the Ohmic resistance of that layer. The Q-factor can be expressed as $Q = \omega_0 \times (P_T/P_L) = f_0/\Delta f$, where ω_0 and f_0 are the resonant frequencies. P_T and P_L are the stored and dissipated energy, respectively, while Δf is the absorption bandwidth. Increasing the resistance of ITO leads to a decrease of the P_L that lowers the Q-factor. When the surface resistance is $12~\Omega/\Box$ of the unit cell, the device achieves broadband absorptivity greater than 90% from 8.3 to 17.4 GHz, was achieved, as shown in figure 4(b) and (c).

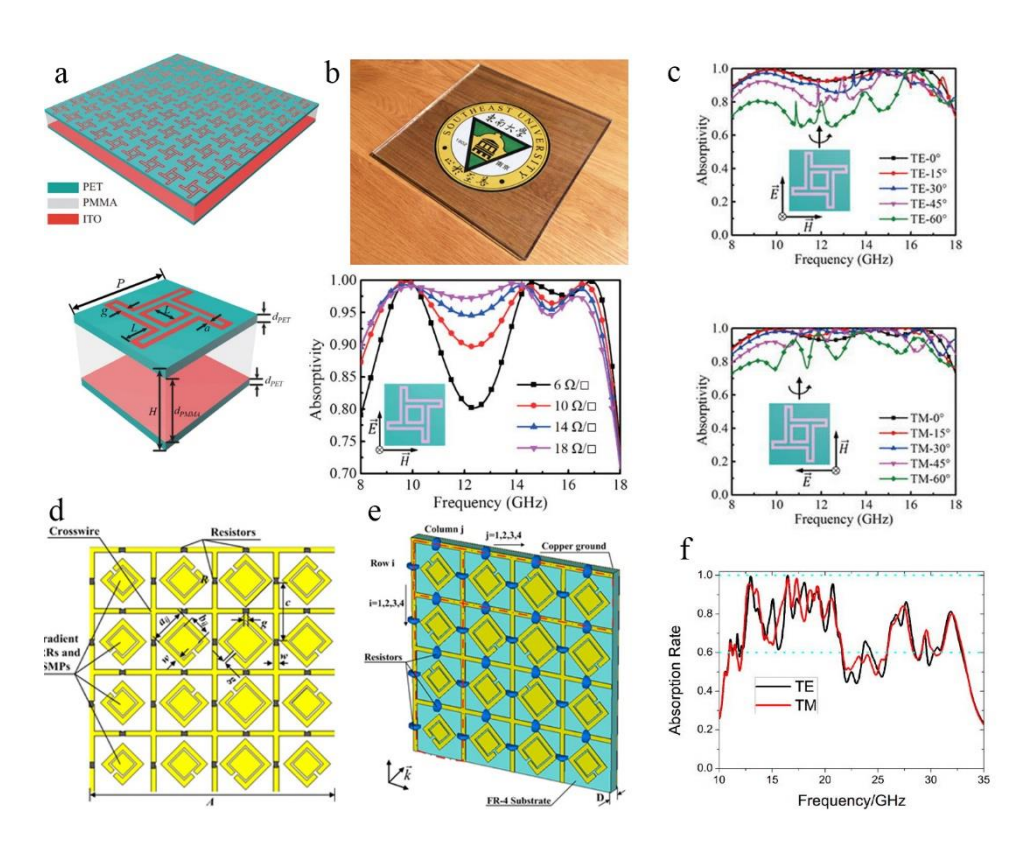


Figure 4. (a) Schematics of an optically transparent BMMPA; (b) Photograph of the fabricated sample and simulated absorptivity spectra with the increase of surface resistance of the ITO layer at normal incidence of TE wave, with the polarization direction illustrated in the inset; (c) The angular dependence of the simulated absorptivity spectra for the MMA under the incidence of TE and TM waves, with the polarization direction and the incidence angle θ illustrated in the insets. The structure of the unit cell of a proposed integrated BMMPA, where (d) is the plan view and (e) is the stereogram; (f) The calculated absorption rate for both TE and TM wave. **a-c**: Reproduced from Ref. ^[69] with permission from AIP Publishing, copyright 2017. **d-f**: Reproduced from Ref. ^[82] with permission from AIP Publishing, copyright 2014.

By modifying the size of the patterns and integrating them into a single unit cell, broadband absorption can be easily obtained. The combination of pattern with different shapes provides a route for achieving ultra-broadband spectra response. Abbott *et al.* demonstrated a retarder composed of an array of split-ring resonators and disk resonators working in the THz region. [90] Gu *et al.* propose a polarization-insensitive BMMPA absorber based on planar gradient structure MM, composed of resistor mounted crosswires and gradient split ring resonators (SRR) with a SMP in it, as shown **in figure 4(d)** and **(e)**. [82] The presence of gradient resonators makes adjacent frequencies merge into a broadband frequency range. As a result, they observed that for both TE and TM waves, the operating frequency ranges from 12.38 to 22.28 GHz, where the absorption rate is above 60%, as plotted in **figure 4(f)**. The enhanced absorption stems from the energy storage effect and difference resonances in the gradient structure. A "magnetic loop trap" structure is formed by the strong magnetic field generated around the SRR and SMP. The EM energy is confined within this structure, which effectively prevents the EM wave from leaking out. Therefore, current is excited on the top of the unit cell. By this means, EM waves could be consumed in the FR-4 dielectric substrates and the chip resistors. [82]

Two-dimensional (2D) materials have attracted great attention due to their exotic optical transparency, flexibility, conductivity and high electron mobility. [93] Low-loss graphene has an adjustable negative permittivity which enables spectral tuning of MMs, which can be used for amplitude tuning at the far-infrared and near-infrared frequencies. Graphene can be used on MMPA devices with tunability

because the dielectric properties of graphene can be dynamically tailored by shifting the Fermi energy via chemical doping or electrostatic voltage. [14, 71, 72, 94] For broadband absorption applications, Vasić *et al.* showed spectral tuning of MMPAs in the mid-infrared region. [72] Chaudhuri *et al.* demonstrated a BMMPA made of $Ti_3C_2T_x$ resonator exhibiting a high-efficiency absorption (~90%) for a wide wavelength window (~1.55 μ m). [77] Zhang *et al.* proposed a tunable BMMPA based on graphene disks operating in the mid-infrared region. [71] They found that when the graphene's Fermi energy was 0.1 eV, the corresponding bandwidth with more than 80% absorptivity can be extended to 6.9 THz, with a full width at half maximum (FWHM) bandwidth of 10.1 THz. For frequencies that satisfy $\hbar\omega < 2E_f$, where E_f is the Fermi energy, the interband transition of graphene can be disabled while the intraband transition depending on the conductivity and spectral tuning will be dominant.

In this subsection, horizontal arrangements for broadband absorption of MMPA have been introduced. The structures discussed are capable of achieving broadband absorption at THz, GHz and visible frequency ranges by placing resonators with different sizes and shapes on the *xy* plane. Further work should emphasize on integrating more resonators in the THz and higher frequencies because the nanofabrication is becoming sophisticated. At the nanoscale, neighbouring resonators on *xy* plane can influence each other and the number of resonators is limited within a period. Besides, future work should be focusing on investigating metal resonators with broadband absorption, e.g., high loss metals. Graphene has attracted attention for its tunable permittivity from visible to far-infrared region. Current work on graphene MMPAs has been limited to theoretical calculations, with no experimental work yet reported due to the difficulties of atomic-level layer manipulation. Further work should be focused on validating the theoretical calculation and addressing the difficulties on atomic layer control of 2D materials, such as black phosphorus (BP), transition metal dichalcogenides (TMD) and graphene.

2.1.2 BMMPA with vertical arrangements

Although the planar strategy is an efficient method for broadening the spectral response while maintaining high absorption, the interval between two resonant frequencies might be too wide to merge due to the spatial constraint of introducing multiband design in the same layer. [38] Alternatively,

placing resonators vertically can also extend the absorption spectrum. Zhang *et al.* stacked three dual-band sub-cells with different geometric parameters to form a BMMPA.^[95] An annular pattern is on the top surface and a metallic circular patch is located at the bottom of each sub-cell. As a result, the BMMPA shows a continuous absorption spectrum between 8.8 and 10.8 GHz with absorptivity all above 80%. The FWHM absorption bandwidth is 2.3 GHz (8.7–11 GHz). Although the square lattice is usually created for narrow band absorption, in this case it was stacked to form a BBMPA with a truncated pyramid structure, working in the full infrared region.^[66, 96]

Slowlight waveguide modes of weakly coupled resonances in various patterns is proposed for broadband absorption. [86, 97] The stacked anisotropic MMPA allows the excitation of slow-wave modes in tapered, alternating metal-dielectric thin films, used to "stop light". [78, 98] Light of a specific wavelength is slowly "squeezed", which is slightly different from the abovementioned vertical stacking—while they yield a broadband absorption by superposing a series of narrow absorption peaks, the slow light effect does not use direct superposition because the layers are too thin to support localized resonance. The incident energy propagates through the z-direction without penetrating into the resonators and then whirls into the resonator region. Vortices are formed close to the interface between the resonator and air regions with concentrated EM field. Quadrangular pyramidal frustums composed of 20 stacked metal patches, with their width tapered linearly from bottom to top were demonstrated by He et al., as shown in figure 5(a), (b) and (c). [98] The device's experimental versus simulation absorptions are compared in figure 5(d). It achieves nearly unity absorption from 8 to 14 GHz over a wide angular range and the measured relative bandwidth is 61.6% while the simulated is 53.1%. The broadband response can be easily understood by examining the electrical and magnetic distribution. At short wavelengths, EM absorption is primarily located at the tapered top, while long wavelengths EM absorption is primarily located at the bottom. Additionally, the absorption is nearly independent of the incidence angle below 40°. At the same time, the slowlight waveguide can be obtained by etching a metal slab into a sawtooth shape with the tooth widths increasing gradually from top to bottom, as demonstrated in **figure 5(e)**.^[78] As a result, the absorptivity is higher than 95%

and preserved for a wide frequency range due to gradual change of effective indexes, as shown in **figure 5(f)**. Meanwhile, the BMMPA maintains high and ultrabroadband absorption when the incident angle is smaller than 60°. **Figure 5(g)** shows that the fundamental propagating mode has an extreme point with low group velocity, i.e., $|v_g|/c$ approaching 0, mirroring slow light modes present in the simulated structure. With $v_g = 0$ for different values of W and teeth widths at the central energy allows waveguides with W from 150 to 600 nm to support slow light modes.

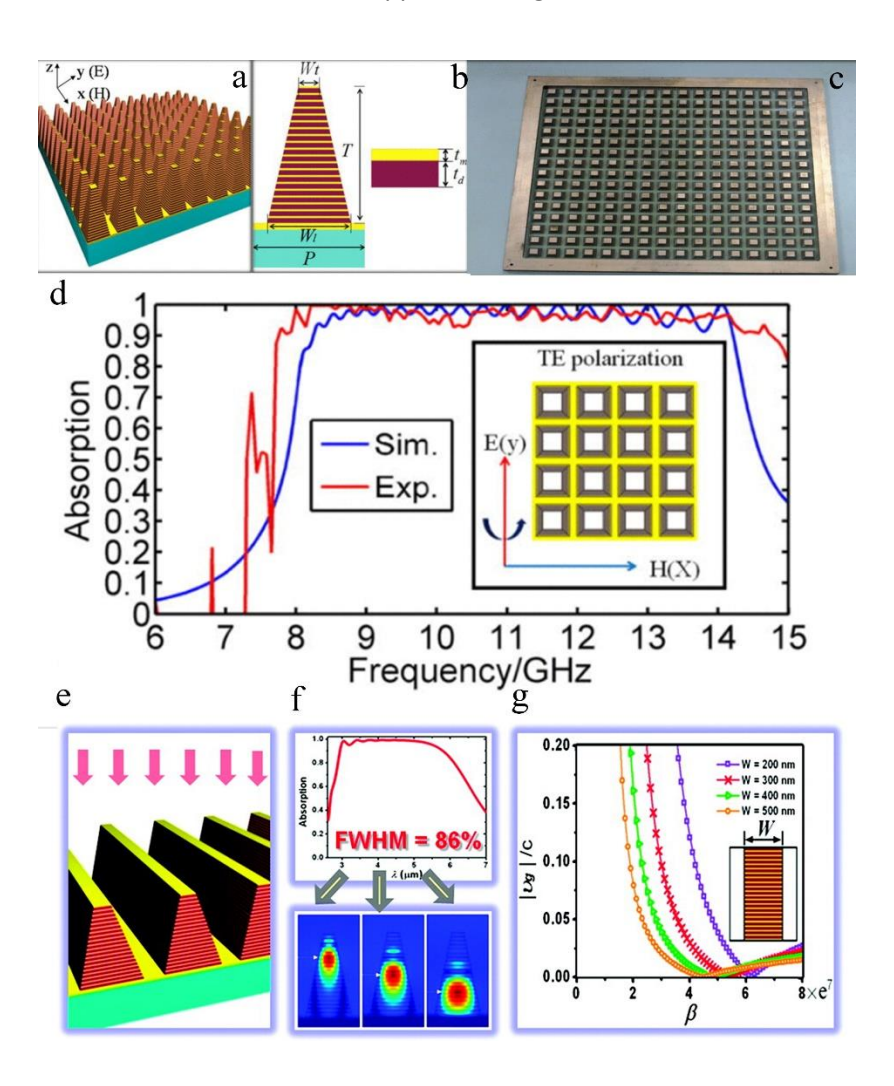


Figure 5. (a) Three-dimensional illustration of the simulated MMPA; (b) schematic of a MMPA unit cell, and (c) photograph of the fabricated sample. The optimized dimensions of a unit are $W_t = 5$ mm, $W_t = 9$ mm, P = 11 mm, $t_m = 0.05$ mm, $t_d = 0.2$ mm, and T = 5 mm. Subscript "m" represents copper, and "d" for FR4; (d) Comparison between the simulated absorption (blue line) and experimental absorption (red line). The inset shows the configuration of the incident wave. (e) Diagram of the sawtooth anisotropic MM thin film absorber. Light of TM polarization is incident along z direction; (f) Absorption spectra for the sawtooth MMPA and distributions of

magnetic field corresponding to 3.5, 4.5, and 5.5 μ m, respectively; (g) Relationship between the group velocity and propagation constant (proportional to wavevector) at different W. **a-d**: Reproduced from Ref. ^[98] with permission from AIP publishing, copyright 2012. **e-g**: Reproduced from Ref. ^[78] with permission from American Chemical Society, copyright 2012.

Xiong *et al.* proposed a stacked BMMPA structure utilizing destructive interference mechanisms.^[86] It maintains a 90% absorption band spaning from 8.37 to 21 GHz with a thickness of 0.10–0.26 free space wavelength. Being different from the gradually size-changing resonator at the vertical direction, there are some examples in the literature demonstrating BMMPAs by embedding patterns in dielectric spacer with different distances.^[89, 99] For example, a three layered cross resonator embedded in polyimide shows three resonances at 4.32, 5.31, 5.71 THz, as the schematic shown in **figure 6(a)**.^[89] Since the three peaks are close enough, they form a wide frequency band from 40.8 to 5.94 THz, where the absorption is greater than 60%, as shown in **figure 6(b)**; the FWHM of the absorption is 48% of the central frequency of the three-layer structure.

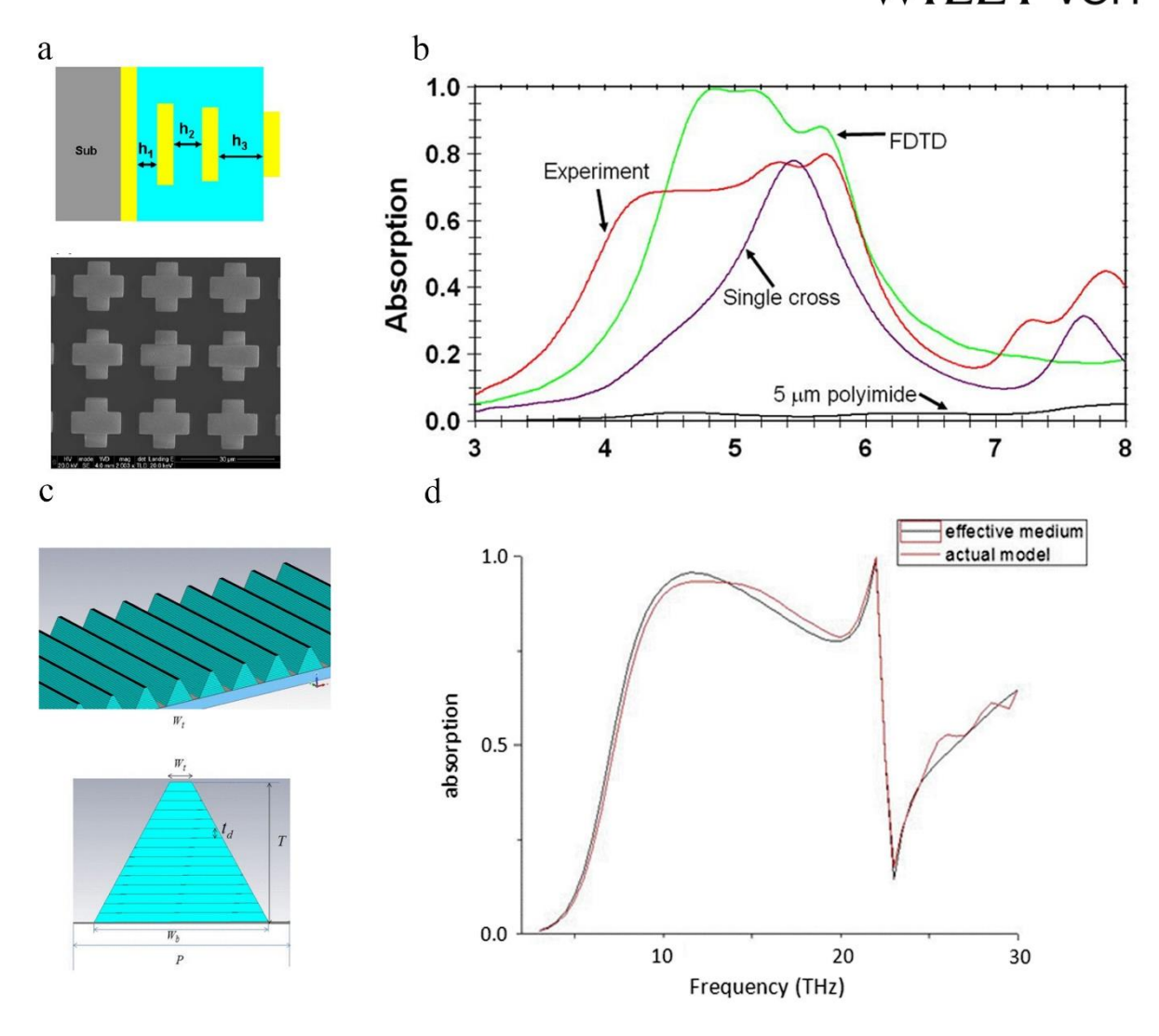


Figure 6. (a) Cross section illustration and SEM image of the complete multilayer absorber; (b) Experimental and simulated data of the multilayer absorber. Also plotted is the experimental absorption spectrum for a single layer absorber. (c) Schematic diagram for a line array of graphene-dielectric multilayered quadrangular pyramidal frustums backed with a homogeneous metal film. A unit cell of the graphene BMMPA is illustrated, with P = 10 μ m, $W_b = 8 \mu$ m, $W_t = 1 \mu$ m, $t_d = 400 \text{ nm}$ and $T = 6 \mu$ m. Light with TM polarization is incident along z-direction; (d) Absorption spectra for a graphene-dielectric multi-layered pyramid absorber with N=15 periods and thickness of dielectric layers equal to 400 nm. The red line is the result of the real structure, and the effective homogeneous mode is shown by the black line. **a** and **b**: Reproduced from Ref. [89] with permission from Optical Society of America, copyright 2011. **c** and **d**: Reproduced from Ref. [74] with permission from IEEE, copyright 2013.

Graphene can be vertically stacked. [73, 74, 100-102] Chen *et al.* simulated a graphene-based BMMPA which consists of an array of graphene-dielectric multilayered pyramidal frustums with a homogeneous metal

film, as shown in figure 6(c). [74] Since the shape of the resonator is unchanged, the pyramidal shape is then tapered linearly from bottom to top, to breed different resonances with a subtle progression. The spectrum in figure 6(d) indicates the performance is excellent, with absorption around 90% covering the frequency range from 10 to 22 THz. The localized EM wave gives an intuitively interpretation for broadening: as the frequency increases, it moves up gradually toward the top of the pyramid structure. Moreover, they found that both the slow wave mode and Floquet periodic mode contributed to absorption. To expand the near-unity bandwidth absorption in the THz region, Amin et al. first adopted an asymmetric graphene pattern to excite quadrupolar SPPs, in comparison with graphene absorbers designed to operate only in their dipolar mode, as shown in figure 7(a). [101] The absorption of threelayer stacking design in figure 7(b) demonstrates a band of 90% absorption from 4.7 to 11.6 THz. By repeatedly stacking graphene/MgF2 layers, another group achieved a broad absorption band in the THz region as well.^[73] Afterwards, a BMMPA with two left-handed and two right-handed helices of graphene has been proposed to achieve perfect absorption covering from ultraviolet to near infrared, i.e., 200-1792 nm. [100] By utilizing many-particle effects, a nano-cross elliptical hole structure embedded in multilayer-graphene stack was proposed to enhance the absorption of graphene and extend the bandwidth.[102]

Compared with graphene and TMDs, BP has a remarkable direct bandgap (~0.3 eV) in bulk, while the 2D BP provides a thickness-dependent direct bandgap ranging up to ~2 eV for monolayer BP. An IR absorber, based on 2D BP MMs sandwiched between dielectric layers, was proposed to achieve extremely broadband absorption ranging from ~30 to 80 μ m, ^[75] with its design shown in **figure 7(c)**. Interference theory was introduced to reveal the mechanism behind the observed absorption phenomena, as shown in **figure 7(d)**. The destructive interference between the directly reflected wave and the following multiple emergent waves effectively captures the behaviour of the BMMPA, giving rise to the high absorption. The electric field intensity at the z-direction in **figure 7(e)** is shown for TM polarization with $\lambda = 54.3 \mu$ m, where the number of layers in the sandwich-like structure (NLSS) decreases from 4 to 1. The field enhancement is primarily concentrated around the edge of the BP

nano-ribbon and the absorption increases with increasing NLSS. The distance D between neighbouring BP nano-ribbons and their thickness affect the absorption performance, as shown in **figure 7(f)**. For $D \ne 0$, absorption rates greater than 90% are achieved if D is less than 80 nm, while for D = 0 nm the absorber performance is evidently reduced. The attenuation can be ascribed to the fact that the MM structure no longer exist after merger. By changing thickness Δ , and thus changing the bandgap, the absorption peak position exhibits a blue shift with decreasing Δ . The proposed absorber achieves a perfect absorption for bilayer and trilayer BP MMs when nano-ribbon width w = 230 nm.

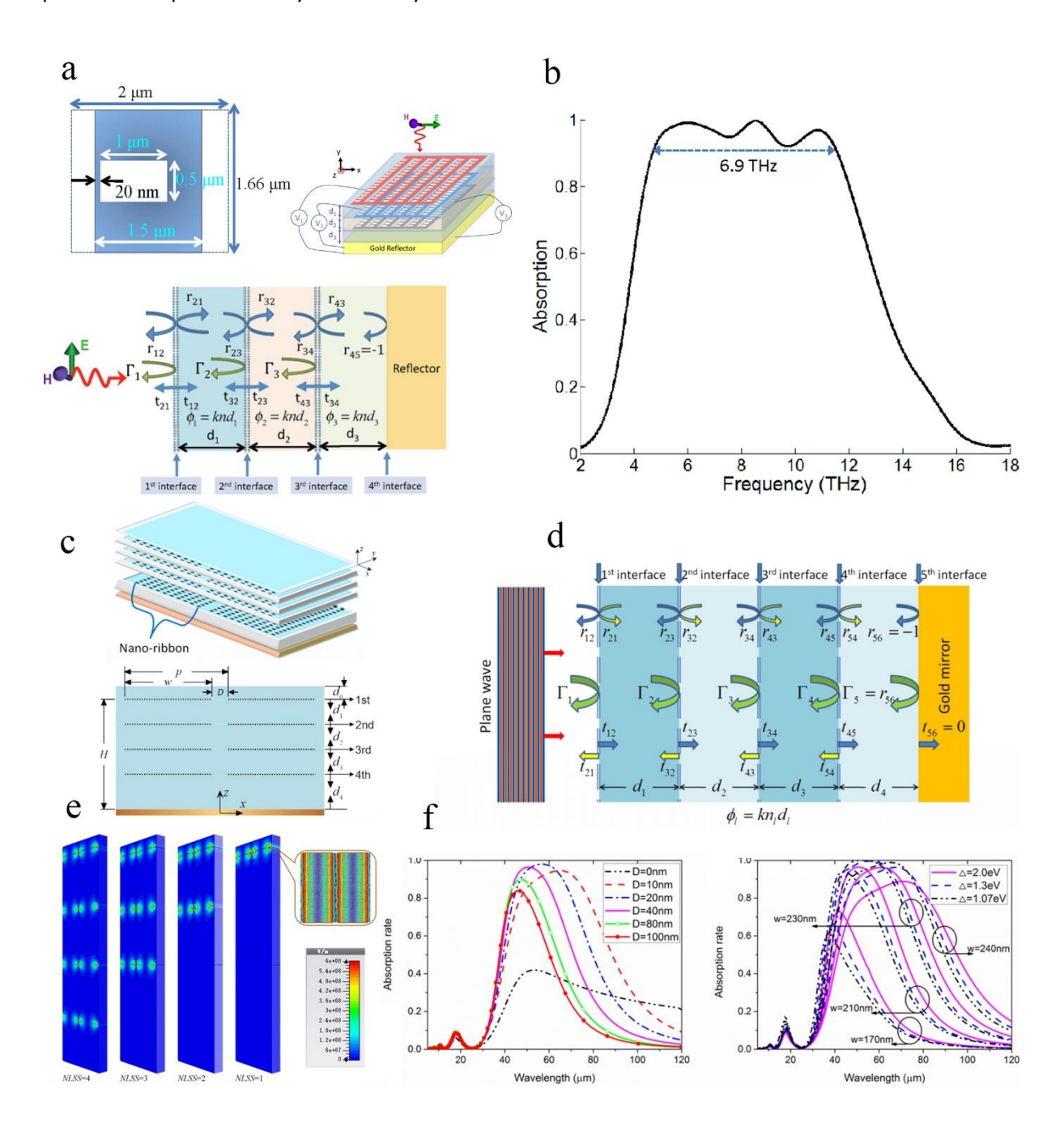




Figure 7. (a) The schematic diagram of the proposed absorber with three layers of graphene (top right); The graphene unit cell with an asymmetric void with its dimensions (top left). Description of the transmission line model for the multilayered absorber (bottom); (b) The absorption spectra of the three-layer design with d_1 = 0.67 μ m, d_2 = 0.5 μ m, and d_3 = 4.78 μ m. (c) Schematic of the proposed sandwich-like structured BP absorber and front view of the proposed absorber with layer dimensions; (d) A schematic diagram of the transmission and reflection for a four-layered sandwich-like BP structure; (e) Simulated average electric field intensity values for monolayer BP MMs with two nano-ribbon periods aligned along the x-direction. The inset presents a sectional view at the in-plane across the 1st interface for NLSS value of 1; (f) Simulated absorption rate spectra for TM polarization at various distances between two nano-ribbons and for various thicknesses of BP in monolayer, bilayer and trilayer with ridges perpendicular to the x-direction. a and b: Reproduced from Ref. [101] with permission from Optical Society of America, copyright 2013. c-f: Reproduced from Ref. [75] with permission from Optical Society of America, copyright 2017.

In this subsection, we have reviewed BMMPAs with vertical arrangements. The BMMPAs with vertical stacking are relatively more effective for broadband absorption than their planar counterparts, but they are typically bulkier because of the stacked layers. Fabricating multiple aligned patterns is complex and time-consuming. 2D materials are attractive for designing THz-absorbers, especially for vertical stacking in BMMPA designs, for the following reasons: 2D layers can support SPPs at THz frequencies; the atomic-scale stacking circumvents the trade-off between stacking thickness and absorption; frequencies tunability can be achieved by biasing the layer. However, due to its atomic thickness, a single layer of 2D material remains practically transparent to THz waves and, as a result, the overall absorption is significantly reduced. To enhance the absorption of 2D materials, different means have been investigated, such as using graphene-based gratings, [103] exploiting the quantum dots near graphene [104] and plamonic effect. [102] Moreover, methods permitting a facile operation in controlling the layers of 2D material and their doping still need improvement.

2.2 BMMPA with lumped elements

Following equivalent circuit theory, metallic patterns can be understood as equivalent inductors and capacitors to approximately determine their resonant frequencies.^[45] Then, lumped resistors are

introduced to connect the gaps of resonant patterns. Compared with traditional MMPAs with only metal structures and dielectric substrates, MMPAs loaded with lumped elements (resistor, inductor, capacitor and diode) provide advantages such as tenability and spectra broadening. [50, 105-109] The lumped elements are loaded by welding to connect the different resonant modes together and consume EM energy. Typically, the Q-factor in electrically coupled LC (ELC) and SRR MMPA is defined by $Q = \sqrt{LC}/R$, with L and C are the inductance and capacitance of the equivalent inductor-capacitor circuit. Increasing the resistance R yields a flatter, lower Q-factor, while decreasing R leads to a sharper, higher Q-factor. To further decrease the Q-factor, the elements are embedded into the MM structure. [50] A split-coin resonator BMMPA welded with lumped resistances demonstrates an absorptivity of 90%, with 1.5 GHz bandwidth and a FWHM of up to 50%, as shown in figure 8(a) and (b). [105] The geometrical parameters of the system are defined in figure 8(a), noting that it is not limited by the quarter wavelength thickness and it is relatively thin ($\sim \lambda/10$) in the propagation direction. Before loading the lumped resistors the absorption is narrow, with two peaks at 5.9 and 7.2 GHz, as shown in figure 8(c). However, after introducing the lumped resistances, the simulated absorptivity exceeds 90% from 3.1 to 5.6 GHz and the FWHM is up to 55% while maintaining absorption unchanged, as shown in **figure 8(d)**. When C=4 pF and $R=250~\Omega$, the absorptivity peaks and the bandwidth extends from 2.2 to 4.7 GHz, with the FWHM inceasing to 72%. However, when C=10 pF, the performance of BMMPA is the best due to reduced Q-factor. While the lumped resistance mainly influences the magnitude of absorptivity, the lumped capacitance influences both the magnitude and bandwidth of absorptivity, as observed in figure 8(d).

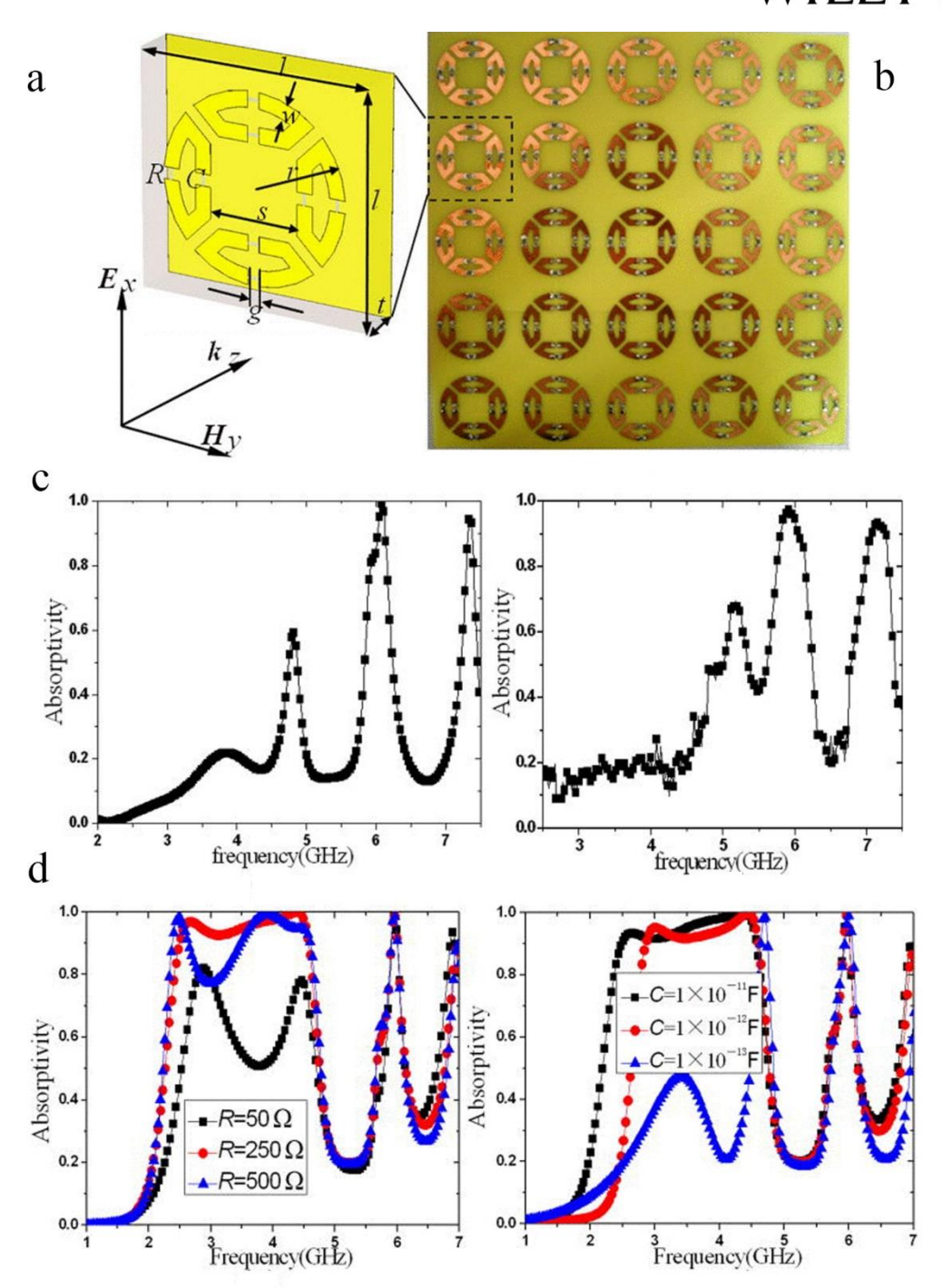


Figure 8. (a) Perspective view of unit cell with indicated TEM wave direction and geometric dimensions and lumped parameters: I = 40 mm, r = 16 mm, s = 15.2 mm, w = 2.7 mm, g = 2 mm, t = 6 mm, C = 4 pF, R = 249 Ω ; (b) Photograph of fabricated lumped elements MA sample; Absorptivity of MMPA before introducing without lumped elements: (c) Absorptivity of the simulation (left) and experiment (right) results; Absorptivity of the BMMPA with different values for the lumped elements: (d) Lumped resistance R and lumped capacitance C, respectively. Reproduced from Ref. [105] with permission from AIP publishing, copyright 2012.

Double-rings loaded with lumped resistances have been validated in their broadband absorption properties. [106, 107] A double-circle ring BMMPA yields a 7.60-GHz-wide absorption from 8.87 GHz to 16.47 GHz with absorptivity greater than 90%. [107] A thin and polarization-insensitive BMMPA, created by loading eight lumped resistors into double octagonal rings, has been investigated by experimental and computational methods. [106] The results achieved a 9.25 GHz-wide absorption from 7.93 to 17.18 GHz, with absorptivity larger than 90% at small incident angles, from 0 to 20°. The electrical field distributions of this structure indicate that high absorption can be ascribed to the rings and resistances in the system. Periodic array of metallic strips are connected to achieve thin and polarization-insensitive BMMPA. [108] The thickness of the absorber is 3 mm, which is almost 1/17 of the free space wavelength at the lowest frequency of 6 GHz. In addition to connecting the resonators via resistors and capacitors, chip resistors and PIN diodes were also used to provide both a broadband absorption profile and switching capabilities. [110] The absorber switched between two frequency bands from 8.45–9.3 GHz and 9.2–10.45 GHz, when the PIN diode is switched to ON and OFF states, respectively.

Lumped elements are welded between the resonators to reduce the *Q*-factor of MMPAs and thus achieve broadband absorption. However, this method is limited to the GHz spectrum, where radar applications operate. With nanoscale resonator fabrication processes, introducing equivalent lumped elements is a tough task. One can transfer this method to THz or infrared frequencies, however, connecting the resonators equivalent with the lumped elements needs accurate alignment during fabrication process. Future work should be focused on addressing this issue.

2.3 BMMPA with plasmonic nanocomposite

In a typical MMPA structure, the contribution of metallic absorption is dominant when the device is operating at NIR or in the visible spectrum. Therefore, the role of dielectric absorption is less important at these frequencies and the device can be made thinner for high frequency application. Metallic NPs offer tailored plasmonic response for absorption and scattering enhancement at their resonant frequency [111, 112]. The top layer is substituted by an ultra-thin (~20 nm) plasmonic nanocomposite made of metal NPs dispersed randomly in polymeric (or generally dielectric) matrix. By combining

impedance matching of the medium to free space to avoid reflection at the outer layer, multiple-reflection of light between the layers and light trapping and absorption from the tiny metallic particles, the nanocomposite BMMPAs have been shown to operate in wide spectral range from UV^[11, 113] to visible^[76] and NIR.^[11, 114]

A high density nanocomposite can lead to broadband absorption due to excitation of localized plasmon resonance of the NPs by visible light. [114] Gold, [11] copper [76] and silver [113, 114] nanocomposites have been applied on BMMPAs for perfect absorption. Elbahri et al. replaced the metallic structure in the MMPA with nanocomposite (Au/SiO₂, figure 9(a), (b)) resulting in almost 100% absorption over a broad range of frequencies from UV to NIR, as shown in figure 9(c). [11] They found that the fill factor of gold NPs in the composite can significantly influence the optical response. A 40% filling factor has been found to be optimum for high absorption covering visible to NIR region, making the surface appear black. This broadband absorption is due to two factors: impedance matching in MM as well as dipole-image interaction and broad Mie resonance of NPs with a large size distribution. Afterwards, they demonstrated a Cu-PTFE nanocomposite BMMPA which presents an average absorption in the visible frequencies above 97%, as shown in figure 9(d). [76] The absorption properties of this copper perfect absorber is greater than that of its gold counterpart because copper is more lossy than gold in the visible spectrum. Although the effect of filling factor and thickness of the film or composite of a silver perfect absorber shows the same influence on the optical properties than in the copper or gold systems, there is an absorption dip at higher frequency for the Ag nanocomposite MMPA, rooted in the overlap of SPR and plasma frequency, as shown in figure 9(e).[113] Due to the high optical absorption in the deep UV region, Ag nanocomposite BMMPA can be used for UV protection applications.

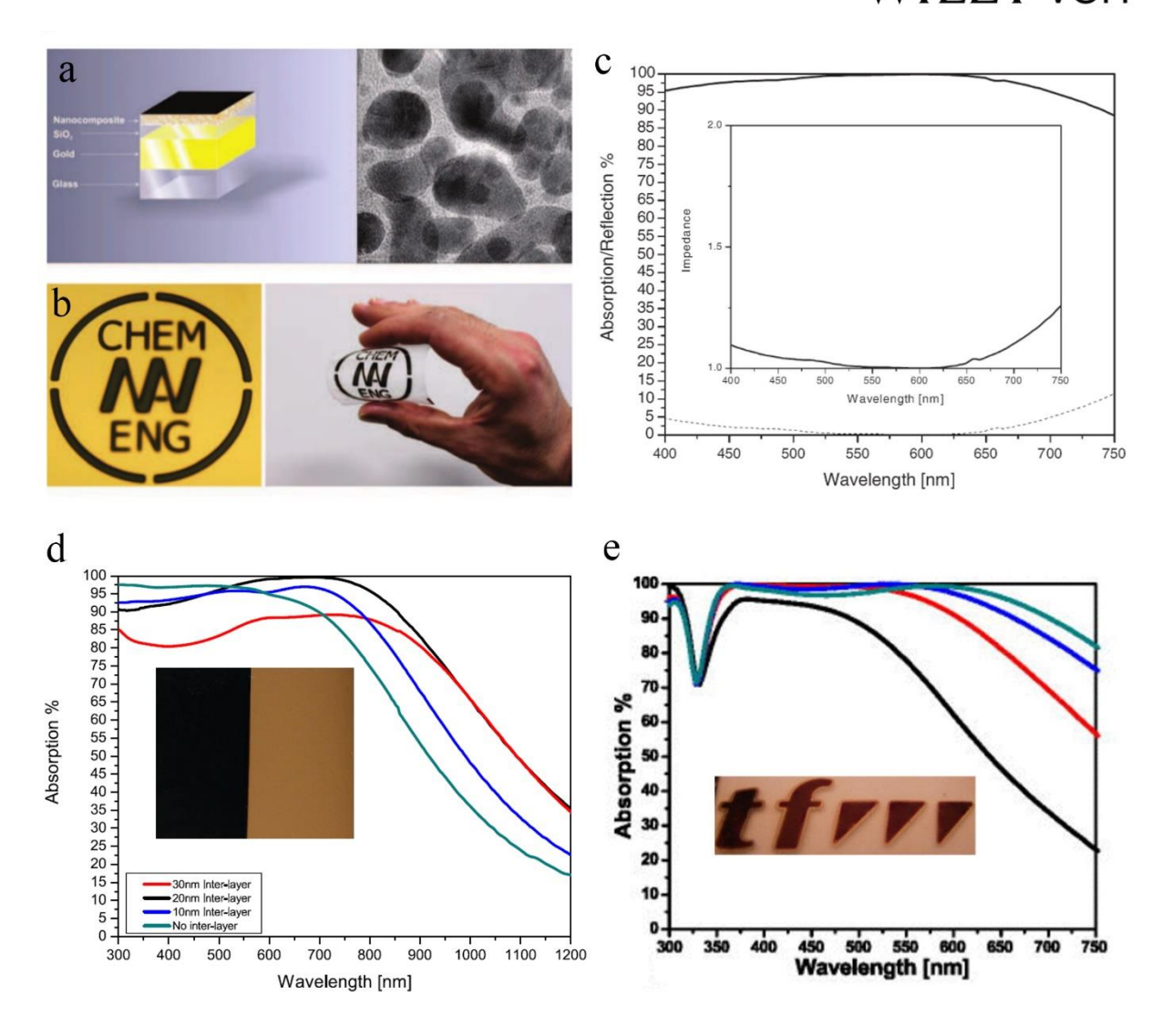


Figure 9. (a) Schematic of a perfect absorber structure manufactured by sputtering. The thickness of the nanocomposite, SiO₂ spacer, and gold mirror layers are 20, 25, and 100 nm, respectively. The left panel illustrates that the whole structure sits on top of a glass substrate; the right panel shows a top-view TEM image of the nanocomposite film; (b) Perfect absorber (blackbody) coated via mask on gold-coated glass (left) and flexible polymer foil (right). These examples show the potential of the coating for application on different substrates, including flexible ones; (c) Absorption (solid line) and reflection (dashed line) spectra of the system described in panel (a), measured at 6 degree angle of incidence. The inset shows the impedance data of 20 nm Au/SiO₂ nanocomposite deposited on a 100 nm gold film with 25 nm SiO₂ spacer layer. (d) Absorption spectra of 20 nm Cu-PTFE composite on a PTFE spacer layer with different thicknesses, over 100 nm of Cu. The green curve shows the composite on a base layer without any inter-layer for comparison. The inset is the photo of the perfect black absorber (left) in comparison with bare copper film (right). (e) Absorption spectra of a silver-SiO₂ nanocomposite

of 15 nm (black curve), 20 nm (red curve), 25 nm (blue curve), and 30 nm (green curve) thickness, deposited on 15 nm of SiO₂ coating a silver mirror. The inset is true color photograph of the perfect absorber coated on transparent polymeric substrate presenting the logo of Faculty of Engineering (TF) of University of Kiel. **a-c**: Reproduced from Ref. [11] with permission from John Wiley and Sons, copyright 2011. **d**: Reproduced from Ref. [76] with permission from Springer Nature, copyright 2012. **e**: Reproduced from Ref. [113] with permission from AIP publishing, copyright 2014.

In summary, the absorption peak position and intensity can be engineered by altering the type of nanocomposite, its filling factor, surrounding dielectric environment and the different layer thickness. The advantage of nanocomposite BMMPAs is their high absorption, obtained through a facile and scalable fabrication process, without involving complex photolithography and pricy electron beam lithography (EBL). Additionally, the absorption yielded is polarization-insensitive and strongly angle independent. However, their working frequency is confined to the UV, visible and NIR regions due to the plasmonic properties of metal NPs. Inspired by biological systems, researchers can seek solution from nature. Bio-nanocomposites are incorporated to develop BMMPAs. A smart plasmonic absorber based on metal-polymer bio-nanocomposites mimicking beetle's body parts achieves a broadband absorption extending from 300 nm to 900 nm. [115] Future work should be focused on two points: high temperature resistant BMMPAs and low frequencies BMMPAs based on nanocomposites. Due to the high absorption from UV to NIR regions, BMMPAs with nanocomposites are attractive for solar energy harvesting. Dielectric materials of nanocomposites are typically composed of polymers which are vulnerable to high temperature. Extending absorption to THz region is also another direction of research. Composites with polymer and carbon particles, with large aspect ratio, have exhibited absorption properties in the THz $^{[116]}$ or and $\mathrm{GHz}^{[117]}$ region.

2.4 Other BMMPA designs

In the previous subsection, we have reviewed mainstream approaches to extend the bandwidth of MMPAs, including horizontal and vertical stacking of resonators, introduction of lumped elements and plasmonic nanocomposite BMMPAs. Additional design tools or methods, such as CMM structures, [35,



^{50]} space-filling,^[65] dielectric tailoring,^[85, 118, 119], using cross-trapezoid resonators,^[24, 120] and resonator material tailoring^[63, 67, 77, 121, 122] are also being investigated to achieve broadband absorption as well.

2.4.1 CMM structures

A trilayer CMM absorber structure, fabricated with CMOS-compatible materials, combines electrical and cavity resonance mechanisms in the NIR region, demonstrating broadband absorption. The cavity and electrical resonances can be tuned by changing the dimension and dielectric thickness. The dual band absorber is then engineered to be at the same wavelength and by merging the two resonant mechanisms broadband absorption is achieved. Using a different approach to CMMs, Cummer *et al.* proposed a BMMPA structure with complementary ELCs and SRRs, as shown in **figure 10(a)**. Figure **10(b)** depicts the spectra response of the joint ELC and SRRs which is stronger and broader than that of an individual ELC or SRR. The calculated absorption is 95% at 2.67 GHz with a FWHM bandwidth of 300 MHz. According to Ref. he basic concept of broadening bandwidth of ELC-SRR BMMPAs relies on tailoring the electrical Lorentzian response in ELC and Lorentzian-shaped resonant magnetic response in SRR. This ELC-SRR structure can be further stacked to demonstrate peak absorption of 99.9% at 2.4 GHz, with FWHM of 700 MHz.

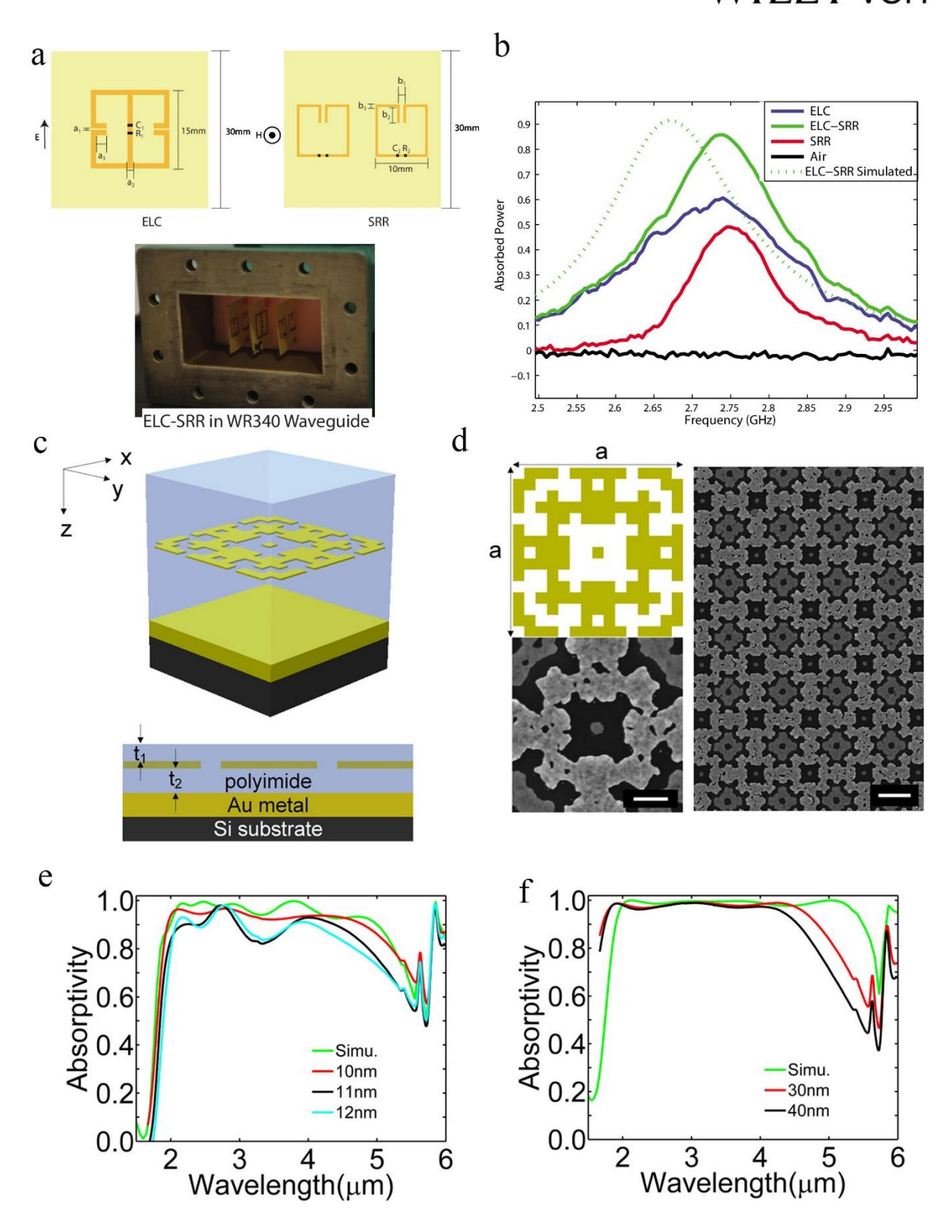


Figure 10. (a) The optimum single-cell ELC-SRR absorption was achieved with ELC parameters of a_1 =0.35 mm, a_2 =1 mm, a_3 =0 mm, a_3 =0 mm, a_3 =10 pF, and a_3 =10 pF, and ELC-SRR measured in a WR340 closed waveguide; (b) ELC-SRR has the highest and broadest absorption with a 86% peak at 2.74 GHz, and FWHM bandwidth of 170 MHz. (c) Diagram of optimized Au-based

BMMPA structure; (d) Top left: Top view of one unit cell of the design. Bottom left: FESEM image of a unit cell of the fabricated structure. Scale bar is 200 nm. Right: Low-magnification FESEM image of the same structure. Scale bar is 600 nm; (e) Simulation and measurements for Au-based BMMPA under unpolarized illumination at normal incidence. The average Au thicknesses of the Au nanostructures as determined by atomic force microscopy measurements are 10, 11, and 12 nm; (f) Simulation and measurements for Pd-based MMAs with Pd nanostructure thicknesses of 30 and 40 nm under unpolarized illumination at normal incidence. **a** and **b**: Reproduced from Ref. [50] with permission from AIP publishing, copyright 2010. **c-f**: Reproduced from Ref. [65] with permission from American Chemical Society, copyright 2014.

2.4.2 Space-filling resonator design

However, the disadvantage of placing resonators with different sizes in a plane is that it is extremely difficult to fit many different sizes of arrays into one unit cell. Moreover, in a unit cell with different resonators or same resonators with different sizes, it will give rise to inhomogeneous characteristics i.e. polarization-dependency and sensitivity to oblique incidence. [49] To overcome these problems, Mayer et al. used GAs to identify the geometry of a single-layer metal nanostructure array that offers broadband absorption independent of polarization, as shown in figure 10(c) and (d).[65] The nanostructures obey certain predefined fabrication constrains, with a cross dipole centered in the unit cell, a large loop centered and interconnected in the unit cell and four smaller isolated loops located at the corner of the unit cell. The predefined structures create EM resonances with narrowly spaced center wavelengths which are merged into a broad resonance in the mid-IR region. The measured absorptivity of the BMMPA for unpolarized TE, and TM illumination agrees well with simulation results, as plotted in figure 10(e) and (f). The average absorptivity of the BMMPA is greater than 98% in a band covering from 1.77 to 4.81 µm. Additionally, optimized Au and Pd structures are compared, showing that the Pd offers significant advantages for robust and reproducible fabrication. While increasing the Au film thickness to 11 and 12 nm results in large fluctuations in absorptivity and a reduction of absorption near the long wavelength edge, increasing Pd thickness from 30 to 40 nm has a negligible influence on the absorption, with only a slight reduction in the long-wavelength extreme. Similarly, a Hilbert space-filling curve, a continuous fractal space-filling curve first described by the German

mathematician David Hilbert, has been proposed as a design to provide broadband absorption. A terahertz BMMPA based on resistive Hilbert curve array is proposed for broadband terahertz detection. The structure in this reference differs from the conventional Hilbert curves, in that it uses resistive curves while in the case of traditional Hilbert curve absorbers, the material used is highly conductive. It achieves a fractional bandwidth (bandwidth of a device divided by its center frequency) of 100% for normal incidence and more than 90% in case of oblique incidence of 45° and 60° for both TE and TM polarizations.

2.4.3 Dielectric layer tailoring

Broadband absorption can also be achieved by mechanical means, [118] temperature tuning, [85] applied electric^[15] and magnetic field^[119, 124]. In our previous study, we demonstrated a BMMPA with pseudobroadband spectrum by using mechanical means.^[118] The top resonator is a typical ELC structure, as shown in figure 11(a). By placing a dielectric slab in close proximity to the subwavelength structures, on the condition that this placement leads to symmetry breaking of the overall structure, multiple absorption peaks can be created and the absorption region can be broadened by bringing a vertical half-slab (not shown in figure) or horizontal half-slab (shown in figure 11(b) and (c)) close to it. Recently, Qu et al. used water as the dielectric substrate for broadband absorption, as demonstrated in figure 11(d).[85] In contrast to the well-known metal-substrate metal configuration, the substrate is a hybrid of water and a low-permittivity material. The broadband absorption benefits from the dispersive permittivity of water in the corresponding band. Although the absorption efficiency is weak due to the impedance mismatch stemming from the large permittivity of water, it can be enhanced by introducing a layered performance matching (LPM) layer and top square resonators. Figure 11(e) and (f) plots the simulation and measured results of the BMMPA at different temperature, indicating the absorption performance of the water-substrate absorbers could be tuned according to the environment temperature.

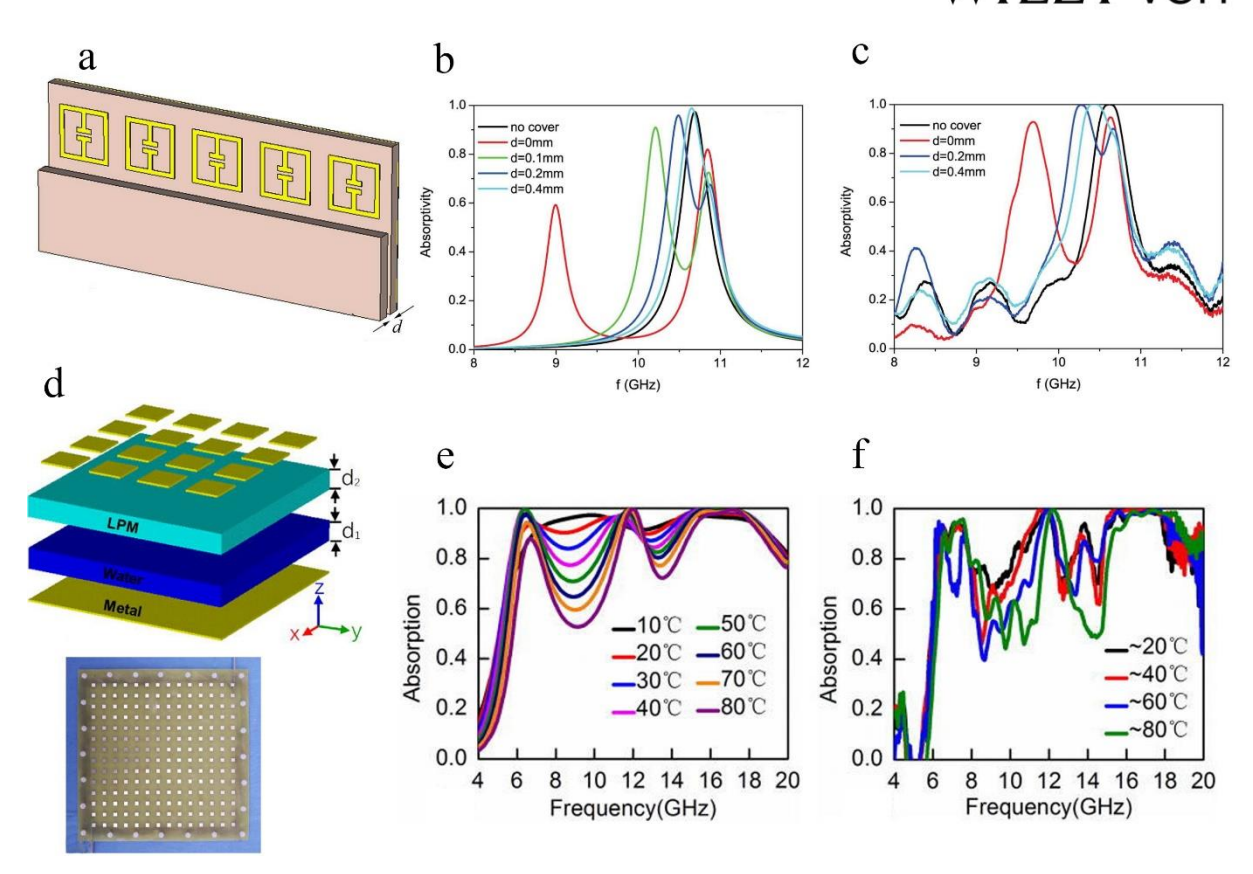


Figure 11. (a) BMMPA with a horizontal half-slab, and (b) theoretical and (c) experimental absorption spectra for different *d*. (d) 3D schematic diagram of the water-substrate BMMPA and optical image of the assembled prototype of the water-substrate BMMPA; (e) Simulated and (f) measured absorption spectra of the fabricated water-substrate BMMPA at different temperatures. **a-c**: Reproduced from Ref. [118] with permission from Optical Society of America, copyright 2012. **d-f**: Reproduced from Ref. [85] with permission from AIP publishing, copyright 2017.

Recently, a combination of ferrite and continuous wire forming a MM structure was shown to achieve a tunable negative index.^[125] Under an external applied magnetic field, the ferrite offers a broadband magnetic response which interacts with the electric resonance supported by the continuous wire, which is embedded in the ferrite layer. We also demonstrated dual, multiband and broadband absorption in MMPA based on ferrite in our previous work.^[119, 126] For broadband absorption, the proposed structure included a copper wire embedded in a FR4 layer and then sandwiched between two ferrite slabs, as illustrated in **figure 12(a)**.^[119] To excite magnetic anisotropy, a magnetic field is applied to the ferrite slabs along the *z*-direction. Under a different magnetic field, varying from 2.6 to

3.4 kOe, the magnetic resonance shifts from 10 to 12.5 GHz, with a well-preserved big magnetic loss. As a result, absorption is high, while bandwidth and maximum absorption are not changed under the different magnetic field, as shown in **figure 12(b)**.

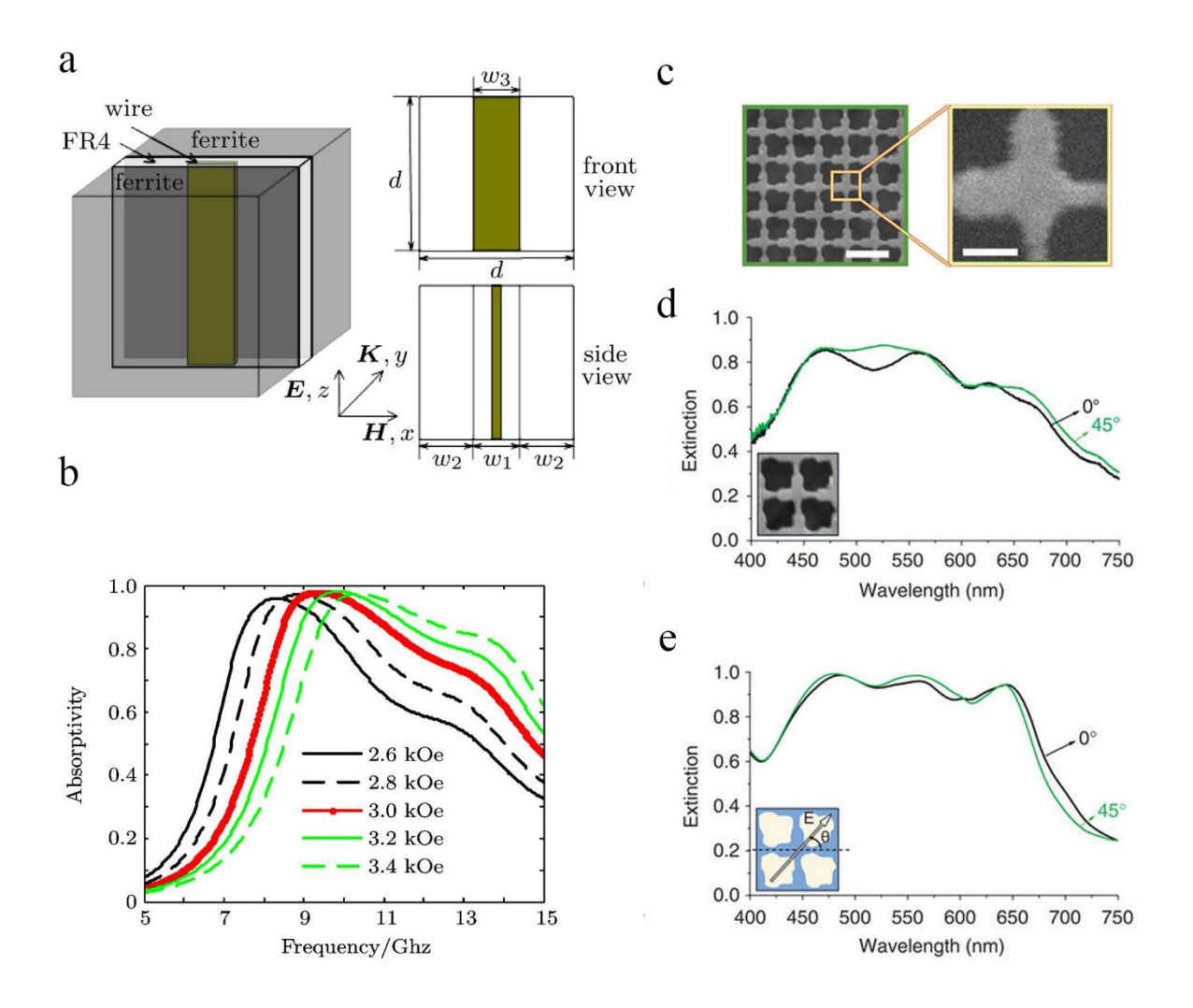


Figure 12. (a) Schematic diagram of the ferrite—wire BMMPA unit cell. Front view, side view, and structure parameters are presented; (b) The absorption bands under different magnetic biases. (c) SEM image of the fabricated crossed trapezoid arrays (left) and a single unit cell (right). Scale bars are 500 and 100 nm, respectively; (d) Measured, and (e) simulated extinction spectra using digitized SEM images (inset) for different incident electric field polarization angles (inset). a and b: Reproduced from Ref.^[119] with permission from IOP publishing, copyright 2012. c-e: Reproduced from Ref.^[24] with permission from Springer Nature, 2011.

2.4.4 Crossed trapezoidal resonators

For applications in the next generation of electronic devices for photovoltaics, ^[24, 127] photoelectrochemical water splitting, ^[128] photodetectors ^[30] and thermal engineering, ^[129] there is a need to address the requirement of reducing fabrication complexity and material consumption. Ultrathin BMMPAs based on cross-trapezoids have been theoretically and experimentally demonstrated. ^[24, 120] Koray Aydin *et al.* proposed ultrathin planar plasmonic super absorbers composed of crossed trapezoidal arrays that are capable of absorbing light from 400 to 700 nm with a measured average absorption of 71%, ^[24] as shown in **figure 12(c)**, **(d)** and **(e)**. While a different transversal resonance is excited at each width along the trapezoid under TE polarization, broadband extinction for TM polarization is rooted in the resonant electromagnetic responses of different cross-sections of the trapezoids at different wavelengths. Therefore, these BMMPAs have the potential of leveraging their optical properties to address the intrinsically weak absorption of ultrathin non-structured materials when realizing super-absorbers with atomic-scale control.

2.4.5 Resonator material tailoring

BMMPAs can be fabricated with resonators made of low bandgap materials, highly lossy metals, MXene or coupling with epsilon-near-zero (ENZ) material. A 50 nm thick BMMPA structure with a Ge (low bandgap) nanobeam on the top demonstrated broadband absorption from 400 to 900 nm, as shown in figure 13(a) and (b). Since noble metals in MMPA, e.g. Au, Ag, Pd, usually create narrow absorption peaks, they can be replaced by highly lossy metals for broadband absorption, such as W, Cr, Ni, Ta. For instance, we reported a narrow MMPA based on Au rings operating in the near and far infrared region, while another group reported a BMMPA with broadband absorption higher than 90% from 1.00 to 2.43 THz by using a highly lossy Cr ring. Due to the coupling between the gap plasmon mode of a metasurface and a ENZ mode in the nanoscale ITO film, a BMMPA with Epsilon-Near-Zero material has shown broadband and perfect absorption resonance. The system, depicted in figure 13(c), incorporates a 12 nm thick ENZ ITO layer between the patterned gold nanodisks and the SiO₂

layer, showing a 240 nm broadband, flat-top perfect (>98%) absorption centered at 1550 nm, while the traditional MMPA demonstrated only a narrow absorption, as shown in **figure 13(d)**. [77] Plasmonic resonances in nanostructured Ti_3C2T_x MXene have been manipulated to achieve aborption over a broad bandwidth of ~1.55 μ m, as shown in **figure 13(e)** and **(f)**. This can be attributed to strong LSPRs at near-infrared frequencies and the optical losses inherent to Ti_3C2T_x .

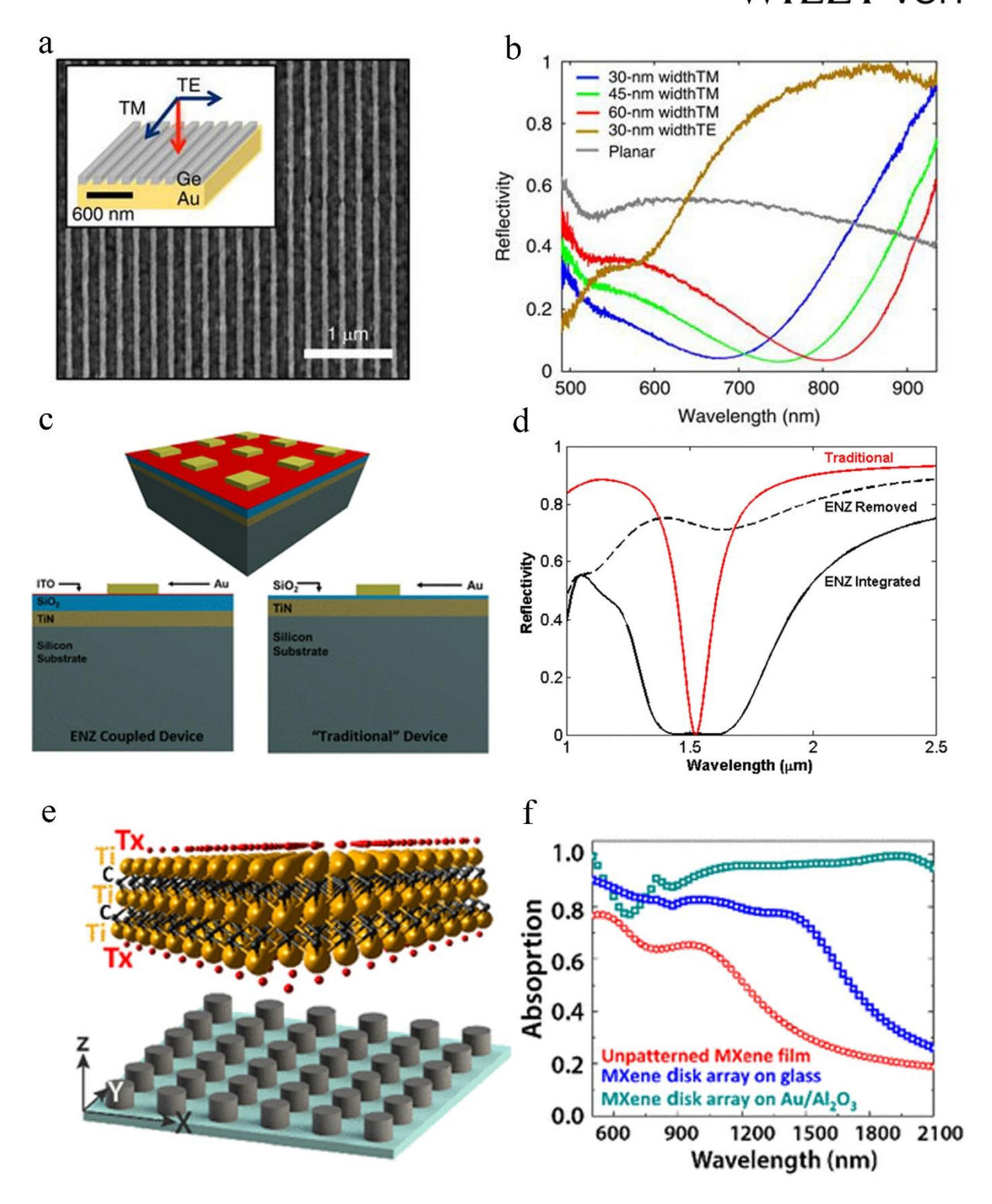


Figure 13. (a) Top-view SEM image of a fabricated metafilm with Ge beams, with a 200-nm-period and 0.3-duty cycle. Scale bar, 1 μ m; (b) Measured reflectivity spectra for TM polarized light for metafilms constructed from nanobeams with a width of 30 (blue), 45 (green) and 60 nm (red). The reflectivity spectra for TE polarized light of the array with 30-nm-wide beams (brown) and a planar Ge film (grey) are shown for reference. (c) Schematic (top) and cross section of the device consisting of a TiN metallic thick film, a SiO₂ dielectric layer, an ITO nanofilm,

and a patterned periodic array of metal squares, all on top of a Si substrate, and a schematic of a reference "traditional" perfect light absorber without an ENZ layer; (d) Simulated reflectivity curves for a perfect absorber with integrated ENZ (solid black line), absorber without ENZ layer (dashed black line), and an optimized "traditional" gap-plasmon perfect light absorber without ENZ layer (solid red line). (e) Schematic of the BMMPA fabricated using two-dimensional titanium carbide (Ti₃C₂T_x) MXene; (f) Comparison of experimental absorption spectra of the two types of disk arrays and unpatterned MXene film (incident light is TE polarized; angle of incidence is 20°). a and b: Reproduced from Ref.^[130] with permission from Springer Nature, 2015. c and d: Reproduced from Ref.^[171] with permission from American Chemical Society, 2018. e and f: Reproduced from Ref.^[77] with permission from American Chemical Society, 2018.

In this section, we have first reviewed the mainstream methods used to achieve broadband absorption operating from UV to microwave frequencies. By integrating differently sized resonators on the xy plane, the absorption bandwidth widens as the number of distinctly sized resonators increases. Another advantage is that the broadband absorption can be tuned as the size changes. However, due to the relatively small cell size required to obtain large enough densities of each resonator, the number of resonators that can be incorporated within the same unit cell is limited. Therefore, the broadening effect based on this type of integration is, to some extent, limited to a finite bandwidth. In comparison, vertical stacking of the resonators does not have a limitation on the number of integrated resonators. Hence, their absorption bandwidth can be much broader, although there is a trade-off between thinness and the bandwidth of the absorber. Intuitively, absorbers with more layers require complicated fabrication steps and the use of complex fabrication tools. Nevertheless, by exploiting slow light effect ultrathin layers that do not individually support localized resonances can be stacked relatively easily. Lumped elements can be welded in to MMPA to lower their Q-factor in the GHz region; however, they are not feasible for THz, IR or optical frequencies because of the resonator size is in the nanoscale. Nanocomposite BMMPAs can be fabricated by facile coating and sputtering; however, their broadband absorption is limited to UV, visible and NIR. Besides, broadband absorption can be achieved by adopting CMM structures, space-filling, dielectric material tailoring, crossed trapezoidal resonators and material tailoring of top resonators. To summarize this section, we have compiled table 2 and 3.

Table 2 compares advantages and disadvantages of four main methods discussed above, including fabrication method, operating frequency and cost. **Table 3** compares different methods of BMMPA design, including data on the reported FWHM, operating frequency, resonator shape/material, dielectric material, average absorption; only a few representative references are cited in the table.

Table 2 Properties of four main BMMPAs, including mechanism, working frequency, fabrication and cost.

Method	Mechanism	Working frequency	Fabrication	Cost	
Planar arragement	Mutiple resonances	UV to GHz	Easy or Hard	Depends	
Vertical stacking	Mutiple resonances or slowlight Waveguide modes	UV to GHz	Hard	High	
Welding lumped elements	Reduce Q-factor	Only GHz	Easy	Low	
Using nanocomposites	Plasmonic effect	UV to NIR	Easy	Low	

Table 3. A summary of methods to achieve BMMPA; NR is not reported and NA is not applicable in the table.

Methods	FWHM	Operating frequency	Resonator shape	Resonator material	Dielectric material	Average absorption (%)	Ref.
	2.16 μm	3–5 μm	Cross	Gold	SiO ₂	≥ 50	[58]
	1.15 THz	6.24-7.04 THz	Square	Copper	SiO ₂	~ 90	[60]
	2.8 GHz	9–13 GHz	Circle	Copper	Epoxy glass	≥95	[87]
Horizontal integration Vertical stacking	NR	0.5–0.7 μm	Square hole	Gold	SiO ₂	> 95	[92]
	NR	9.79–11.72 GHz	Dendritic	NR	FR-4	≥ 90	[55]
	NR	8.3–17.4 GHz	Windmill	ITO	PET&PMMA	≥ 90	[69]
	NR	0.65-1.45 THz	SRR & disk	Gold	PDMS	≥80	[90]
	5.66 GHz	12.38–22.28 GHz	SRR & SMP	Copper	FR-4	≥ 60	[82]
	10.1 THz	31.0–37.0 THz	Circle	Gold & Graphene	Polyimide	≥ 90	[71]
	2.3 GHz	8.8–10.8 GHz	Ring	Copper	FR-4	≥80	[95]
	1.72 μm	3.0–5.5μm	Sawtooth slab	Gold	Germanium	≥95	[78]
	NR	8.37–21 GHz	Loop	Copper	TMM4	≥ 90%	[86]
	2.40 THz	4.08-5.94 THz	Cross	Gold	Polyimide	≥ 60	[89]
	NR	8–100 THz	Frustum pyramid	Graphene	n=3 ^{1/2}	~ 90	[74]
	NR	46.2–62.8μm	Ribbon	ВР	n=1.7	≥ 90	[75]
	~ 9 THz	4–12 THz	Asymmetric void	Graphene	n=2.5 ^{1/2}	≥ 90	[101]
	700 MHz.	2.2–3.0 GHz	ELC-SRR	Copper	FR4	≥ 60	[50]
	1.38 GHz	3.1–5.6 GHz	Split-coin	Copper	FR4	≥ 90	[105]
Welded with lumped elements	> 4.56 GHZ	8.87–16.47 GHz	Double-circle ring	Copper	FR4	≥ 90	[131]
	NR	7.93–17.18 GHz	Double octagonal rings	Copper	PEC	≥90	[106]
	NR	8.45–9.3 GHz 9.2–10.45 GHz	Jerusalem-cross	Conductor	FR4	≥ 90	[110]
Nanocomposite	NR	400–2500 nm	NA	Ag NPs	Teflon AF [*]	≥ 60	[114]
	NR	Visible range	NA	Au NPs	SiO ₂	~ 100	[11]
	NR	Visible range	NA	Cu NPs	PTFE	≥ 97.5	[76]
СММ	NR	1.3–2.5 μm	Sheet with square hole	Molybdenum	SiO ₂	NR	[35]
GA	NR	1.77–4.81 μm	GA-based	Palladium	Polyimide	≥ 98	[65]
Fractal space-filling curve	1.3 THz	0.5–1.8 THz	Hilbert curve	Aluminium	n=3 ^{1/2}	≥ 90	[123]
Resonator material tailoring	> 1.55 μm	500-2500nm	Disk	Titanium Carbide	Al_2O_3	~ 90	[77]



Crossed trapezoidal arrays	NR	400–700 nm	Crossed trapezoid	Silver	SiO ₂	≥ 71	[24]
Lossy metal	1.94 THz	1.0-2.43 THz	Ring	Chromium	Polyimide	≥ 90	[67]

3. Applications of BMMPAs

The last decade has witnessed a proliferation of BMMPAs for diverse applications, including solar PV, photodetection, bolometry and the manipulation of mechanical resonances. Compared with their traditional counterparts, they have shown superior properties such as polarization-independent, insensitive to incidence angle and perfect absorption with tunability and broader bandwidth. Benefiting from advanced, cost-effective micro machining technology, BMMPAs can to be further applied to devices based on photoacoustic, photoelectric, photothermal and photomagnetic effect. In the subsections that follow, we will review specific examples of applications for BMMPAs.

3.1 BMMPAs for solar photovoltaics

Solar PV systems are considered as ideal candidates to harvest solar radiation. As commercial PV devices approach to the detailed balance limit, the requirement for cost-effective solar cells is to achieve high efficiency with less material consumption. In the past decades, light trapping schemes were proposed to enhance the light absorption of solar cells. [111, 132] However, their intrinsic defects hinder their large-scale production, e.g., degradation of open circuit voltage of quantum dots solar cells, [111] surface recombination of nanowire solar cells. [133] The current thin film PV systems need less material, but their disadvantage lies reduced absorption due to the reduction absorber layer. Hence, light trapping scheme is critical for thin film solar cells. Details for light trapping techniques, along with the working principles and physics of PV cells are given in Ref. [133, 134]. The light trapping ability of BMMPAs can be applied to both solar thermo-photovoltaic (STPV) devices and ultrathin solar cells.

The main challenges in direct utilization of plasmonic resonance absorption of solar energy in the visible range are significant Ohmic losses and their consequential heating. An attractive route to avoid the adverse consequences of plasmonic overheating from direct visible absorption is to utilize STPVs, as shown in **figure 14**. STPV is a conversion process from heat to electricity via photonic reemission.

Due to its broadband absorption ability, a BMMPA can be applied on STPVs to address their poor absorption. The STPV systems have been widely investigated due to the theoretical models that predict up to 85% efficiency [129]. Under a suitable light concentration scheme, and with a reasonable ratio of areas between the emitter and absorber, the efficiency of a STPV system adopting an absorber (tungsten pyramids)-emitter (tungsten slab) pair with a single-junction solar cell can exceed the Shockley-Queisser (SQ) limit. [135] The theoretical limit of an STPV system with solar absorber/narrow-band thermal emitter structures was also calculated to be 41%, which is higher than the SQ limit of 31% [12]. The efficiency remains above 31% for an emitter temperature (Te) > 1200 K when a heat reservoir is included in the STPV system design, extending the power-generating period beyond the daytime.

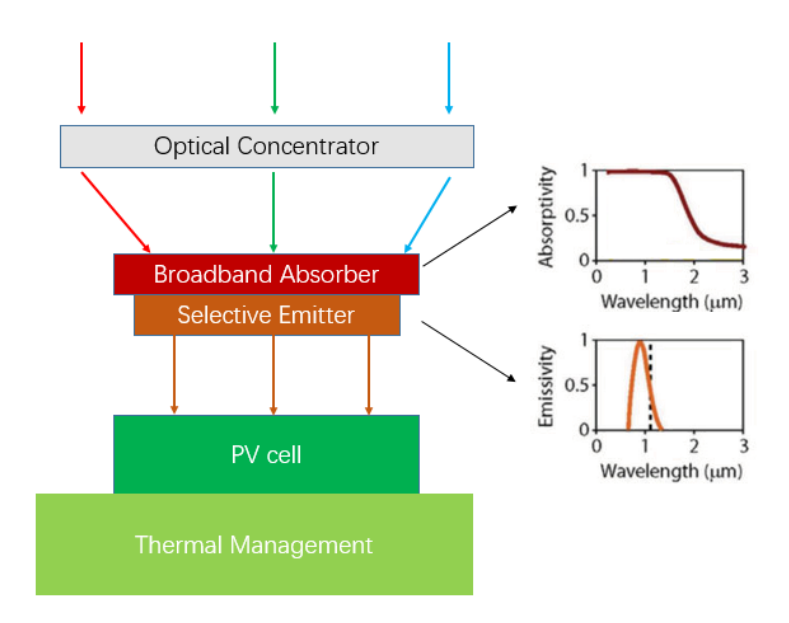


Figure 14. Schematic of STPV systems. The absorber and emitter typically operate above 1000 K while the PV cell operate at room temperature.

The key design goals in creating an absorber for STPV application are: broadband high absorption covering UV, visible and NIR region along with zero emittance in the mid-IR regime to minimize energy loss from spontaneous thermal radiation; independence on the angle of incidence and polarization of incoming light. Extensive efforts have been focused on achieving ideal STPVs with BMMPAs. Square rings with four gaps are tailored to obtain polarization angle independent BMMPAs for solar

application in the microwave, infrared and visible regime.^[84] Most of the previous designs on MMPAs work at room temperature, but the temperature-dependent optical properties of BMMPA have to be fully investigated in order to understand their thermal dependence while harvesting efficient solar energy. Chou et al. demonstrated a thermally stable selective solar absorber made of 2D metaldielectric photonic crystal structures after 24h heating at 1000 °C. [136] Wang et al. experimentally demonstrated a highly-efficient MM selective absorber for solar thermal energy harvesting, working at temperatures up to 350 °C. [64] The structure is composed of a 2D Ti grating, MgF₂ dielectric layer and a tungsten film, depicted in figure 15(a), (b), (c) and (d). Their absorbance within the solar spectrum is higher than 0.9 and a low emittance of 0.2 in the mid-IR regime as shown in figure 15(e). While a black surface could only convert 32% of solar energy to useful heat at 100°C and would drop quickly to zero at 125°C, the final solar thermal conversion efficiency of the absorber could reach 78.1% under 1 sun (i.e., no optical concentrator) at 100 °C, monotonically dropping to zero at the stagnation temperature of 241 °C, as compared in figure 15(f). The solar-to-heat conversion efficiency can be further boosted by using concentrators. Figure 15(g) shows that the measured conversion efficiency of an absorber at 400 °C can reach 21.5% under 5 suns, 57.4% with 10 suns and 80% with 25 suns. However, the efficiency of a black surface only changes from 93% to 98% at the same temperature from 1 to 100 suns.

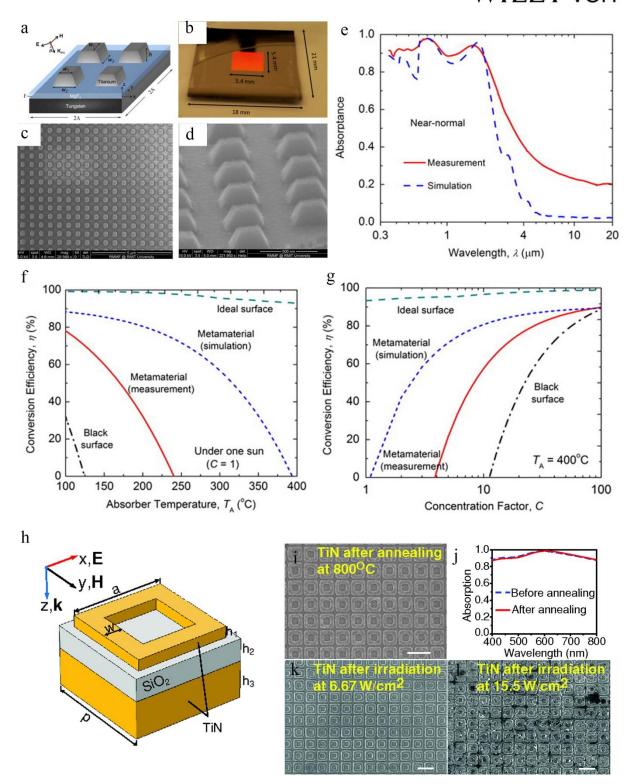


Figure 15. (a) Structure schematic for proposed MM solar absorber. K_{inc} represents the incident wavevector, and the incidence angle θ is defined as the angle between K_{inc} and the surface normal. The plane of incidence (POI) is defined as the xz plane. The E field is in the POI for TM incidence, while it is perpendicular to the POI for TE incidence; (b) A photo of the fabricated sample for optical characterization. SEM images of the fabricated absorber sample from (c) top view and (d) side view; (e) Measured and simulated room-temperature spectral

absorptance of the MM solar absorber; (f) Predicted solar-to-heat conversion efficiencies of an ideal selective surface, the MM solar absorber (with optical properties either measured or simulated), and a black surface as a function of absorber temperature absorber temperature (T_A) under 1 sun; (g) Solar-to-heat conversion efficiency for all three surfaces as a function of concentration factor C at an absorber temperature of T_A =400 °C. (h) Schematic representation of a unit cell of the three-layer TiN MMPA with dimensions of a = 250 nm, w = 50 nm, p = 300 nm, h_1 = 30 nm, h_2 = 60 nm, and h_3 = 150 nm; SEM image (i) and the measured absorption (j) of the TiN absorber after annealing at 800 °C for 8h, as well as the reference measured absorption of TiN before annealing; SEM images for the TiN absorber after being illuminated by a laser with an intensity of 6.67 W/cm² (k) and 15.5 W/cm² (l). a-g: Reproduced from Ref. [64] with permission from Elsevier B.V., copyright 2015. h-l: Reproduced from Ref. [16] with permission from John Wiley & Sons, copyright 2014.

Noble metals are indispensable in creating BMMPA structures, but they suffer from low melting points. STPV systems usually operate at 800 °C or higher, thus approaching or surpassing the melting points of bulk Au (1063°C), Ag (961°C) and Al (660°C). [137] Ni has a high melting point (1455°C) but its absorption performance is usually limited. Furthermore, the melting point of the patterned metallic structures at the nanoscale is greatly lowered due to the small size effect. [138] Therefore, refractory metals with high melting points are selected to be used in STPVs, such as tungsten (W, 3422°C), [137, 139, ^{140]} molybdenum (Mo, 2623°C)^[140, 141] and tantalum (Ta, 3020°C). ^[135, 142] Using Ta, an integrated doublesided 2D photonic crystal (PhC) absorber/emitter pair is demonstrated for a high-performance STPV systems. [135] At an irradiance of 130 kW m⁻², the PhC absorber demonstrates more than a two-fold improvement in measured STPV system efficiency (3.74%) relative to a nearly blackbody absorber (1.60%). However, W, Mo and Ta are not good absorbers in the visible range due to their large impedance mismatch and thus cannot effectively cover the solar spectrum. Li et al. adopted TiN to fabricate a BMMPA with an average absorption of 95% over the range of 400-800 nm after annealing at 800°C for 8h, [16] indicating its promise for applications in STPV systems, as shown in figure 15(h), (i) and (j). On the other hand, a Au absorber is greatly damaged when illuminated under the laser intensity of 6.67 W/cm², as can be seen from figure 15(k) and (l). TiN absorber can remain stable under a laser illumination of 6.67 W/cm², but is somewhat damaged at the illumination intensity of 15.5 W/cm².

In addition to high thermal stability, another relevant issue for BMMPAs in solar applications is Ohmic loss. Ohmic loss and the resulting material heating lead to a decrease in efficiency. [143] Metallic nanostructures operating at optical frequencies suffer from larger Ohmic losses than those working at lower frequencies, because the geometric skin depth is larger than bulk skin depth and the larger absorption cross section induces strong currents. This is a problem not only facing the STPV systems, but also MM solar cell structures. Güney *et al.* demonstrate that Ohmic losses in MMs can be reduced by geometric tailoring, such as by increasing the radius of curvature at sharp corners. [144] In this study, the so-called bulk skin depth technique (BSDT) was proposed to reduce the geometric skin depth at optical frequencies to reduce the Ohmic losses by offering three advantages: (1) optical absorption in the metallic structure (i.e., Ohmic loss) is shifted into the semiconductor, with increased optical absorption useful for solar energy conversion; (2) reduced Joule heating; (3) additional interconnections can be added in the system without destroying or short-circuiting the absorber.

In conclusion, BMMPAs play a critical role in enhancing absorption for PV applications. The challenge is how to design high-temperature, resistive absorbers while maintaining low Ohmic losses. In addition to the absorber, a narrow bandwidth selective emitter needs to be carefully designed to maximize efficiency. [145] As of today, an efficient solar absorber with both spectral selectivity and high-temperature compatibility is still lacking. Nonradiative decay of surface plasmon in BMMPAs is a parasitic process, but recent studies have shown that it can be harnessed in the form of hot electrons for photovoltaics, [146] photocatalysis [147] and photodetection. [148] Unfortunately, the quantum efficiency of devices based on hot electrons is still low due to poor electron injection.

3.2 Photodetection with high responsivity

Recent studies have shown that photodetection can exploit the hot electrons generated from SP or LSPR nonradiative decay, providing a chance for using MMs in photodetection.^[30, 148, 149]. In metal-dielectric interfaces, a Schottky barrier is formed, as shown in **figure 16**. The hot electrons from SP nonradiative decay can be transported to the junction interface, where they can be injected into the band of semiconductor before thermalization if they have enough energy. The bandwidth is limited by

Schottky barrier height rather than the bandgap of the semiconductor ^[148]. If one can obtain a broadband absorption at energies beyond the bandgap of the semiconductor, a broadband photodetector can be realized. Therefore, there are two advantages in using MMPAs as photodetectors: (1) providing hot electrons to detect photons below the bandgap of the semiconductor; (2) enhancing light absorption by incorporating a MMPA with larger light interaction cross sections than the semiconductor.

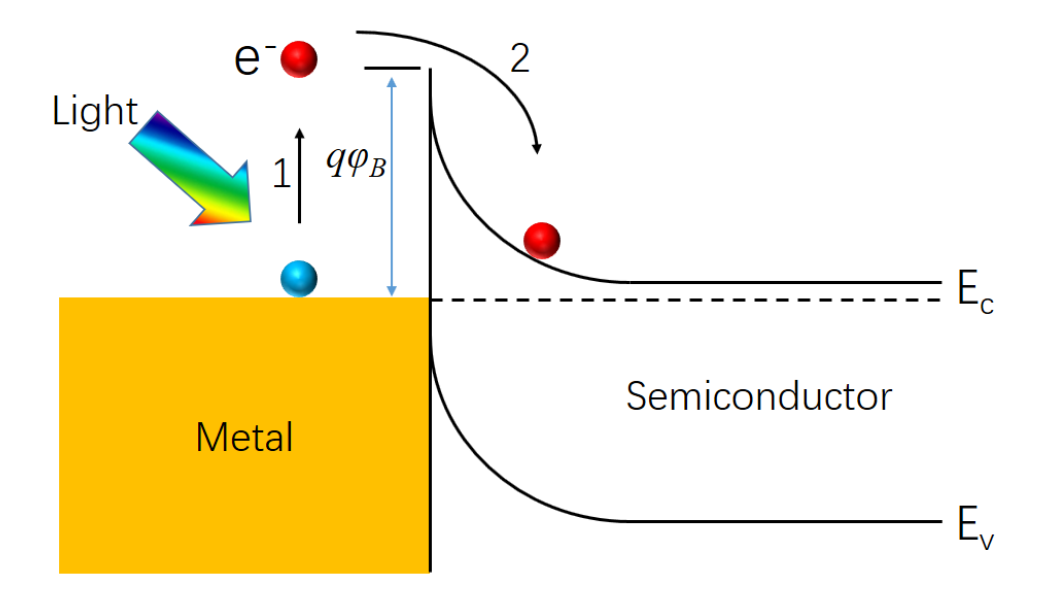


Figure 16. Energy band diagram for plasmonic hot electrons over a metal–semiconductor Schottky barrier, $q\phi_{B}$.

However, SPs and LSPRs are intrinsically narrow therefore only allowing limited detection bands. Some groups have demonstrated photodetectors based on BMMPA to circumvent the narrow bandwidth. Valentine *et al.* first demonstrated a BMMPA detector composed of bipartite checkerboard supercell, as shown in **figure 17(a)** and **(b)**. It maintains absorptivity over 80% from 1250 to 1500 nm, as shown in **figure 17(c)**. A peak absorptivity above 90% is maintained for incident angles of up to 75 and 60° under p- and s-polarized illumination, respectively. Due to the presence of ultrathin BMMPA structure, the efficiency of hot electron transfer process is significantly enhanced, its FWHM is up to 800 nm and photoresponsivity is larger than 1.8 mA/W from 1200 to 1500 nm, as shown in **figure 17(d)**. ^[148] In the same year, Chen-Chieh *et al.* proposed a new concept for the development of a BMMPA photodetector in the telecommunication region: deep-trench/thin-metal (DTTM) active antenna structures that

enhance the photoresponsivity of Si beyond the band edge, as shown in **figure 17(e)**. ^[30] The peak value of absorbance for the DTTM arrays (88%) was four times and one order of magnitude larger than those of nanoantennas and dot/hole arrays, respectively, as compared in **figure 17(e)**. The photoresponsivity curves demonstrated higher responsivities in the shorter wavelength regime, gradually decreasing when increasing the wavelength of the incident light, as shown in **figure 17(f)**. Distribution of photocurrents to reconstruct an image of the letters 'NTU', are shown in **figure 17(g)**, as recorded at an intensity of 1.2 fW/ μ m² at a wavelength of 540 nm, 4.7 pW/ μ m² at a wavelength of 1310 nm and an intensity of 4.57 pW/ μ m² at a wavelength of 1550 nm, respectively. Therefore, Si-based DTTM devices displayed excellent ability for photodetection beyond the bandgap of Si.

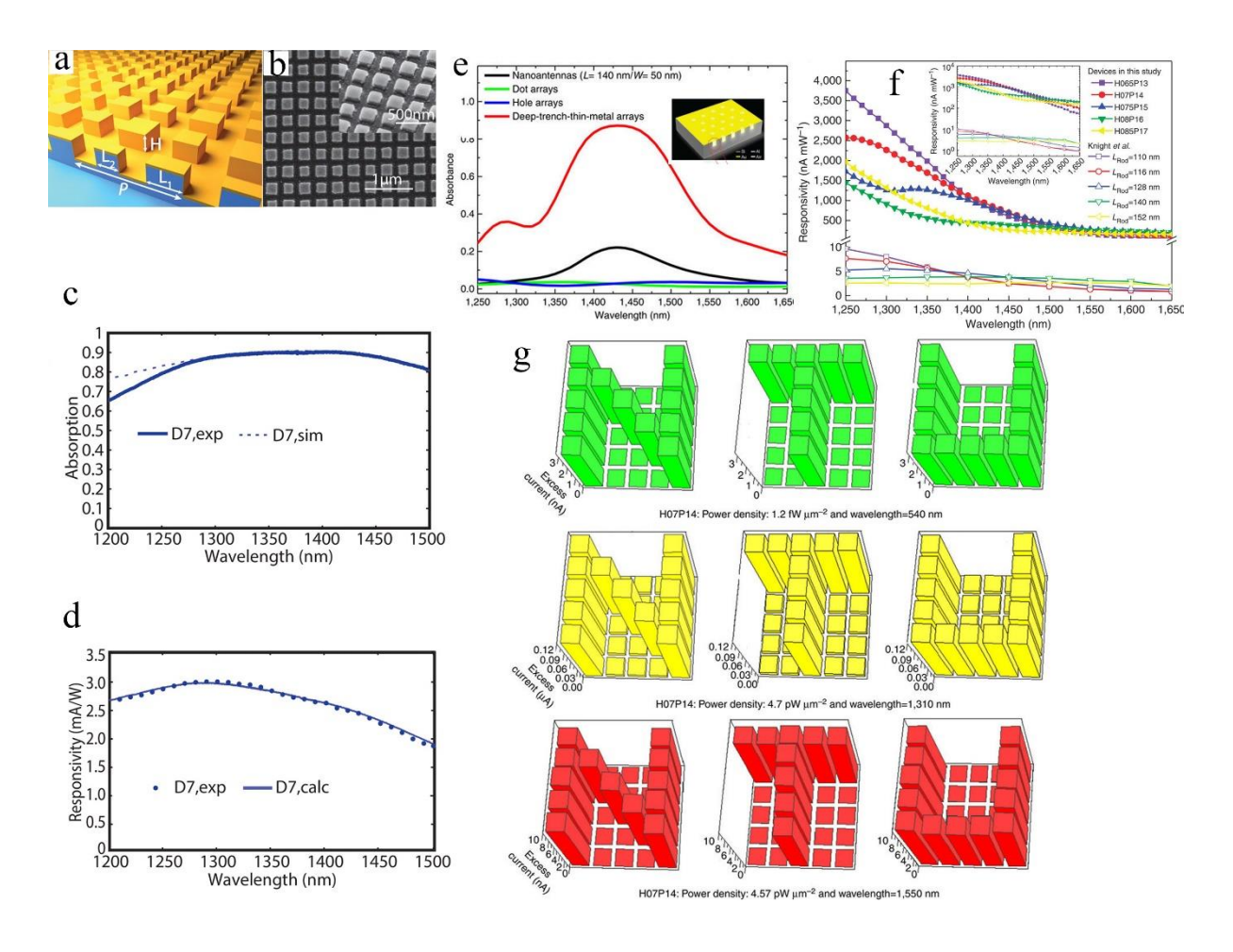


Figure 17. (a) Schematic of the BMMPA photodetector. The dimensions of the photodetector are L_1 = 185 nm, L_2 = 225 nm, P = 680 nm, H = 160 nm; (b) SEM image of the fabricated device; (c) Experimentally measured (solid) and simulated (dashed) absorption spectra of the BMMPA detector; (d) Experimentally measured (circles) and calculated (line) photoresponsivity spectra of the BMMPA photodetector. (e) Simulated absorption spectra of

the four types of antenna structures. Among them, the DTTM arrays exhibited the largest absorption in the broadband regime. The inset is the illustration of the detector structure; (f) Responsivity spectra of the proposed DTTM devices, in comparison with the nanoantenna-based devices reported by Knight *et al.* [150]; (g) Bar charts displaying excess current obtained by the H07P14-containing DTTM device under an applied bias voltage of 0 V, detected at wavelengths of 540, 1310 and 1550 nm. The images were constructed based on the existence or absence of a photocurrent during the point-by-point scanning of the DTTM device. Clear images of the capitalized letters 'NTU' were obtained, even though the incident power density was low; in particular, 4.7 pW/ μ m² at a wavelength of 1310 nm and 4.57 pW/ μ m² at a wavelength of 1,550 nm. The pixel size is 5 mm. a-d: Reproduced from Ref. [148] with permission from American Chemical Society, copyright 2014. e-g: Reproduced from Ref. [30] with permission from Springer Nature, copyright 2014.

The excitation of hot carriers through plasmonic effect is a very fast process, [151-153] thus offering an additional advantage for the creation of high speed photodetectors. Importantly, the generation rates of this non-thermal carriers (**figure 18(a)**) can be greatly increased by enhancing the field in the metal structures. Regions with large field enhancement (hot spots), generated either by the geometry of specific nanoantennas^[152, 154] or by the near-field interaction of neighbouring structures, [151, 152] drive larger rates of generation of hot carriers. **Figure 18** shows selected results from two different studies that illustrate these two characteristics of the generation of hot carriers: the ultrafast nature of their excitation and the relevance of the hot spots in exciting them. These studies employ pump-probe measurements to study the carrier dynamics in MM composed of Au nanodisks^[151] or Au and Ag NPs^[152] on top of a gold layer, separated in both cases by a dielectric spacer layer of various thicknesses. The spacer thickness changes the intensity of interaction between the top nanostructures and the gold layer. Thinner spacers increase the field enhancement in the system and give rise to hot spots, as the simulation results show in **figures 18(c)** and **(d)**. When this occurs, highly non-thermal hot carriers are generated in high densities, creating a strong fast transient signal that attenuates very rapidly as the carriers thermalize. This can be seen in figures **18(b)** and **(e)**.

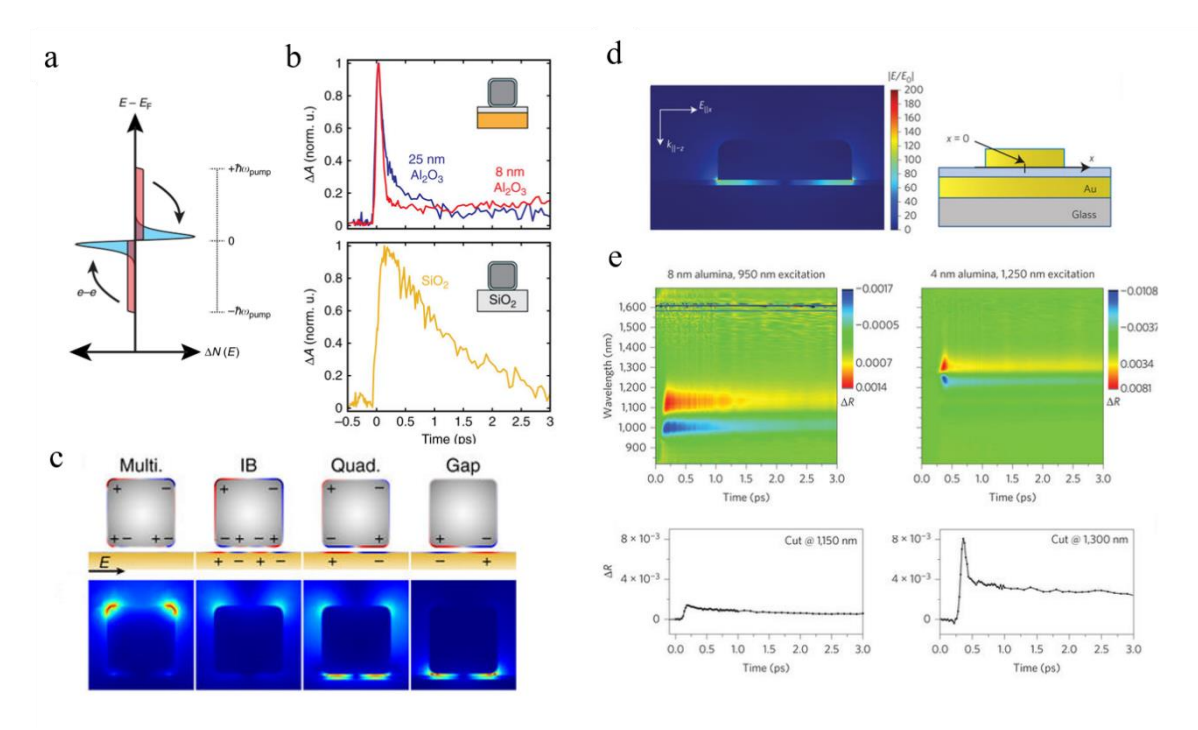


Figure 18. (a) Hot electron distribution from plasmon excitation. Nonthermal (red) carriers initially form a symmetric step-wise distribution relative to the Fermi energy upon excitation. After electron-electron scattering, a thermalized electron population (cyan) with a Fermi-Dirac distribution is formed from the nonthermal electrons, with an electronic temperature above that of the lattice. (b) (top) Kinetic trace of normalized differential absorbance for Ag nanocubes on an 8 nm Al₂O₃ spacer compared to a 25 nm Al₂O₃ spacer at the gap resonance and (bottom) to bare Ag nanocubes on SiO₂ in transmission mode, which exhibits no ultrafast (~100 fs) decay of the response, arising from the relaxation of highly energetic nonthermal carriers. (c) Cross section of the surface charge (top) and electric field profiles (bottom) at the peaks of the interband (IB) transition and plasmon modes for an electric field oriented in-plane. The field strength scale is up to 20x free space for the multipolar (Multi) mode, IB transition, and quadrupolar (Quad) mode and 100× free space for the gap mode. (d) (left) Electromagnetic field distribution inside the nanostructure (defined as $|E/E_0|$), showing strong plasmonic hot spots at the edges of the nanodisk and (right) geometry of the system; (e) Two-dimensional map of the time evolution of the plasmonic spectral change in 8-nm-thick (left) and 4-nm-thick (right) alumina spacer samples, and (bottom) cuts at 1115 nm (left) and 1300 nm (right) showing the time dynamics of the corresponding data in the above panels after excitation of the plasmon. The time dynamics in the 4-nm-thick spacer are drastically different to the thicker spacer, with a new ultrafast component following the excitation near its resonance at

950 nm. **a-c**: Reproduced from Ref. ^[152] with permission from Springer Nature, copyright 2017. **d** and **e**: Reproduced from Ref. ^[151] with permission from Springer Nature, copyright 2015.

Enhanced generation of hot carriers through plasmonic excitation depends on the intensity of electric field in the metal, thus the importance of hot spots and small sizes, [151, 155, 156] but especially at the surfaces of the NPs or films. This is not only to facilitate their injection through the Schottky barrier, a point discussed below, but also to directly increase the rate of generation of hot carriers by surface effects. These constrain the coherent excitation of the electron cloud in the plasmon, inducing electron-surface collisions with transitions that do not conserve linear momentum of an electron. [155, 156] The relevance of the NP surface in this process highlights the importance of its geometry, which can generate intense hot spots without the need for interparticle interaction by adding sharp features or tips, such as in nanostars or nanocubes. [154, 156-158] Furthermore, small NPs have a larger surface-to-volume ratio, thus offering a higher relative generation rates of hot electrons. [156, 158] Although small NPs by themselves may not provide a wide spectral interaction profile, they can be used to sensitize an ensemble of larger resonators in interaction, or in a polydisperse and interacting sample. [159]

A variety of different photodetector designs use hot carriers generated by plasmonic excitation, $^{[30, 148, 160]}$ including the combination of metal antennas with 2D materials serving as a collecting layer for the exited carriers. $^{[161]}$ A recent example of a planar BMMA that takes advantage of the hot spot effect is presented by L. Wen *et al.*, who covered a disordered planar collection of Si nanoholes (SiNH) with a thin layer of Au, $^{[162]}$ as depicted in **figure 19(a)**. In this system, besides the excitation of modes resonant on the cavities of the top layer, the inter-hole interaction promotes excitation of electrons through hot spots, as illustrated by **Figures 19(b)** and **(c)**, which show the simulated electric field distribution. With this approach, they achieved absorptions greater than 80% across a bandwidth of approximately 1 μ m (wavelengths from 1100 to 2000 nm), as shown in **figure 19(d)**, due in part to the variety of sizes of the nanoholes on the surface. At the same time, this irregular planar layout makes the device strongly polarization-independent. This stands in contrast with most of the designs discussed in this review, which typically have periodic patterns. Another example of this kind of design has been reported by Lu

et al., showing a hot electron photodetector with a collection of polydisperse gold NPs separated from a gold film by a TiO_2 spacer, as shown in **figure 19(e)**, effectively covering the entire visible spectrum.^[159] **Figure 19(f)** shows the experimental results, compared with equivalent systems without hot spots, which evidence an absorption of at least 80% at wavelengths ranging from 400 to 700 nm.

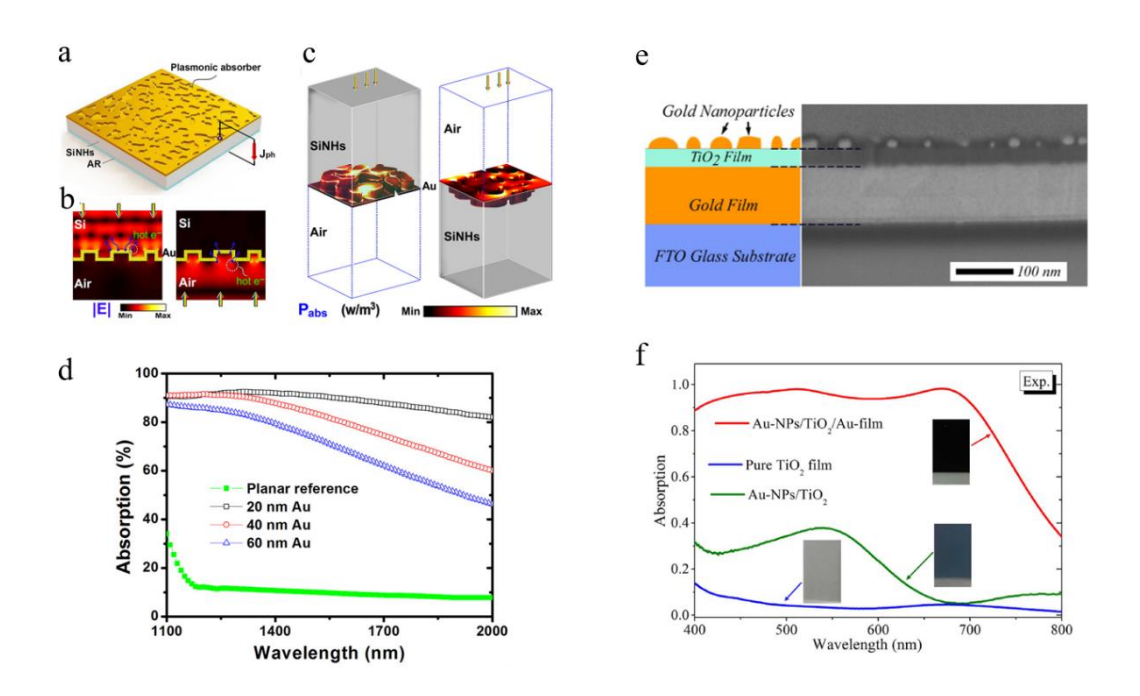


Figure 19. (a) Schematic of the proposed plasmonic hot electron photodetector; (b, c) Field and volumetric power absorption (P_{abs}) distributions of the device operating at the front and back-illumination modes, from simulations replicating a typical morphology of Au/SiNHs from the experiments; (d) Measured absorption spectra under back illumination of the Au/SiNH devices with different thicknesses of Au coatings. The result of a planar reference device with 20 nm thick Au deposited on nonstructured sample is also included. (e) (left) Schematic of the metal-dielectric-metal nanostructure that is composed of (from bottom to the top) a FTO glass substrate coated with an optically thick Au film (~150 nm) followed by a thin TiO₂ film acting as the spacer layer and at the very top, a monolayer of Au NPs with random size dispersion and spatial distribution. (right) Side-view SEM image of the optimized Au-NPs/TiO₂/Au-film nanostructure prepared with a 5-nm-thick Au film pre-deposited on a 50-nm-thick TiO₂ spacer layer; (f) Experimentally measured absorption spectra of the Au-NPs/TiO₂/Au-film nanostructure, the pure TiO₂ film, and the Au-NPs/TiO₂ nanostructure. The insets show the photographic images of the prepared samples. a-d: Reproduced from Ref. [162] with permission from American Chemical Society, copyright 2017. e and f: Reproduced from Ref. [159] with permission from Springer Nature, copyright 2016.

As mentioned above, thermalization of these highly energetic carriers also happens in a very short timescale, which decreases the likelihood of successful injection into the semiconductor when the carrier is not excited close enough to the metal-semiconductor interface. [156, 158, 163] Moreover, the direction of the carrier momentum is also important: if, for simplicity, we consider it as a ballistic particle, it is clear that it has to travel towards the metal-semiconductor interface in order to traverse it. Then, in order to maximize the number of harvested hot photocarriers, some of the mentioned planar BMMA designs have sought to increase the interfacial area and decrease the width of the metal layer. Complementing this notion, Knight *et al.* have discussed the possibility of embedding the metal pattern into the semiconductor, with the goal of capturing a larger proportion of excited carriers by allowing additional regions in the momentum space to traverse to the semiconductor or, in other words, adding additional Schottky barriers at additional directions. [164] This idea allows a broader range of polarizations to be excited for a given metal pattern geometry.

In summary, MMPA designs that rely on the generation of hot carriers can be harnessed to create fast and sensitive photodetectors. To create efficient devices, the two key requirements are to use geometries and materials that provide large generation rates of these highly non-thermal carriers, and to provide means to maximize their extraction from the plasmon-supporting structure into the layers that are used to collect the photocurrents. Although some groups have shown enhanced photodetection ability in Si-BMMPA structure, further study is needed to expand this design to other semiconductor materials. Besides, leveraging SPs and LSPRs of metallic structure in the visible and NIR regions is limited by material fabrication techniques. The dimensions of the structure range from approximately 50 to 250 nm, sizes which inevitably involve complicated and expensive FIB or EBL manufacturing processes. In general, the requirements for BMMPA-based photodetection are: high responsivity, simple fabrication with CMOS compatibility, high photoresponsivity, polarization-independence, zero-bias operation, low power consumption and broadband detection.

3.3 Bolometers based on BMMPAs

To suppress dark noise, bulky cryogenic systems are required in infrared photodetectors. Thermal detectors provides portable, low-cost alternatives for IR detection or imaging at room temperature. A bolometer is a device for detecting the power of incident EM radiation via heating of a material with a temperature-dependent electrical resistance, as illustrated in **figure 20(a)**. Conventional bolometer design uses thick metal, semiconductor or superconductor as absorber to guarantee high absorption while BMMPA-based bolometer can boost its performance and decrease thickness significantly. [8, 165-169]

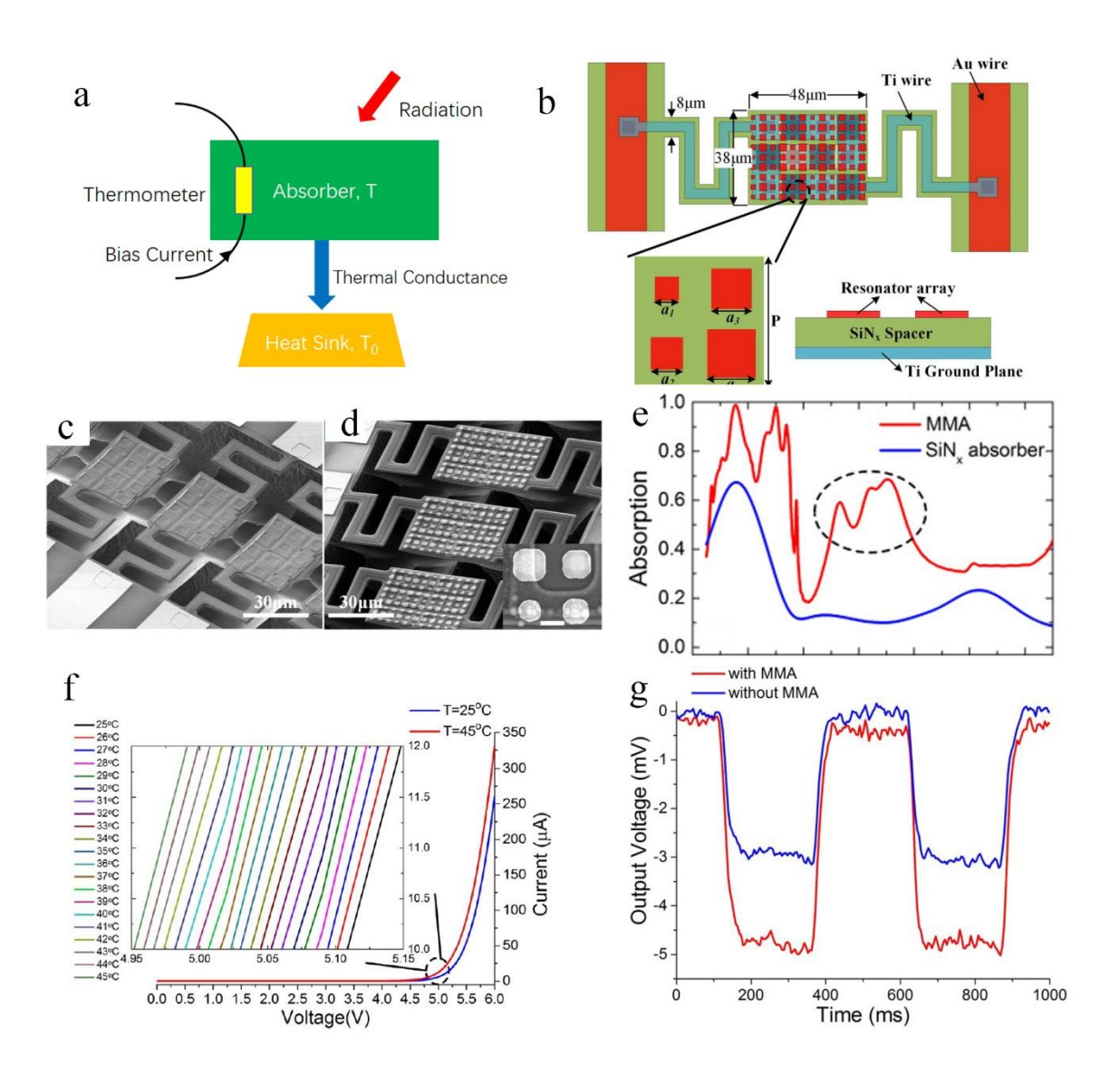


Figure 20. (a) A typical bolometer structure including a BMMPA. (b) Top view of the designed microbolometer; SEM pictures of the fabricated microbolometers (c) without and (d) with BMMPA. The zoomed-in picture in (d) is the unit cell of the resonator array (scale bar: $2 \mu m$); (e) Simulated absorption of BMMPA and the ordinary SiNx

absorber; (f) I-V characteristics of the fabricated microbolometer at the two different device temperatures of 25°C and 45°C, respectively. The inset is the zoomed-in view of different I-V curves with a 1°C step around a 10 μ A bias; (h) Transient responses of the microbolometers under modulated IR incidence at a bias current of 10 μ A. **b-g**: Reproduced from Ref. [167] with permission from Optical Society of America, copyright 2016.

Thomas Maier et al. presented an alternative integrated solution of wavelength-tunable absorption control in thermal microbolometers.^[8] Later, a proof-of-concept MMPA-based bolometer was demonstrated in 2012, operating at around 1.5 µm and exhibiting room-temperature time constants of about 134 μ s. [169] On this basis, the authors envisioned an integrated bolometer array architecture that would allow for integrated broadband spectroscopy and polarimetry without the need of any external dispersive element or polarizer. Some groups have integrated the BMMPA-based bolometer in compact photoelectric devices. [166, 167] A monolithic resonant terahertz sensor element comprising a BMMPA and a micro-bolometer was reported in 2013, with a minimum noise-equivalent power (NEP) of 37 pW/ $\sqrt{\rm Hz}$ and a thermal time constant of 68 ms.^[166] Ma et al. reported a microbolometer integrated with a BMMPA, superior to an ordinary SiN_x absorber within a broad spectral range, as shown in figure 20(b), (c), (d) and (e). [167] The MM structure yields three vaguely distinguishable peaks at 7.31, 8.43, and 9.03 µm corresponding to the resonant absorption of there square resonators with a size of 1.5, 2, and 2.5 µm respectively. The peak originating from the 3 µm size resonator is swallowed by the adjacent peak, but it can be distinguished by the field distribution, as shown in figure 20(e). The I-V curve in figure 20(f) indicates a temperature sensitivity of -8 mV/K, meaning that the junction voltage will drop by 8 mV as the device temperature rises by 1 K. The responsivity of the bolometer is characterized by the transient response of the device upon IR illumination, as shown in figure 20(g). The BMMPA shows a boost in the responsivity of the microbolometers by as high as 60% under all bias conditions investigated.

Hot-electrons are not only promising for photodetection but also presents a solution to achieve improved responsivity and NEP. Two different types of phonon cooled hot-electron bolometer (HEB) are compared: a conventional antenna coupled HEB (AC-HEB) and a novel frequency selective

bolometer with a BMMPA. [168] While the optical responsivity and NEP are \sim 6 A/W and \sim 20 pW/ $\sqrt{\rm Hz}$ for the AC-HEB, that of the BMMPA-HEBs is \sim 40 A/W and \sim 5 pW/ $\sqrt{\rm Hz}$, respectively.

Overall, part of the initial motivation to develop BMMPAs is their application in thermal detection, although integrated devices are rarely reported. Although BMMPA-based IR thermal detection demonstrates high responsivity and outperforms common detection technology without requiring heavy refrigeration systems, a challenge remains in how to bridge the gap between the BMMPA-based bolometer and mainstream CMOS technology. Further investigation need to focus on solving the compatibility of the BMMPA-based bolometer with integrated circuit fabrication process.

3.4 MMPAs for broadband manipulation of mechanical resonances

Stretching forces are commonly utilized to engineer MMPAs. For example, conductive rubber is used as a back layer for dielectric resonators. Due to the different coupling mechanism of rubber, the operation frequency of MMPA blueshifts with increasing strain parallel to the H field but becomes independent on strain variation parallel to the E field. [170] Resonant light in the MM structure can also be efficiently converted into heat based on thermomechanically coupled optical and mechanical resonances or controlling mechanical damping with light. [18, 171] BMMPA-based mechanical resonances have several benefits: very low oscillation threshold pump power, parametric mechanical oscillation over an extremely broad frequency range of optical pump frequencies (e.g., \sim 4 THz in Ref. [18]), low *Q*-factor; and does not strictly require Fano resonances.

In order to mimic real materials and support simultaneous optical and mechanical resonances, Cubukcu *et al.* demonstrated in a pioneering work that the optical and mechanical degrees of freedom of MMs can interact via heating by optical absorption, meaning that one can manipulate the mechanical damping by using light. The structure shown in **figure 21(a)** and **(b)** is composed of a bilayer gold-SiN membrane containing an array of polarization independent cross-shaped plasmonic nanoslots and a metal back-reflector. When illuminated near its resonance with a continuous-wave 1550 nm laser beam, the optical power is efficiently absorbed and converted into heat on the bilayer membrane. As shown in **figure 21(c)**, the heated membrane deflection results from the

plasmomechanical coupling when the structure is illuminated with a pump laser at ω_L corresponding to 1550 nm wavelength, tuned slightly to the red side of the Fano resonance frequency ω_0 . The absorbance will be tuned by δA due to changes in the absorber gap originating from the natural oscillation of the membrane with amplitude δx at its mechanical resonance frequency $(1/\tau_m)$, where τ_m is the period of the mechanical oscillation. The light-induced damping $\Gamma_{\rm pl} \propto \delta A/\delta x$, is able to increase or decrease the initial mechanical damping depending on its sign as shown in **figure 21(d)**. For positive resonance detuning, that is, $\omega_L < \omega_0$, $\Gamma_{\rm pl}$ is always positive, which dampens the mechanical resonance, whereas for $\omega_L > \omega_0$, mechanical amplification, i.e., gain, is possible since $\Gamma_{\rm pl}$ is always negative, as shown in **figure 21(e)**. As a result, solely by optical pumping at 210 μ W, the effective temperature of the mechanical mode can be reduced down to 48 K from room temperature, as shown in **figure 21(f)**.

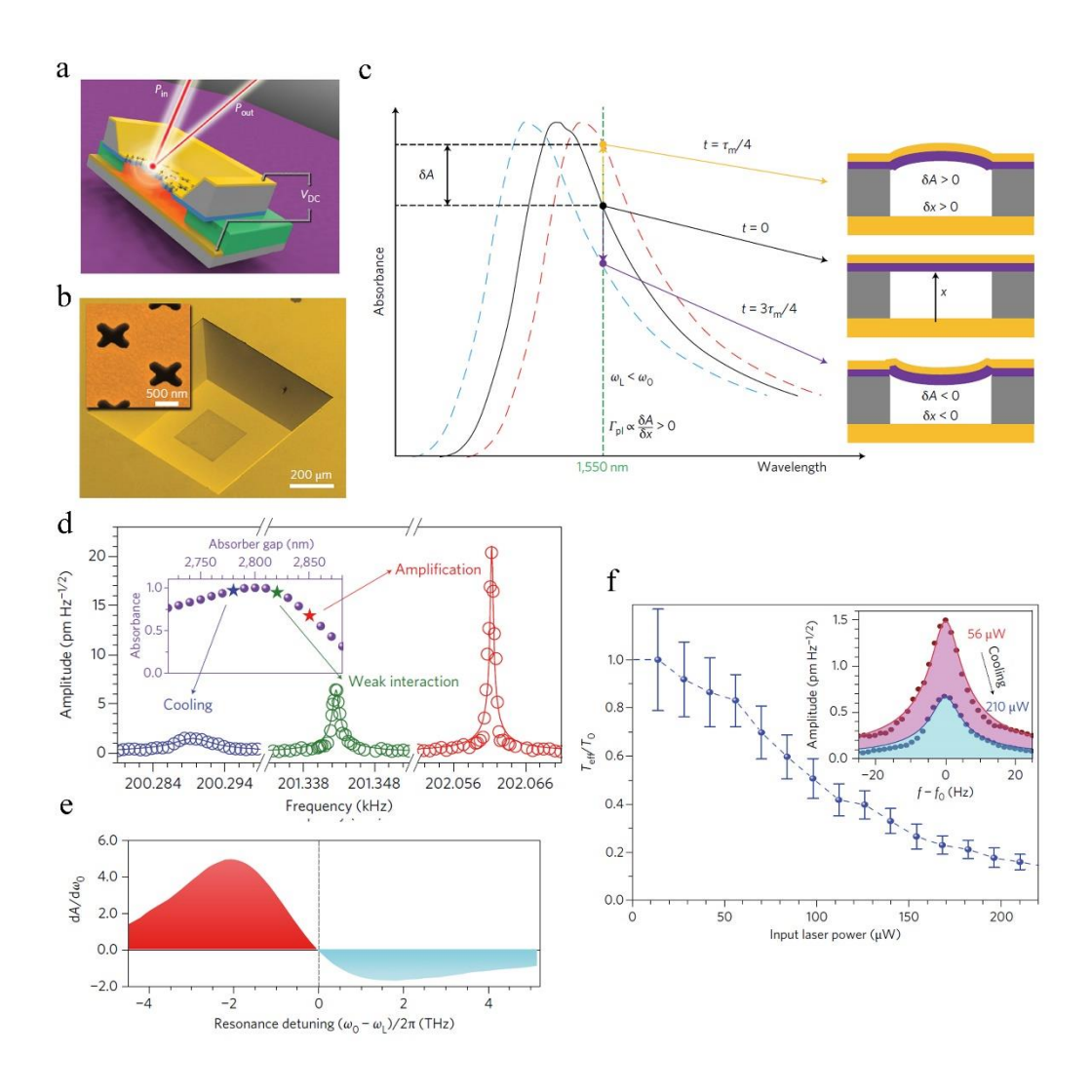


Figure 21. (a) Schematic of a MMPA with a mechanically compliant bilayer (Au (25 nm)/SiN (100 nm)) membrane component decorated with a nanoantenna array; (b) The false-color SEM image of the fabricated cross-shaped nanoslot (length (360 nm)/width (150 nm)) antenna array (period 800 nm) that covers an area of 250 µm by 250 μm at the center of the 500 μm by 500 μm membrane. Inset: close-up SEM of the array; (c) Plasmomechanical coupling: when the MM is illuminated with a pump laser at $\omega_{\rm L}$ corresponding to a wavelength of 1,550 nm, tuned slightly to the red side of the Fano resonance frequency ω_0 , the natural oscillation of the membrane of amplitude δx at its mechanical resonance frequency ($1/\tau_m$) leads to a dynamic modulation of total absorbance (δA). As δA varies between positive and negative values, this leads to a dynamic modulation on the thermal expansion of the membrane. As illustrated here for positive resonance detuning, i.e., $\omega_L < \omega_0$, the light-induced mechanical damping $\Gamma_{\rm pl} \propto \delta A/\delta x$ is always positive, which dampens the mechanical resonance; (d) The thermomechanical Brownian noise spectra for the fundamental mechanical resonance measured at a pump power of \sim 17 μ W for different absorber gap values corresponding to weak (unperturbed), positive (amplification) and negative (cooling) absorption-induced forces. The inset shows the MM absorbance as a function of absorber gap at 1,550 nm pump wavelength near the Fano resonance; (e) Differential spectral absorbance ($dA/d\omega_0$) versus the detuning between the Fano resonance frequency (ω_0) and the fixed 1,550 nm pump laser frequency (ω_L); (f) The effective temperature $T_{\rm eff}$ of the fundamental mechanical mode is proportional to the area under its peak thermomechnical noise spectrum, exemplified in the inset. The absorber gap has been tuned at 5.5 V, corresponding to the maximum $|dA/d\omega_0|$ on the red side of the Fano resonance. At 210 μ W pump power, T_{eff} for the Brownian motion of the mechanical mode is reduced below 50 K from room temperature (T_0 =300 K). Reproduced from Ref. [18] with permission from Springer Nature, copyright 2016

In addition to showing manipulation of mechanical damping by light, the BMMPA demonstrates its utility on electromechanical applications. Electromechanical BMMPAs have been demonstrated operating under sub-terahertz, [172] terahertz [173] and near-infrared spectra. [83] After introducing the BMMPA structure, their modulation speed can be increased by several orders of magnitude, and is thus promising for further applications in tunable spectral filters, switches, modulators and adaptable transformation optics devices, etc. Zheludev *et al.* proposed an approach based on combining the elastic properties of a nanoscale-thickness dielectric membrane with nanoscale electrostatic forces in a planar BMMPA, providing a powerful generic platform for achieving tunable MM characteristics in

the optical spectral range. [83] The colossal electro-optical response of MMs guarantees either fast continuous tuning of its optical properties or high-contrast irreversible switching in a device only 100 nm thick, without external polarizers and analysers. The electrically reconfigurable photonic MM and a schematic of the driving circuit and a section of the MM pattern consisting of a gold nanostructure supported by SiN strings are shown in figure 22(a) and (b). The reversible electro-optical tuning and modulation spectra indicate that the transmittance may be modulated by $^{\sim}5\%$ around 1.1 and 1.3 μm while the reflectance can be modulated by up to 8% around 1.5 μ m [83]. As a MHz bandwidth electrooptical modulator, the mechanical systems can be easily driven to frequencies up to their fundamental resonance. The power consumption is determined numerically to be small (~100 fJ). The material's high-contrast, non-volatile electro-optical switch properties are evaluated by ON an OFF states and the corresponding contrast, as shown in figure 22(c). The transmission, reflection and absorption (T, R and A) of the MM redshift by 20% when the device switches, leading to a dramatic change of 250% in T around 1.2 mm and a change of 110% in R around 1.6 mm, as shown in figure 22(d), (e) and (f), respectively. Therefore, the BMMPA allows fast continuous tuning of its optical properties and highcontrast irreversible switching in a device of only 100 nm thick, without external polarizers and analysers.

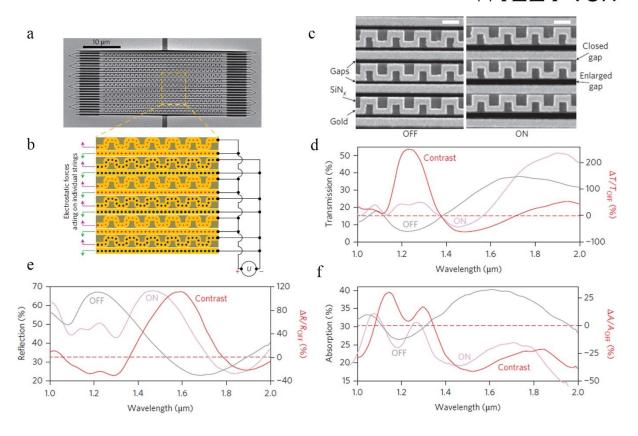


Figure 22. (a) SEM image of the device; (b) Schematic of the driving circuit (black) and a section of the MM pattern consisting of a gold nanostructure (yellow) supported by silicon nitride strings (brown). The driving voltage *U* causes positive (red) and negative (blue) charging and thus electrostatic forces acting in opposite directions (pink and green); (c) SEM images of the MM in its OFF and ON states. Scale bar, 500 nm; Transmission (d), reflection (e) and absorption (f) spectra of the device in the OFF and ON states (left axis) and the corresponding switching contrast (right axis). Reproduced from Ref. [83] with permission from Springer Nature, copyright 2013.

Although it is an easy task to find the solution for electromechanical/thermomechanical manipulation within THz or sub-THz region, devices working in the visible and near-infrared range are challenging because of the required nanoscale fabrication. The electromechanical manipulation provides an opportunity to achieve tunable spectral filters, switches, modulators, protective optical circuitry, optical networks and adaptable transformation optical devices. Thermomechanical coupling facilitates optical manipulation of the dynamics of mechanical oscillators and provides a mean to introduce effective cooling. By using the two mechanisms, further work should be focused on experimental demonstration of these devices.

4. Future outlook and comments

In the past decade, a wide variety of BMMPAs covering wide spectral regimes have been experimentally and theoretically demonstrated due to the significant advances in device fabrication and theoretical modelling. This review summarizes versatile methods with facile design and geometrical scalability, highlighting the ideas behind BMMPAs working at different frequencies, as well as providing guidance on how to optimize design parameters to fulfil diverse application requirements. Most of the BMMPAs are polarization-insensitive due to the symmetric patterns on the top and maintain high absorption over a large range of incidence angle. However, the field of BMMPA research is still at its infancy. Formidable technological challenges remain, as some theoretically demonstrated ideas are too sophisticated to fabricate, limited by the present fabrication technology, e.g. BMMPAs based on 2D materials. These require atomic thickness processing and nanoscale patterning resolution and thus inevitably involve multi-step fabrication and costly FIB or EBL techniques. Furthermore, more effort is required to bridge the gap between the high yield in large fabricated areas and low cost. Solar energy harvesting devices, for instance, are of great significance to address the energy crisis worldwide. BMMPAs provide a great potential to achieve high-efficiency PV devices with theoretical prediction of STPV systems of up to 85% efficiency and ultrathin solar cells. Devices operating from visible to NIR regions of the spectrum need nano-sized resonators in BMMPA designs because the absorption frequencies critically rely on the size of the resonators. However, present fabrication methods of resonators depend mainly on expensive fabrication methods, which are ill-suited for large scale production. Self-assembly and casting-based techniques are promising for fabricating cost-effective PV devices based on BMMPAs. Finally, two "smalls" must be taken into account: to obtain small device sizes at low frequency and to improve small effects at the nanoscale. On the one hand, since the lattice parameter increases for BMMPA operating at lower frequency, narrowing down the size of resonator at low frequency is desired for compact integrated circuits and industrial communication devices. On the other hand, when resonators have nanoscale size, their physical properties are different, such as melting point, oxidation and grain boundary effects, leading to a complicated design.

In addition to the applications reviewed in this paper, we should bear in mind that we can design BMMPAs for other applications as long as we converted the absorbed light into something useful, e.g., into an electrical signal. Overall, although faced with formidable challenges to overcome, the rapidly expanding BMMPA research give us the confidence that their tunable, versatile applications will renew absorption-based devices and they will be adopted by the industry in the near future.

Acknowledgements

This work was supported by National Basic Research Program of China (project 2013CB933301) and National Natural Science Foundation of China (project 51272038). L.V.B. was supported by China Postdoctoral Science Foundation. G.P.W. acknowledges support from the Center for Nanoscale Materials, a U.S. Department of Energy Office of Science User Facility, and support by the U.S. Department of Energy, Office of Science, under Contract No. DE-AC02-06CH11357 One of us (A.O.G.) was supported by the Volkswagen Foundation (Germany) and via the Chang Jiang (Yangtze River) Chair Professorship (China). In addition, the authors acknowledge financial support obtained from the Virtual Institute for Theoretical Photonics and Energy.

Received: ((will be filled in by the editorial staff))
Revised: ((will be filled in by the editorial staff))
Published online: ((will be filled in by the editorial staff))

References

- [1] D. R. Smith, W. J. Padilla, D. Vier, S. C. Nemat-Nasser, S. Schultz, Phys Rev Lett 2000, 84, 4184.
- [2] H. Chen, B.-I. Wu, B. Zhang, J. A. Kong, Physical Review Letters 2007, 99, 063903.
- [3] N. Seddon, T. Bearpark, Science 2003, 302, 1537.
- [4] D. Smith, S. Schultz, P. Markoš, C. Soukoulis, Phys Rev B 2002, 65, 195104.
- [5] N. I. Landy, S. Sajuyigbe, J. Mock, D. Smith, W. Padilla, Phys Rev Lett 2008, 100, 207402.
- [6] J. Hao, J. Wang, X. Liu, W. J. Padilla, L. Zhou, M. Qiu, Appl Phys Lett 2010, 96, 251104.
- [7] C. M. Watts, X. Liu, W. J. Padilla, Adv Mater 2012, 24.
- [8] T. Maier, H. Brückl, Opt Lett 2009, 34, 3012.
- [9] X. Liu, T. Starr, A. F. Starr, W. J. Padilla, Phys Rev Lett 2010, 104, 207403.
- [10] N. Liu, M. Mesch, T. Weiss, M. Hentschel, H. Giessen, Nano letters 2010, 10, 2342.
- [11] M. K. Hedayati, M. Javaherirahim, B. Mozooni, R. Abdelaziz, A. Tavassolizadeh, V. S. K. Chakravadhanula, V. Zaporojtchenko, T. Strunkus, F. Faupel, M. Elbahri, Advanced Materials 2011, 23, 5410.
- [12] C. Wu, B. Neuner Iii, J. John, A. Milder, B. Zollars, S. Savoy, G. Shvets, Journal of Optics 2012, 14, 024005.
- [13] H.-T. Chen, Opt Express 2012, 20, 7165.
- [14] R. Alaee, M. Farhat, C. Rockstuhl, F. Lederer, Optics express 2012, 20, 28017.
- [15] D. Shrekenhamer, W.-C. Chen, W. J. Padilla, Phys Rev Lett 2013, 110, 177403.
- [16] W. Li, U. Guler, N. Kinsey, G. V. Naik, A. Boltasseva, J. Guan, V. M. Shalaev, A. V. Kildishev, Advanced Materials 2014, 26, 7959.
- [17] A. Tittl, A. K. U. Michel, M. Schäferling, X. Yin, B. Gholipour, L. Cui, M. Wuttig, T. Taubner, F. Neubrech, H. Giessen, Adv Mater 2015, 27, 4597; X. Liu, W. J. Padilla, Optica 2017, 4, 430.

- [18] H. Zhu, F. Yi, E. Cubukcu, Nature Photonics 2016.
- [19] C. Kurter, J. Abrahams, S. M. Anlage, Applied Physics Letters 2010, 96, 253504; B. Edwards, A. Alù, M. E. Young, M. Silveirinha, N. Engheta, Physical review letters 2008, 100, 033903; G. Scalari, C. Maissen, D. Turčinková, D. Hagenmüller, S. De Liberato, C. Ciuti, C. Reichl, D. Schuh, W. Wegscheider, M. Beck, Science 2012, 335, 1323; I. Zolotovskii, D. Korobko, R. Minvaliev, V. Ostatochnikov, Opt Spectrosc+ 2014, 117, 822; I. Sersic, M. Frimmer, E. Verhagen, A. F. Koenderink, Phys Rev Lett 2009, 103, 213902; A. Christ, O. J. Martin, Y. Ekinci, N. A. Gippius, S. G. Tikhodeev, Nano Letters 2008, 8, 2171.
- [20] A. G. Paulish, P. S. Zagubisalo, S. A. Kuznetsov, "High-performance metamaterial MM-to-IR Converter for MM-wave imaging", presented at *Infrared, Millimeter, and Terahertz Waves (IRMMW-THz), 2013 38th International Conference on, 2013.*
- [21] Z. H. Jiang, S. Yun, F. Toor, D. H. Werner, T. S. Mayer, ACS nano 2011, 5, 4641.
- [22] P. Yu, J. Wu, E. Ashalley, A. Govorov, Z. Wang, Journal of Physics D: Applied Physics 2016, 49, 365101.
- [23] L. Luo, I. Chatzakis, J. Wang, F. B. Niesler, M. Wegener, T. Koschny, C. M. Soukoulis, Nature communications 2014, 5.
- [24] K. Aydin, V. E. Ferry, R. M. Briggs, H. A. Atwater, Nature communications 2011, 2, 517.
- [25] B. Reinhard, K. M. Schmitt, V. Wollrab, J. Neu, R. Beigang, M. Rahm, Appl Phys Lett 2012, 100, 221101.
- [26] Z. Yong, S. Zhang, C. Gong, S. He, Scientific reports 2016, 6.
- [27] X. Liu, T. Tyler, T. Starr, A. F. Starr, N. M. Jokerst, W. J. Padilla, Phys Rev Lett 2011, 107,
- 045901; P. Bermel, M. Ghebrebrhan, M. Harradon, Y. X. Yeng, I. Celanovic, J. D. Joannopoulos, M. Soljacic, Nanoscale research letters 2011, 6, 1.
- [28] D. Shrekenhamer, W. Xu, S. Venkatesh, D. Schurig, S. Sonkusale, W. J. Padilla, Phys Rev Lett 2012, 109, 177401.
- [29] K. Chen, R. Adato, H. Altug, Acs Nano 2012, 6, 7998.
- [30] K.-T. Lin, H.-L. Chen, Y.-S. Lai, C.-C. Yu, Nature communications 2014, 5.
- [31] B. Casse, W. Lu, Y. Huang, E. Gultepe, L. Menon, S. Sridhar, Appl Phys Lett 2010, 96, 023114.
- [32] M. Gil, J. Bonache, F. Martin, Metamaterials 2008, 2, 186.
- [33] M. D. Astorino, F. Frezza, N. Tedeschi, "Narrow-band and dual-band metamaterial absorbers in the THz regime", presented at *Electromagnetic Theory (EMTS)*, 2016 URSI International Symposium on, 2016.
- [34] Y. Lee, P. Tuong, H. Zheng, J. Rhee, W. Jang, Journal of the Korean Physical Society 2012, 60, 1203.
- [35] P. Pitchappa, C. P. Ho, P. Kropelnicki, N. Singh, D.-L. Kwong, C. Lee, J Appl Phys 2014, 115, 193109.
- [36] Y. J. Yoo, Y. J. Kim, P. Van Tuong, J. Y. Rhee, K. W. Kim, W. H. Jang, Y. Kim, H. Cheong, Y. Lee, Opt Express 2013, 21, 32484.
- [37] S. Bhattacharyya, S. Ghosh, K. Vaibhav Srivastava, Journal of Applied Physics 2013, 114, 094514.
- [38] L. Huang, H. Chen, Progress In Electromagnetics Research 2011, 113, 103.
- [39] G. Dayal, S. A. Ramakrishna, Journal of Optics 2013, 15, 055106.
- [40] Y. Q. Ye, Y. Jin, S. He, JOSA B 2010, 27, 498.
- [41] J. Rhee, Y. Yoo, K. Kim, Y. Kim, Y. Lee, J Electromagnet Wave 2014, 28, 1541.
- [42] M. K. Hedayati, F. Faupel, M. Elbahri, Materials 2014, 7, 1221; S. Ogawa, M. Kimata, Materials 2018, 11, 458; L. Huang, H. T. Chen, *A brief review on terahertz metamaterial perfect absorbers*, Vol. 6, 2013.
- [43] X. Zhao, K. Song, AIP Advances 2014, 4, 100701.
- [44] Y. Wu, J. Li, Z.-Q. Zhang, C. Chan, Phys Rev B 2006, 74, 085111; B. A. Slovick, Z. G. Yu, S. Krishnamurthy, Phys Rev B 2014, 89, 155118.
- [45] J. Zhou, L. Zhang, G. Tuttle, T. Koschny, C. M. Soukoulis, Physical Review B 2006, 73, 041101.
- [46] G. Duan, J. Schalch, X. Zhao, J. Zhang, R. D. Averitt, X. Zhang, Phys Rev B 2018, 97, 035128.

- [47] A. Rasoul, A. Mohammad, R. Carsten, Journal of Physics D: Applied Physics 2017, 50, 503002.
- [48] P. Rufangura, C. Sabah, Vacuum 2015, 120, 68; B. Mulla, C. Sabah, Waves in Random and Complex Media 2015, 25, 382.
- [49] H. Li, L. H. Yuan, B. Zhou, X. P. Shen, Q. Cheng, T. J. Cui, J Appl Phys 2011, 110, 014909.
- [50] S. Gu, J. Barrett, T. Hand, B.-I. Popa, S. Cummer, J Appl Phys 2010, 108, 064913.
- [51] M. Navarro-Cía, M. Beruete, I. Campillo, M. Sorolla, Phys Rev B 2011, 83, 115112.
- [52] H.-T. Hsu, C.-J. Wu, Progress In Electromagnetics Research Letters 2009, 9, 101.
- [53] Y. Huang, Y. Tian, G. Wen, W. Zhu, Journal of Optics 2013, 15, 055104; Y.-J. Huang, G.-J.
- Wen, J. Li, W.-R. Zhu, P. Wang, Y.-H. Sun, J Electromagnet Wave 2013, 27, 552.
- [54] S. Gu, B. Su, X. Zhao, Journal of Applied Physics 2013, 114, 163702.
- [55] B. S. L. C.-R. Zhang, Y.-P. Z. Xiao-Peng, Acta Physica Sinica 2010, 5, 042.
- [56] P. Tuong, J. Park, J. Rhee, K. Kim, H. Cheong, W. Jang, Y. Lee, Materials Chemistry and Physics 2013, 141, 535.
- [57] W. Zhu, X. Zhao, B. Gong, L. Liu, B. Su, Applied Physics A: Materials Science & Processing 2011, 102, 147.
- [58] W. Ma, Y. Wen, X. Yu, Opt Express 2013, 21, 30724.
- [59] L. Huang, D. R. Chowdhury, S. Ramani, M. T. Reiten, S.-N. Luo, A. J. Taylor, H.-T. Chen, Opt. Lett. 2012, 37, 154.
- [60] Y. Cheng, Y. Nie, R. Gong, Optics & Laser Technology 2013, 48, 415.
- [61] M. Soheilifar, R. Sadeghzadeh, AEU-International Journal of Electronics and Communications 2015, 69, 126.
- [62] M. Choi, S. H. Lee, Y. Kim, S. B. Kang, J. Shin, M. H. Kwak, K.-Y. Kang, Y.-H. Lee, N. Park, B. Min, Nature 2011, 470, 369.
- [63] H. Wang, L. Wang, Optics express 2013, 21, A1078.
- [64] H. Wang, V. P. Sivan, A. Mitchell, G. Rosengarten, P. Phelan, L. Wang, Solar Energy Materials and Solar Cells 2015, 137, 235.
- [65] J. A. Bossard, L. Lin, S. Yun, L. Liu, D. H. Werner, T. S. Mayer, ACS nano 2014, 8, 1517.
- [66] J. Zhu, Z. Ma, W. Sun, F. Ding, Q. He, L. Zhou, Y. Ma, Applied Physics Letters 2014, 105, 021102.
- [67] D. Hu, H. Wang, Z. Tang, X. Zhang, Appl Optics 2016, 55, 5257.
- [68] S. Molesky, C. J. Dewalt, Z. Jacob, Opt Express 2013, 21, A96.
- [69] C. Zhang, Q. Cheng, J. Yang, J. Zhao, T. J. Cui, Applied Physics Letters 2017, 110, 143511.
- [70] G. Deng, J. Yang, Z. Yin, Appl Optics 2017, 56, 2449.
- [71] Y. Zhang, Y. Li, Y. Cao, Y. Liu, H. Zhang, Optics Communications 2017, 382, 281.
- [72] B. Vasić, R. Gajić, Applied Physics Letters 2013, 103, 261111.
- [73] Z. Su, J. Yin, X. Zhao, Optics express 2015, 23, 1679.
- [74] S. He, T. Chen, IEEE transactions on terahertz science and technology 2013, 3, 757.
- [75] J. Wang, Y. Jiang, Opt Express 2017, 25, 5206.
- [76] M. K. Hedayati, F. Faupel, M. Elbahri, Applied Physics A 2012, 109, 769.
- [77] K. Chaudhuri, M. Alhabeb, Z. Wang, V. M. Shalaev, Y. Gogotsi, A. Boltasseva, ACS Photonics 2018, 5, 1115.
- [78] Y. Cui, K. H. Fung, J. Xu, H. Ma, Y. Jin, S. He, N. X. Fang, Nano letters 2012, 12, 1443.
- [79] Y. Bai, L. Zhao, D. Ju, Y. Jiang, L. Liu, Optics express 2015, 23, 8670.
- [80] R. Feng, J. Qiu, L. Liu, W. Ding, L. Chen, Optics express 2014, 22, A1713.
- [81] B. Zhang, Y. Zhang, J. Duan, W. Zhang, W. Wang, Sensors 2016, 16, 1153.
- [82] G.-H. Yang, X.-X. Liu, Y.-L. Lv, J.-H. Fu, Q. Wu, X. Gu, Journal of Applied Physics 2014, 115, 17E523.
- [83] J.-Y. Ou, E. Plum, J. Zhang, N. I. Zheludev, Nature nanotechnology 2013, 8, 252.
- [84] F. Dincer, O. Akgol, M. Karaaslan, E. Unal, C. Sabah, Progress In Electromagnetics Research 2014, 144, 93.
- [85] Y. Pang, J. Wang, Q. Cheng, S. Xia, X. Y. Zhou, Z. Xu, T. J. Cui, S. Qu, Applied Physics Letters 2017, 110, 104103.
- [86] H. Xiong, J.-S. Hong, C.-M. Luo, L.-L. Zhong, Journal of Applied Physics 2013, 114, 064109.
- [87] Y. Liu, S. Gu, C. Luo, X. Zhao, Applied Physics A 2012, 108, 19.

- [88] X. Zhao, K. Fan, J. Zhang, H. R. Seren, G. D. Metcalfe, M. Wraback, R. D. Averitt, X. Zhang, Sensors and Actuators A: Physical 2015, 231, 74.
- [89] J. Grant, Y. Ma, S. Saha, A. Khalid, D. R. Cumming, Opt. Lett. 2011, 36, 3476.
- [90] Y. Z. Cheng, W. Withayachumnankul, A. Upadhyay, D. Headland, Y. Nie, R. Z. Gong, M. Bhaskaran, S. Sriram, D. Abbott, Applied Physics Letters 2014, 105, 181111.
- [91] C. Wu, G. Shvets, Opt. Lett. 2012, 37, 308.
- [92] C. Hu, L. Liu, Z. Zhao, X. n. Chen, X. Luo, Optics express 2009, 17, 16745.
- [93] R. R. Nair, P. Blake, A. N. Grigorenko, K. S. Novoselov, T. J. Booth, T. Stauber, N. M. Peres, A. K. Geim, Science 2008, 320, 1308.
- [94] S. H. Lee, M. Choi, T.-T. Kim, S. Lee, M. Liu, X. Yin, H. K. Choi, S. S. Lee, C.-G. Choi, S.-Y. Choi, Nature materials 2012, 11, 936.
- [95] D.-e. Wen, H. Yang, Q. Ye, M. Li, L. Guo, J. Zhang, Physica Scripta 2013, 88, 015402.
- [96] Q. Liang, T. Wang, Z. Lu, Q. Sun, Y. Fu, W. Yu, Advanced Optical Materials 2013, 1, 43.
- [97] J. Sun, L. Liu, G. Dong, J. Zhou, Optics Express 2011, 19, 21155; J. Yang, X. Hu, X. Li, Z.
- Liu, Z. Liang, X. Jiang, J. Zi, Physical Review B 2009, 80, 125103; H.-T. Chen, J. Zhou, J. F. O'Hara, F. Chen, A. K. Azad, A. J. Taylor, Physical review letters 2010, 105, 073901.
- [98] F. Ding, Y. Cui, X. Ge, Y. Jin, S. He, Applied Physics Letters 2012, 100, 103506.
- [99] B.-X. Wang, L.-L. Wang, G.-Z. Wang, W.-Q. Huang, X.-F. Li, X. Zhai, IEEE Photonics Technology Letters 2014, 26, 111.
- [100] S. Agarwal, Y. Prajapati, Applied Physics A 2016, 122, 561.
- [101] M. Amin, M. Farhat, H. Bağcı, Optics express 2013, 21, 29938.
- [102] X. Jia, X. Wang, C. Yuan, Q. Meng, Z. Zhou, Journal of Applied Physics 2016, 120, 033101.
- [103] X. Zhu, W. Yan, P. Uhd Jepsen, O. Hansen, N. Asger Mortensen, S. Xiao, Applied Physics Letters 2013, 102, 131101.
- [104] G. Konstantatos, M. Badioli, L. Gaudreau, J. Osmond, M. Bernechea, F. P. G. De Arquer, F. Gatti, F. H. Koppens, Nature nanotechnology 2012, 7, 363.
- [105] Y. Zhi Cheng, Y. Wang, Y. Nie, R. Zhou Gong, X. Xiong, X. Wang, Journal of Applied Physics 2012, 111, 044902.
- [106] S. Li, J. Gao, X. Cao, W. Li, Z. Zhang, D. Zhang, Journal of Applied Physics 2014, 116, 043710.
- [107] J. Chen, X. Huang, G. Zerihun, Z. Hu, S. Wang, G. Wang, X. Hu, M. Liu, Journal of Electronic Materials 2015, 44, 4269.
- [108] Y. Shi, Y. C. Li, T. Hao, L. Li, C.-H. Liang, Waves in Random and Complex Media 2017, 27, 381.
- [109] G. Chao, Q. Shao-Bo, P. Zhi-Bin, Z. Hang, X. Zhuo, B. Peng, P. Wei-Dong, L. Bao-Qin, Chinese Physics Letters 2010, 27, 117802; X. Kong, J. Xu, J.-j. Mo, S. Liu, Frontiers of Optoelectronics 2017, 10, 124.
- [110] D. Lee, H. Jeong, S. Lim, Scientific Reports 2017, 7, 4891.
- [111] J. Wu, P. Yu, A. S. Susha, K. A. Sablon, H. Chen, Z. Zhou, H. Li, H. Ji, X. Niu, A. O. Govorov, A. L. Rogach, Z. M. Wang, Nano Energy 2015, 13, 827.
- [112] P. Yu, Y. Yao, J. Wu, X. Niu, A. L. Rogach, Z. Wang, Scientific Reports 2017, 7, 7696.
- [113] M. Hedayati, A. Zillohu, T. Strunskus, F. Faupel, M. Elbahri, Applied Physics Letters 2014, 104, 041103.
- [114] A. Biswas, H. Eilers, F. Hidden Jr, O. Aktas, C. Kiran, Applied physics letters 2006, 88, 013103.
- [115] N. F. Hadley, Science 1979, 203, 367.
- [116] K. Tanaka, Y. Fujiyama, R. Tomokane, H. Koga, S. Akita, T. Nosaka, Y. Nakayama, M. Tonouchi, "Wave absorbing properties of polymer-carbon nanocomposites in the THz region", presented at *Infrared and Millimeter Waves*, 2007 and the 2007 15th International Conference on Terahertz Electronics. IRMMW-THz. Joint 32nd International Conference on, 2007.
- [117] A. Saib, L. Bednarz, R. Daussin, C. Bailly, X. Lou, J.-M. Thomassin, C. Pagnoulle, C. Detrembleur, R. Jérôme, I. Huynen, IEEE T Microw Theory 2006, 54, 2745.
- [118] W. Zhu, Y. Huang, I. D. Rukhlenko, G. Wen, M. Premaratne, Opt Express 2012, 20, 6616.
- [119] Y. Yong-Jun, H. Yong-Jun, W. Guang-Jun, Z. Jing-Ping, S. Hai-Bin, O. Gordon, Chinese Physics B 2012, 21, 038501.

- [120] L. Liu, H. Peng, Y. Pu, X. Ying, Z. Li, J. Xu, Y. Jiang, Z. Liu, Opt. Express 2018, 26, 1064; S. Butun, K. Aydin, Opt. Express 2014, 22, 19457.
- [121] F. Ding, J. Dai, Y. Chen, J. Zhu, Y. Jin, S. I. Bozhevolnyi, Scientific reports 2016, 6, 39445.
- [122] J. R. Hendrickson, S. Vangala, C. Dass, R. Gibson, J. Goldsmith, K. Leedy, D. E. Walker, J. W. Cleary, W. Kim, J. Guo, ACS Photonics 2018, 5, 776.
- [123] A. Noor, Z. Hu, Journal of Infrared, Millimeter, and Terahertz Waves 2010, 31, 791.
- [124] M. Decker, I. Staude, I. I. Shishkin, K. B. Samusev, P. Parkinson, V. K. Sreenivasan, A. Minovich, A. E. Miroshnichenko, A. Zvyagin, C. Jagadish, Nature communications 2013, 4, 2949.
- [125] K. Bi, G. Dong, X. Fu, J. Zhou, Applied Physics Letters 2013, 103, 131915; F. J. Rachford, D. N. Armstead, V. G. Harris, C. Vittoria, Physical review letters 2007, 99, 057202.
- [126] Y. Huang, G. Wen, W. Zhu, J. Li, L.-M. Si, M. Premaratne, Opt Express 2014, 22, 16408.
- [127] C. Hägglund, S. P. Apell, The journal of physical chemistry letters 2012, 3, 1275; J. N. Munday, H. A. Atwater, Nano letters 2010, 11, 2195.
- [128] A. Rothschild, E. Sharlin, G. Ankonina, H. Dotan, I. Dumchin, M. Gross, O. Kfir, O. Blank, Nature Materials 2013, 12, 158.
- [129] N.-P. Harder, P. Würfel, Semiconductor Science and Technology 2003, 18, S151.
- [130] S. J. Kim, P. Fan, J.-H. Kang, M. L. Brongersma, Nature communications 2015, 6.
- [131] J. Chen, X. Huang, G. Zerihun, Z. Hu, S. Wang, G. Wang, X. Hu, M. Liu, Journal of Electronic Materials 2015, 44, 4269.
- [132] V. Aroutiounian, S. Petrosyan, A. Khachatryan, K. Touryan, Journal of Applied Physics 2001, 89, 2268; P. Yu, J. Wu, L. Gao, H. Liu, Z. Wang, Sol Energ Mat Sol C 2017, 161, 377.
- [133] Y. Peng, W. Jiang, A. Eric, G. Alexander, W. Zhiming, Journal of Physics D: Applied Physics 2016, 49, 365101.
- [134] P. Yu, Y. Yao, J. Wu, X. Niu, A. L. Rogach, Z. Wang, Scientific Reports 2017, 7; E. Garnett, P. Yang, Nano letters 2010, 10, 1082.
- [135] V. Rinnerbauer, A. Lenert, D. M. Bierman, Y. X. Yeng, W. R. Chan, R. D. Geil, J. J. Senkevich, J. D. Joannopoulos, E. N. Wang, M. Soljačić, Advanced Energy Materials 2014, 4.
- [136] J. B. Chou, Y. X. Yeng, Y. E. Lee, A. Lenert, V. Rinnerbauer, I. Celanovic, M. Soljačić, N. X. Fang, E. N. Wang, S. G. Kim, Advanced Materials 2014, 26, 8041.
- [137] E. Rephaeli, S. Fan, Opt Express 2009, 17, 15145.
- [138] Q. Jiang, S. Zhang, M. Zhao, Mater Chem Phys 2003, 82, 225.
- [139] V. Andreev, A. Vlasov, V. Khvostikov, O. Khvostikova, P. Gazaryan, S. Sorokina, N. Sadchikov, Journal of Solar Energy Engineering 2007, 129, 298; C. Ungaro, S. K. Gray, M. C. Gupta, Optics express 2015, 23, A1149; Y. Huang, L. Liu, M. Pu, X. Li, X. Ma, X. Luo, Nanoscale 2018, 10, 8298.
- [140] J. H. Park, S. E. Han, P. Nagpal, D. J. Norris, ACS Photonics 2016, 3, 494.
- [141] A. Kohiyama, M. Shimizu, H. Yugami, Applied Physics Express 2016, 9, 112302.
- [142] Y. Nam, A. Lenert, Y. X. Yeng, P. Bermel, M. Soljačić, E. N. Wang, "Solar thermophotovoltaic energy conversion systems with tantalum photonic crystal absorbers and emitters", presented at *Solid-State Sensors, Actuators and Microsystems (TRANSDUCERS & EUROSENSORS XXVII), 2013 Transducers & Eurosensors XXVII: The 17th International Conference on, 2013*; A. Lenert, D. M. Bierman, Y. Nam, W. R. Chan, I. Celanović, M. Soljačić, E. N. Wang, Nature nanotechnology 2014. 9, 126.
- [143] A. Vora, J. Gwamuri, N. Pala, A. Kulkarni, J. M. Pearce, D. Ö. Güney, Scientific reports 2014, 4.
- [144] D. Ö. Güney, T. Koschny, C. M. Soukoulis, Physical Review B 2009, 80, 125129.
- [145] H. Deng, T. Wang, J. Gao, X. Yang, Journal of Optics 2014, 16, 035102.
- [146] E. W. McFarland, J. Tang, Nature 2003, 421, 616.
- [147] J. Li, S. K. Cushing, P. Zheng, F. Meng, D. Chu, N. Wu, Nature communications 2013, 4, 2651.
- [148] W. Li, J. Valentine, Nano letters 2014, 14, 3510.
- [149] S. Song, Q. Chen, L. Jin, F. Sun, Nanoscale 2013, 5, 9615; W. Li, Z. J. Coppens, L. V.
- Besteiro, W. Wang, A. O. Govorov, J. Valentine, Nature Communications 2015, 6, 8379.
- [150] M. W. Knight, H. Sobhani, P. Nordlander, N. J. Halas, Science 2011, 332, 702.

- [151] H. Harutyunyan, A. B. Martinson, D. Rosenmann, L. K. Khorashad, L. V. Besteiro, A. O. Govorov, G. P. Wiederrecht, Nature nanotechnology 2015, 10, 770.
- [152] M. E. Sykes, J. W. Stewart, G. M. Akselrod, X.-T. Kong, Z. Wang, D. J. Gosztola, A. B. Martinson, D. Rosenmann, M. H. Mikkelsen, A. O. Govorov, Nature Communications 2017, 8, 986.
 [153] Y. Yu, Z. Ji, S. Zu, B. Du, Y. Kang, Z. Li, Z. Zhou, K. Shi, Z. Fang, Adv Funct Mater 2016, 26, 6394.
- [154] A. Sousa-Castillo, M. Comesaña-Hermo, B. Rodríguez-González, M. s. Pérez-Lorenzo, Z. Wang, X.-T. Kong, A. O. Govorov, M. A. Correa-Duarte, The Journal of Physical Chemistry C 2016, 120, 11690.
- [155] A. O. Govorov, H. Zhang, Y. K. Gun'ko, The Journal of Physical Chemistry C 2013, 117, 16616; L. V. Besteiro, A. O. Govorov, The Journal of Physical Chemistry C 2016, 120, 19329.
- [156] G. V. Hartland, L. V. Besteiro, P. Johns, A. O. Govorov, ACS Energy Letters 2017, 2, 1641.
- [157] X. T. Kong, Z. Wang, A. O. Govorov, Advanced Optical Materials 2017, 5.
- [158] L. V. Besteiro, X.-T. Kong, Z. Wang, G. Hartland, A. O. Govorov, ACS Photonics 2017, 4, 2759.
- [159] Y. Lu, W. Dong, Z. Chen, A. Pors, Z. Wang, S. I. Bozhevolnyi, Scientific reports 2016, 6, 30650.
- [160] B. Y. Zheng, Y. Wang, P. Nordlander, N. J. Halas, Adv Mater 2014, 26, 6318; F. P. García de Arquer, A. Mihi, G. Konstantatos, ACS photonics 2015, 2, 950.
- [161] Z. Fang, Z. Liu, Y. Wang, P. M. Ajayan, P. Nordlander, N. J. Halas, Nano letters 2012, 12, 3808; W. Wang, A. Klots, D. Prasai, Y. Yang, K. I. Bolotin, J. Valentine, Nano letters 2015, 15, 7440; J. Fang, D. Wang, C. T. DeVault, T.-F. Chung, Y. P. Chen, A. Boltasseva, V. M. Shalaev, A. V. Kildishev, Nano Letters 2017, 17, 57.
- [162] L. Wen, Y. Chen, L. Liang, Q. Chen, ACS Photonics 2017.
- [163] J. Saavedra, A. Asenjo-Garcia, F. J. García de Abajo, ACS Photonics 2016, 3, 1637.
- [164] M. W. Knight, Y. Wang, A. S. Urban, A. Sobhani, B. Y. Zheng, P. Nordlander, N. J. Halas, Nano letters 2013, 13, 1687.
- [165] K. Du, Q. Li, W. Zhang, Y. Yang, M. Qiu, IEEE Photonics Journal 2015, 7, 1.
- [166] J. Grant, I. Escorcia Carranza, C. Li, I. J. McCrindle, J. Gough, D. R. Cumming, Laser & Photonics Reviews 2013, 7, 1043.
- [167] W. Ma, D. Jia, Y. Wen, X. Yu, Y. Feng, Y. Zhao, Opt Lett 2016, 41, 2974.
- [168] S. Cibella, P. Carelli, M. Castellano, F. Chiarelloa, A. Gaggeroa, E. Giovinea, G. Scalaric, G. Torriolia, R. Leonia, "A metamaterial-coupled hot-electron-bolometer working at THz frequencies", presented at *Proc. of SPIE Vol.*, 2017.
- [169] F. B. Niesler, J. K. Gansel, S. Fischbach, M. Wegener, Appl Phys Lett 2012, 100, 203508.
- [170] F. Zhang, S. Feng, K. Qiu, Z. Liu, Y. Fan, W. Zhang, Q. Zhao, J. Zhou, Appl Phys Lett 2015, 106, 091907.
- [171] N. J. Hogan, A. S. Urban, C. Ayala-Orozco, A. Pimpinelli, P. Nordlander, N. J. Halas, Nano letters 2014, 14, 4640.
- [172] D. Chicherin, S. Dudorov, D. Lioubtchenko, V. Ovchinnikov, S. Tretyakov, A. V. Räisänen, Microw Opt Techn Let 2006, 48, 2570.
- [173] W. Zhu, A. Liu, T. Bourouina, D. Tsai, J. Teng, X. Zhang, G. Lo, D. Kwong, N. Zheludev, Nature communications 2012, 3, 1274.

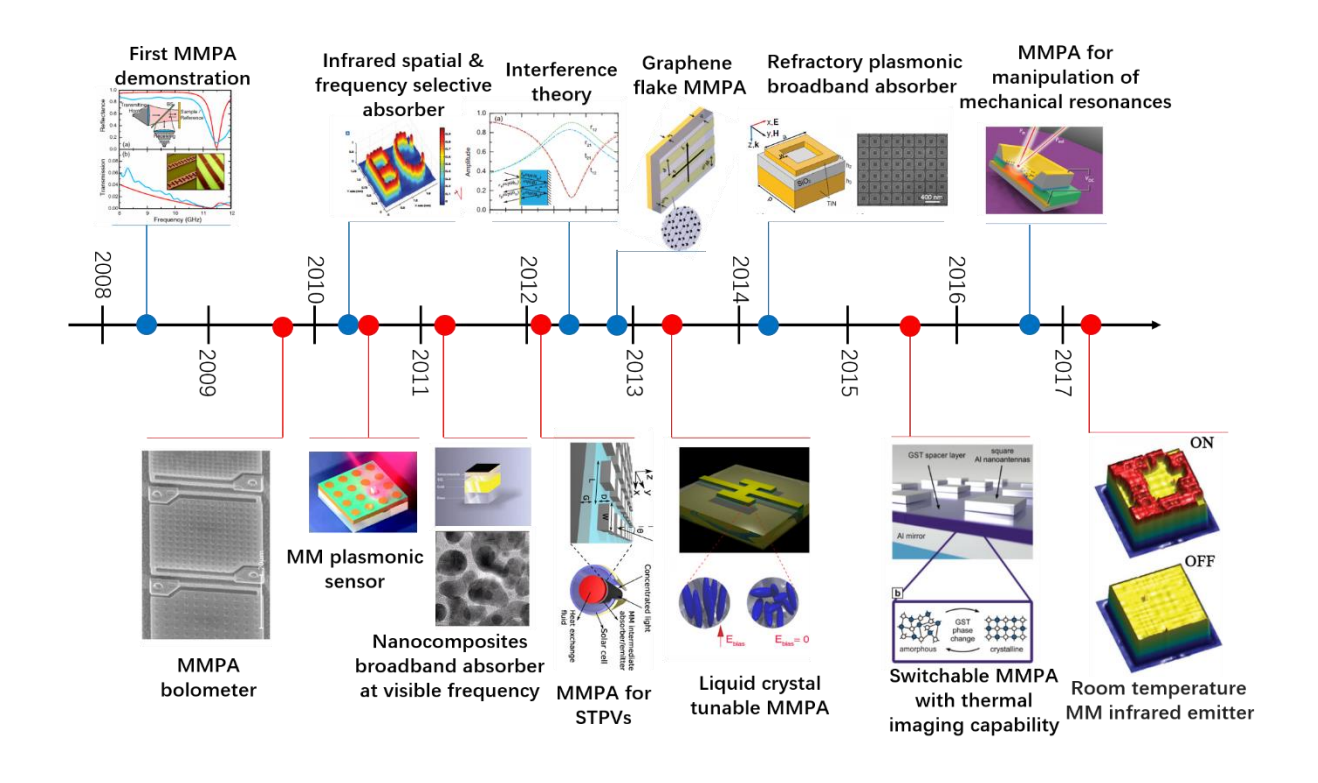


Figure 1. Selected representative publications on MMPA from 2008 to the middle of 2017. The publications are from Ref. ^[5, 8-17, 18], respectively along the time axis.

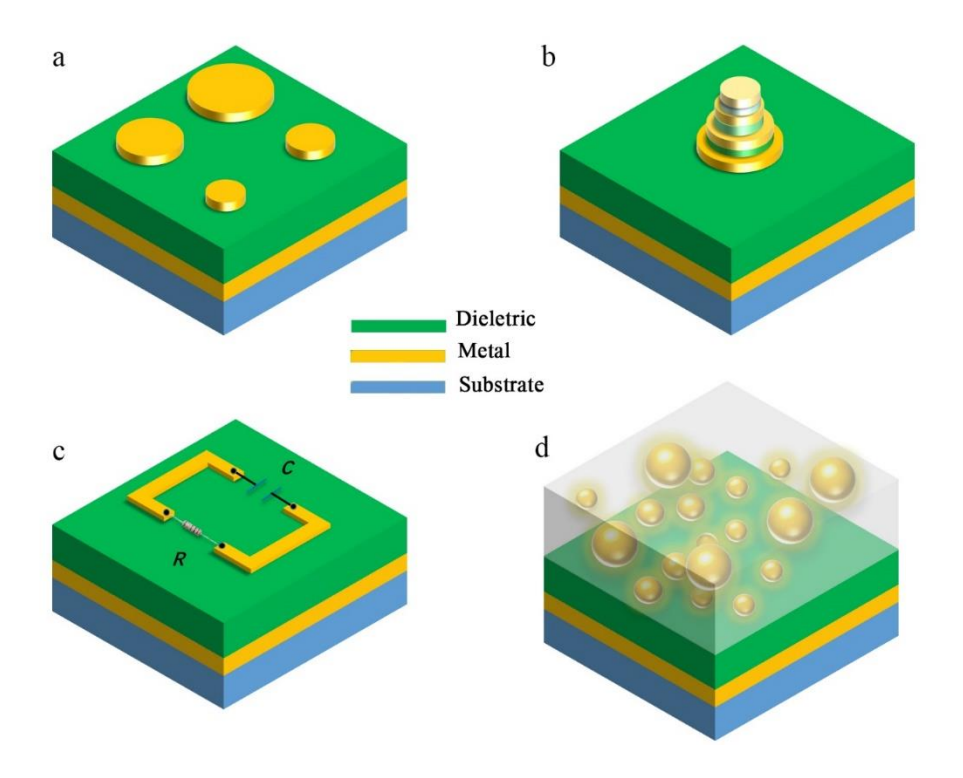


Figure 2. Conventional designs for BMMPAs. (a) Planar arrangement; (b) Vertical arrangement; (c) Welded with lumped elements; (d) Nanocomposites.

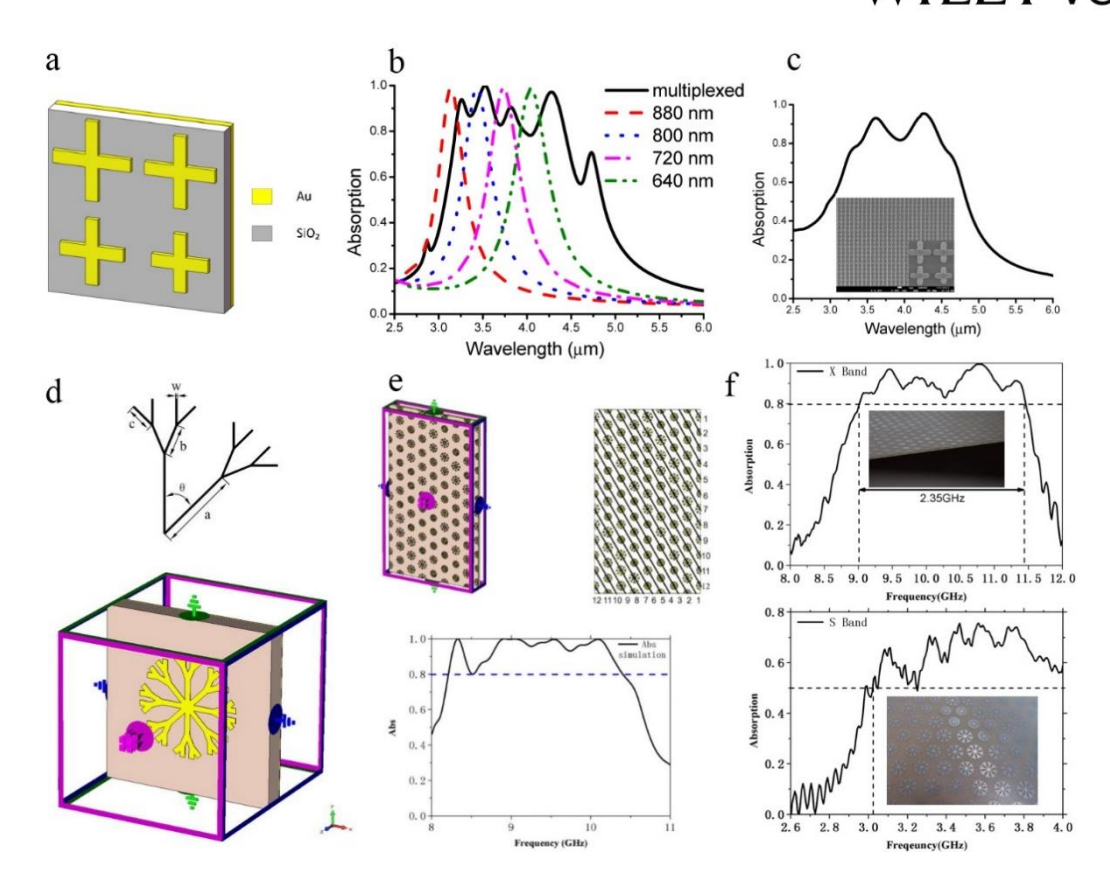


Figure 3. (a) Unit cell schematic diagram of four cross resonators. The gold layer is 100 nm thick for the ground plane and 60 nm for the metallic patterns. The SiO₂ dielectric layer is 190 nm; (b) Simulated absorption of multiplexed and four traditional non-multiplexed absorbers; (c) Measured absorption for multiplexed absorber. The inset is a SEM image of the multiplexed absorber. (d) Three-level dendritic structure and dendritic unit cell in the simulation model; (e) The schematic of the X-band absorber composed of twelve kinds of independent units and its simulation result; (f) The experimental results of the X-band and S-band absorbers. **a-c**: Reproduced from Ref. ^[58] with permission from Optical Society of America, copyright 2013. **d-f**: Reproduced from Ref. ^[54] with permission from AIP Publishing, copyright 2013.

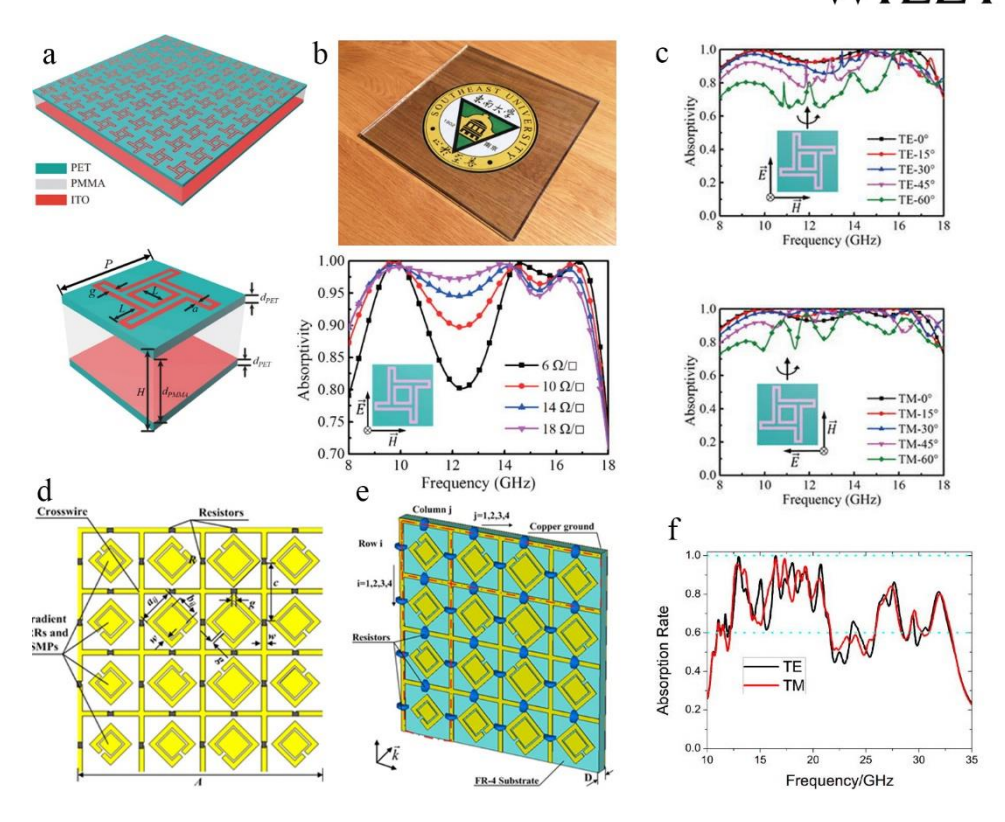


Figure 4. (a) Schematics of an optically transparent BMMPA; (b) Photograph of the fabricated sample and simulated absorptivity spectra with the increase of surface resistance of the ITO layer at normal incidence of TE wave, with the polarization direction illustrated in the inset; (c) The angular dependence of the simulated absorptivity spectra for the MMA under the incidence of TE and TM waves, with the polarization direction and the incidence angle θ illustrated in the insets. The structure of the unit cell of a proposed integrated BMMPA, where (d) is the plan view and (e) is the stereogram; (f) The calculated absorption rate for both TE and TM wave. **a-c**: Reproduced from Ref. ^[69] with permission from AIP Publishing, copyright 2017. **d-f**: Reproduced from Ref. ^[82] with permission from AIP Publishing, copyright 2014.

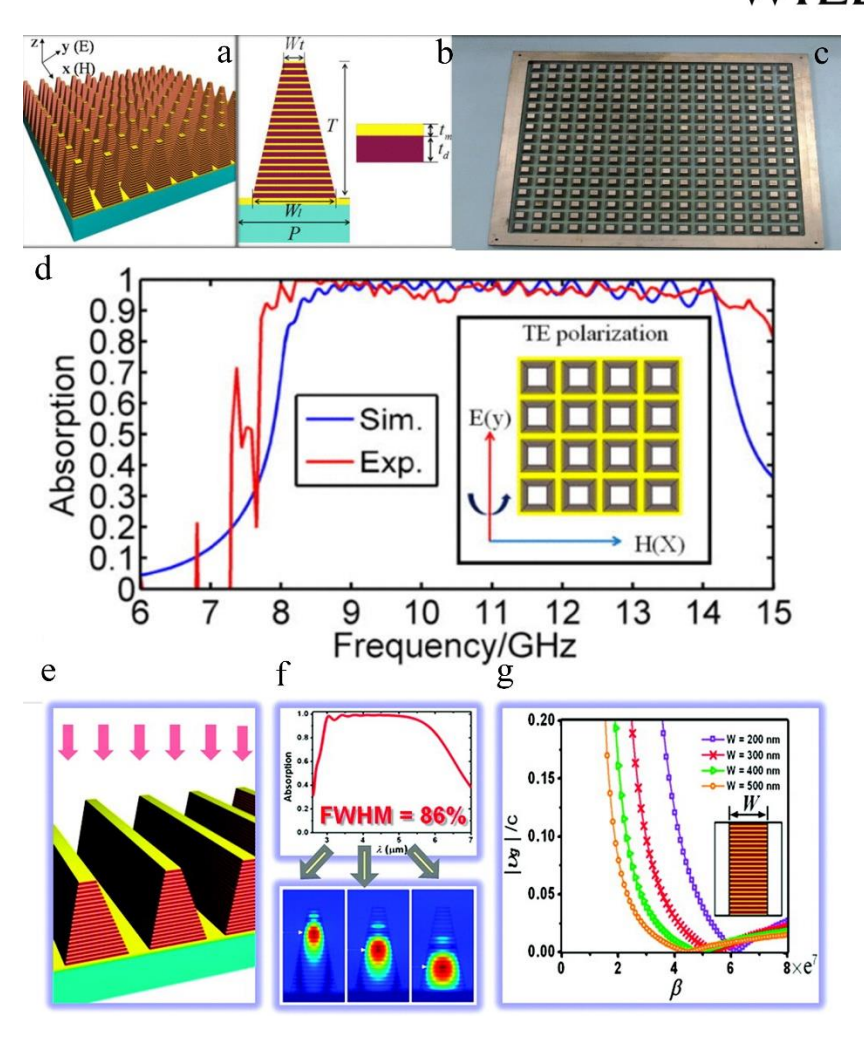


Figure 5. (a) Three-dimensional illustration of the simulated MMPA; (b) schematic of a MMPA unit cell, and (c) photograph of the fabricated sample. The optimized dimensions of a unit are $W_t = 5$ mm, $W_t = 9$ mm, P = 11 mm, $t_m = 0.05$ mm, $t_d = 0.2$ mm, and T = 5 mm. Subscript "m" represents copper, and "d" for FR4; (d) Comparison between the simulated absorption (blue line) and experimental absorption (red line). The inset shows the configuration of the incident wave. (e) Diagram of the sawtooth anisotropic MM thin film absorber. Light of TM polarization is incident along z direction; (f) Absorption spectra for the sawtooth MMPA and distributions of magnetic field corresponding to 3.5, 4.5, and 5.5 μm, respectively; (g) Relationship between the group velocity and propagation constant (proportional to wavevector) at different W. **a-d**: Reproduced from Ref. [98] with permission from AIP publishing, copyright 2012. **e-g**: Reproduced from Ref. [78] with permission from American Chemical Society, copyright 2012.

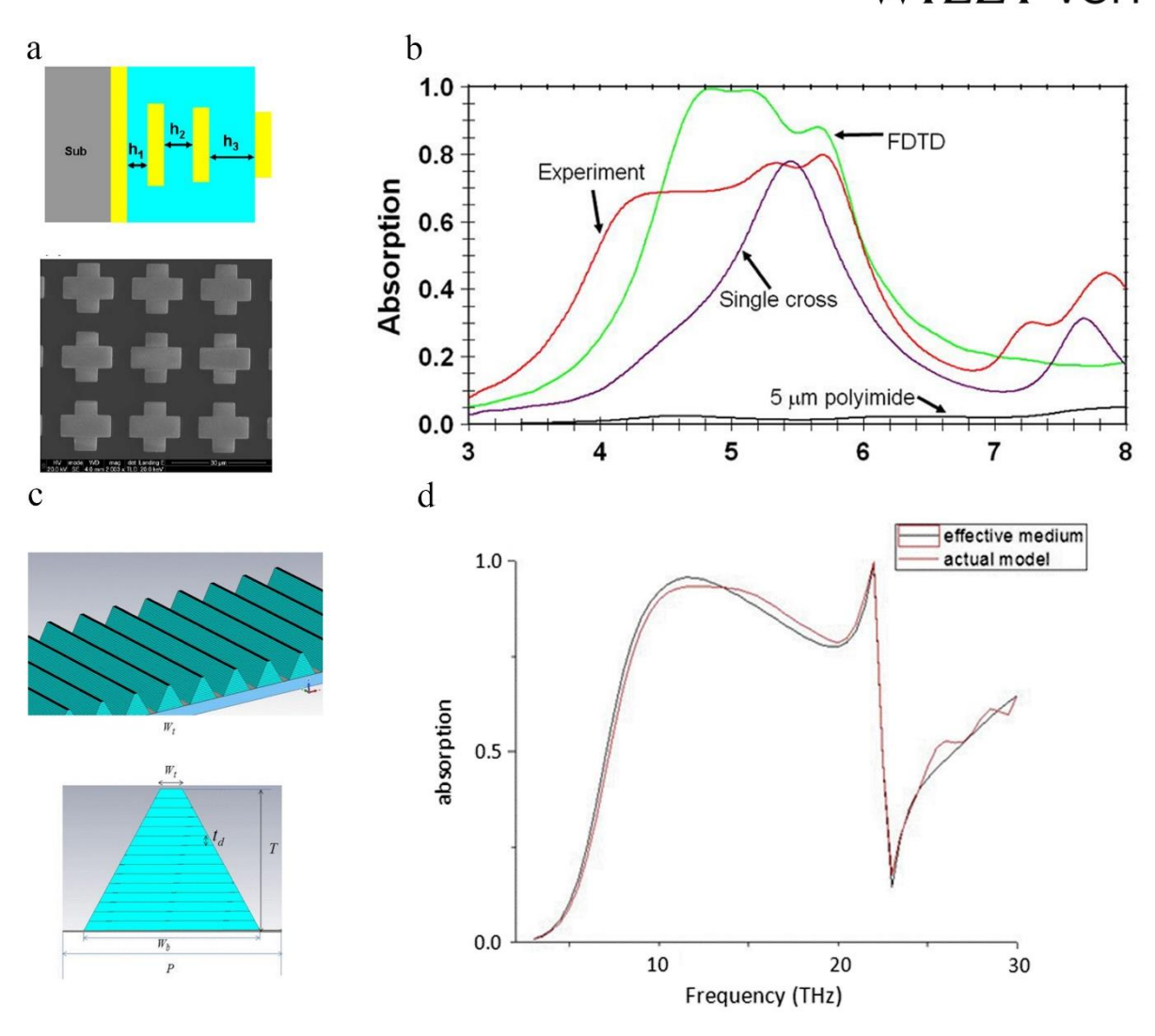


Figure 6. (a) Cross section illustration and SEM image of the complete multilayer absorber; (b) Experimental and simulated data of the multilayer absorber. Also plotted is the experimental absorption spectrum for a single layer absorber. (c) Schematic diagram for a line array of graphene-dielectric multilayered quadrangular pyramidal frustums backed with a homogeneous metal film. A unit cell of the graphene BMMPA is illustrated, with $P = 10 \, \mu m$, $w_b = 8 \, \mu m$, $w_t = 1 \, \mu m$, $t_d = 400 \, nm$ and $T = 6 \, \mu m$. Light with TM polarization is incident along z-direction; (d) Absorption spectra for a graphene-dielectric multi-layered pyramid absorber with N=15 periods and thickness of dielectric layers equal to 400 nm. The red line is the result of the real structure, and the effective homogeneous mode is shown by the black line. a and b: Reproduced from Ref. [89] with permission from Optical Society of America, copyright 2011. c and d: Reproduced from Ref. [74] with permission from IEEE, copyright 2013.

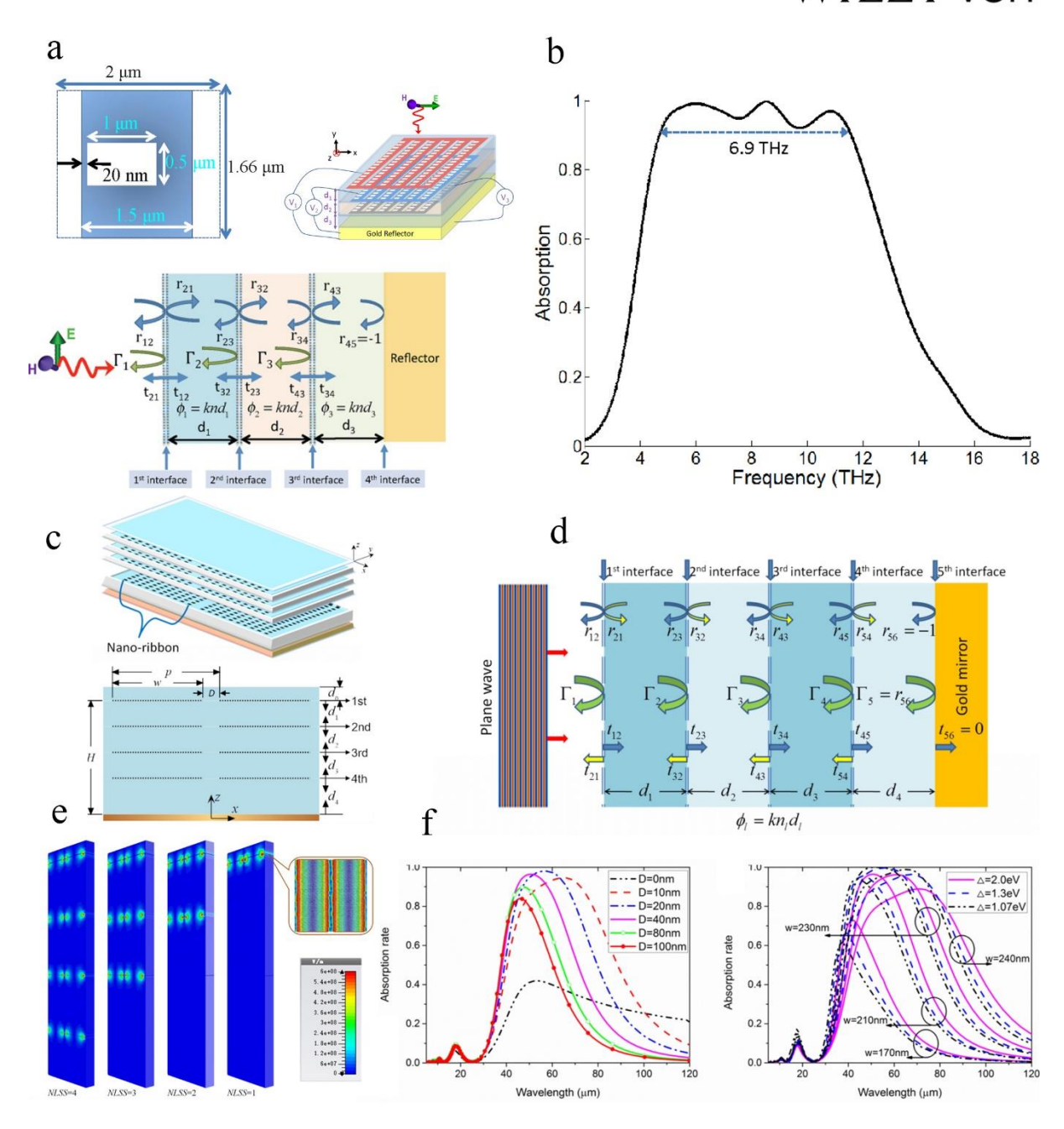


Figure 7. (a) The schematic diagram of the proposed absorber with three layers of graphene (top right); The graphene unit cell with an asymmetric void with its dimensions (top left). Description of the transmission line model for the multilayered absorber (bottom); (b) The absorption spectra of the three-layer design with $d_1 = 0.67 \mu m$, $d_2 = 0.5 \mu m$, and $d_3 = 4.78 \mu m$. (c) Schematic of the proposed sandwich-like structured BP absorber and front view of the proposed absorber with layer dimensions; (d) A schematic diagram of the transmission and reflection for a four-layered sandwich-like BP structure; (e) Simulated average electric field intensity values for monolayer BP MMs with two nanoribbon periods aligned along the x-direction. The inset presents a sectional view at the in-plane across

the 1st interface for NLSS value of 1; (f) Simulated absorption rate spectra for TM polarization at various distances between two nano-ribbons and for various thicknesses of BP in monolayer, bilayer and trilayer with ridges perpendicular to the *x*-direction. **a** and **b**: Reproduced from Ref. [101] with permission from Optical Society of America, copyright 2013. **c-f**: Reproduced from Ref. [75] with permission from Optical Society of America, copyright 2017.

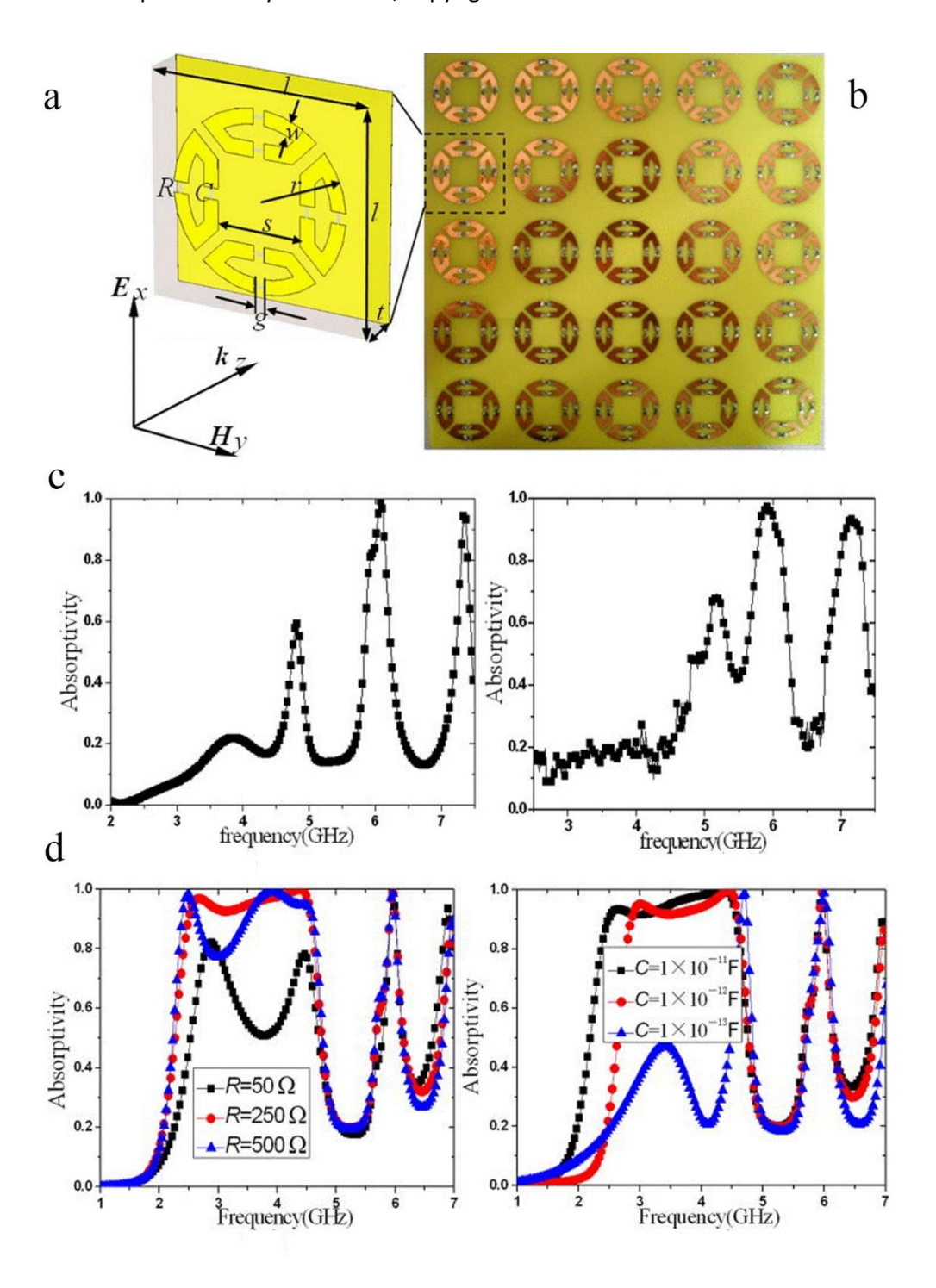


Figure 8. (a) Perspective view of unit cell with indicated TEM wave direction and geometric dimensions and lumped parameters: I = 40 mm, r = 16 mm, s = 15.2 mm, w = 2.7 mm, g = 2 mm, t = 6 mm, C = 4 pF, $R = 249 \Omega$; (b) Photograph of fabricated lumped elements MA sample; Absorptivity of MMPA before introducing without lumped elements: (c) Absorptivity of the simulation (left) and experiment (right) results; Absorptivity of the BMMPA with different values for the lumped elements: (d) Lumped resistance R and lumped capacitance C, respectively. Reproduced from Ref. [105] with permission from AIP publishing, copyright 2012.

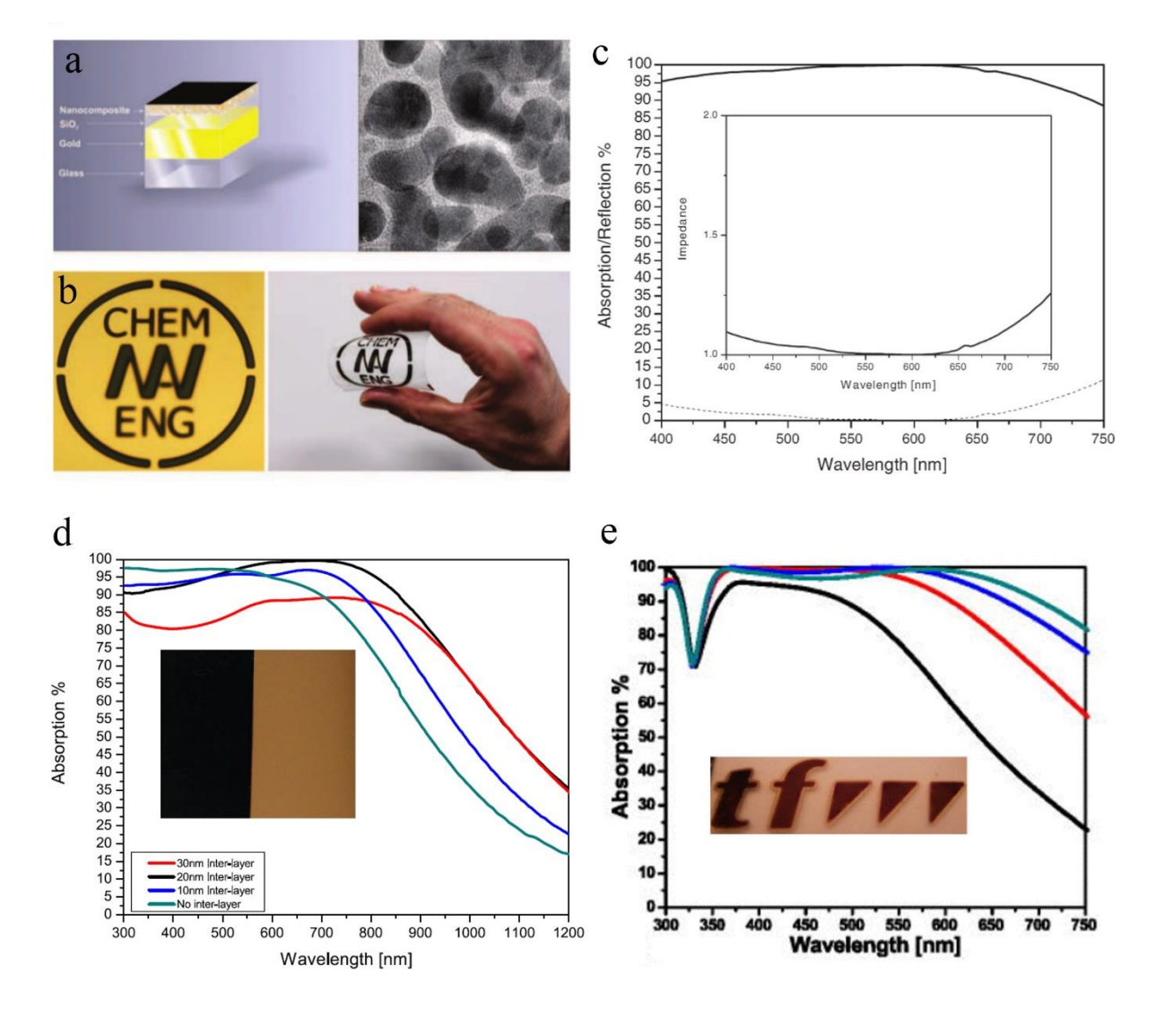


Figure 9. (a) Schematic of a perfect absorber structure manufactured by sputtering. The thickness of the nanocomposite, SiO_2 spacer, and gold mirror layers are 20, 25, and 100 nm, respectively. The left panel illustrates that the whole structure sits on top of a glass substrate; the right panel shows a top-

view TEM image of the nanocomposite film; (b) Perfect absorber (blackbody) coated via mask on gold-coated glass (left) and flexible polymer foil (right). These examples show the potential of the coating for application on different substrates, including flexible ones; (c) Absorption (solid line) and reflection (dashed line) spectra of the system described in panel (a), measured at 6 degree angle of incidence. The inset shows the impedance data of 20 nm Au/SiO₂ nanocomposite deposited on a 100 nm gold film with 25 nm SiO₂ spacer layer. (d) Absorption spectra of 20 nm Cu-PTFE composite on a PTFE spacer layer with different thicknesses, over 100 nm of Cu. The green curve shows the composite on a base layer without any inter-layer for comparison. The inset is the photo of the perfect black absorber (left) in comparison with bare copper film (right). (e) Absorption spectra of a silver-SiO₂ nanocomposite of 15 nm (black curve), 20 nm (red curve), 25 nm (blue curve), and 30 nm (green curve) thickness, deposited on 15 nm of SiO₂ coating a silver mirror. The inset is true color photograph of the perfect absorber coated on transparent polymeric substrate presenting the logo of Faculty of Engineering (TF) of University of Kiel. a-c: Reproduced from Ref. [11] with permission from John Wiley and Sons, copyright 2011. d: Reproduced from Ref. [16] with permission from Springer Nature, copyright 2012. e: Reproduced from Ref. [113] with permission from AIP publishing, copyright 2014.

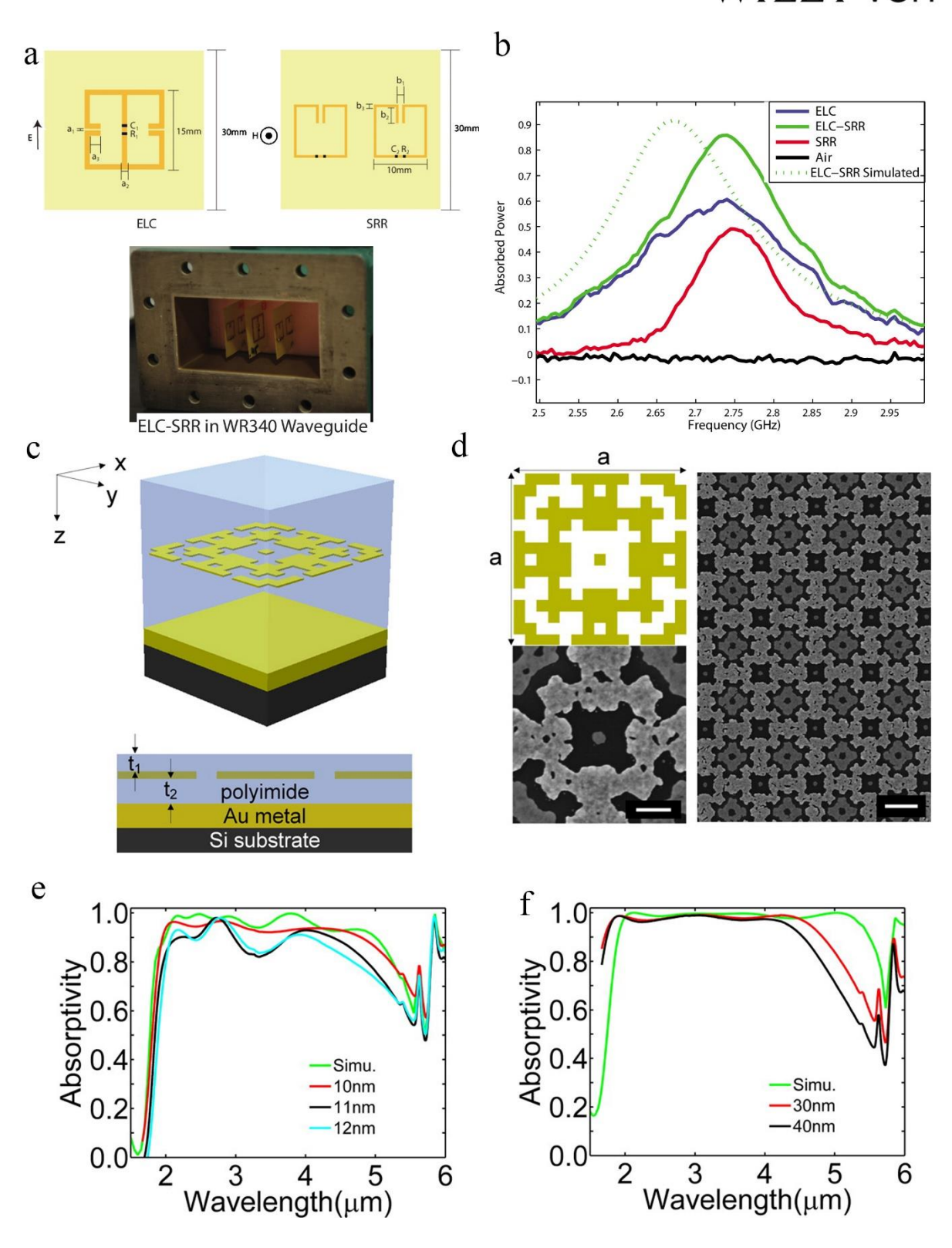


Figure 10. (a) The optimum single-cell ELC-SRR absorption was achieved with ELC parameters of a_1 =0.35 mm, a_2 =1 mm, a_3 =0 mm, a_1 =10 pF, and a_2 =10 pF, and a_2 =10 pF, and a_3 =10 pF, and a_4 =10 pF, and an achieved with ELC parameters of a_4 =10 pF, and a_4

MHz. (c) Diagram of optimized Au-based BMMPA structure; (d) Top left: Top view of one unit cell of the design. Bottom left: FESEM image of a unit cell of the fabricated structure. Scale bar is 200 nm. Right: Low-magnification FESEM image of the same structure. Scale bar is 600 nm; (e) Simulation and measurements for Au-based BMMPA under unpolarized illumination at normal incidence. The average Au thicknesses of the Au nanostructures as determined by atomic force microscopy measurements are 10, 11, and 12 nm; (f) Simulation and measurements for Pd-based MMAs with Pd nanostructure thicknesses of 30 and 40 nm under unpolarized illumination at normal incidence. a and b: Reproduced from Ref. [50] with permission from AIP publishing, copyright 2010. c-f: Reproduced from Ref. [65] with permission from American Chemical Society, copyright 2014.

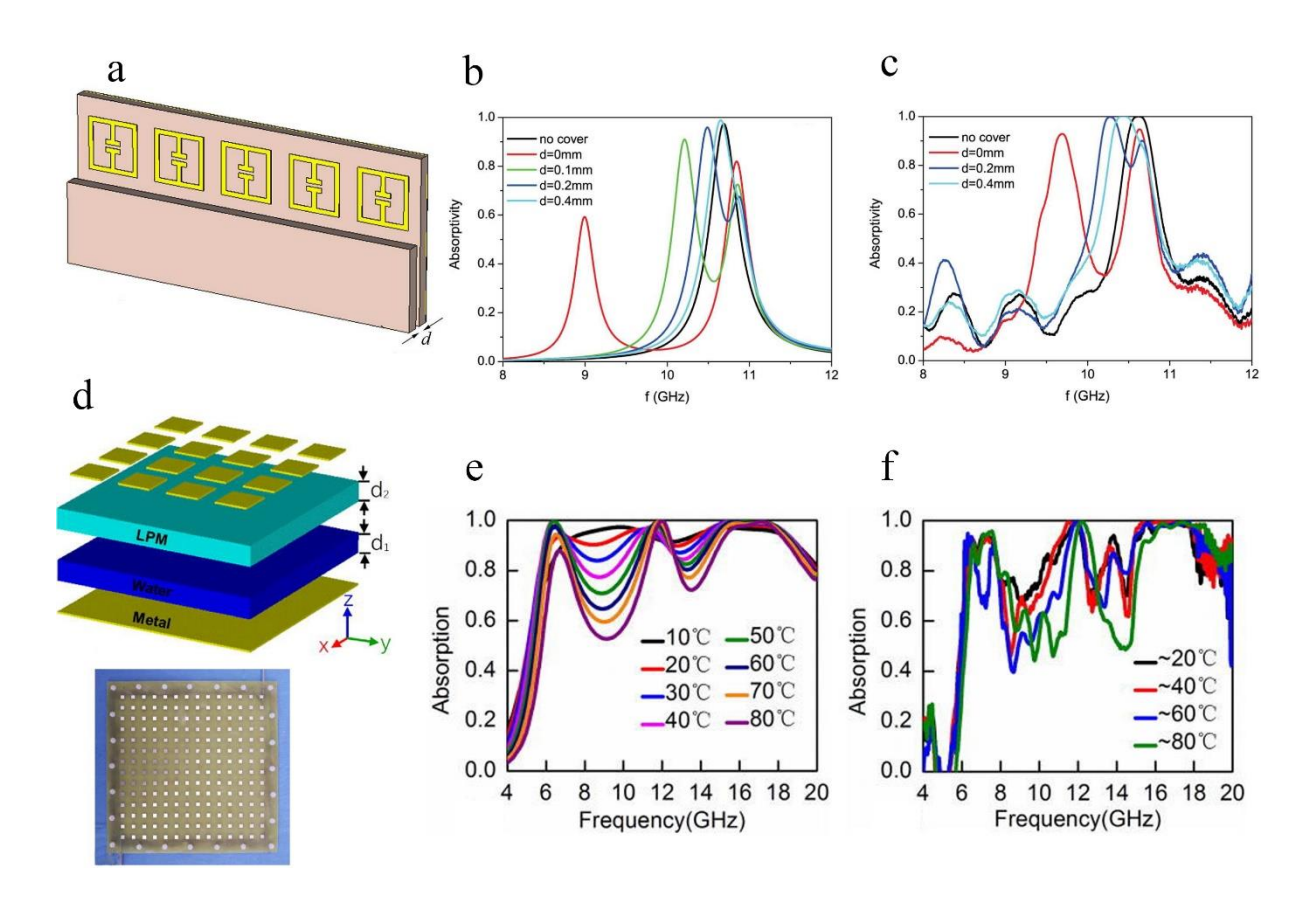


Figure 11. (a) BMMPA with a horizontal half-slab, and (b) theoretical and (c) experimental absorption spectra for different *d*. (d) 3D schematic diagram of the water-substrate BMMPA and optical image of the assembled prototype of the water-substrate BMMPA; (e) Simulated and (f) measured absorption spectra of the fabricated water-substrate BMMPA at different temperatures. **a-c**: Reproduced from

Ref. [118] with permission from Optical Society of America, copyright 2012. **d-f**: Reproduced from Ref. [85] with permission from AIP publishing, copyright 2017.

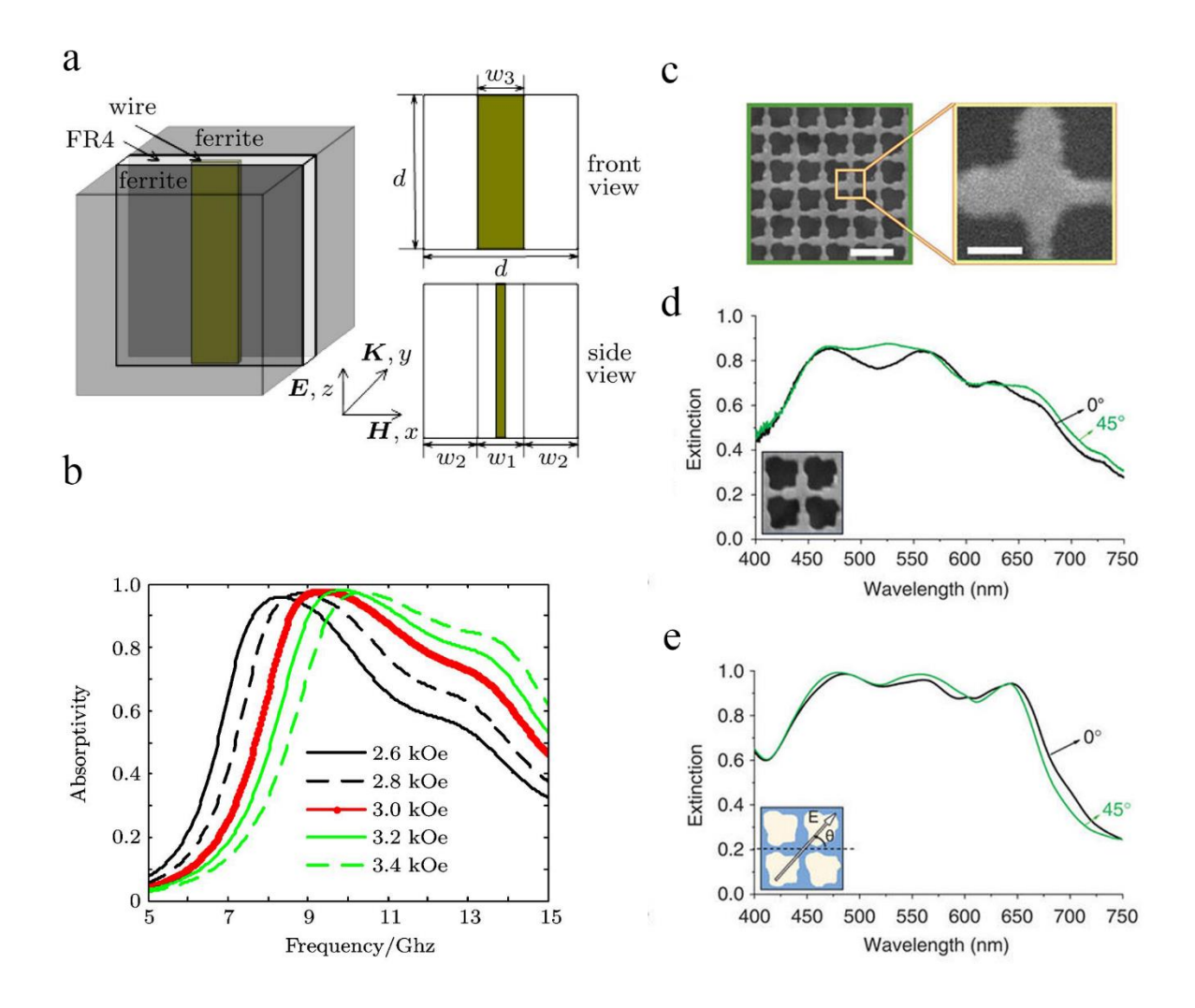


Figure 12. (a) Schematic diagram of the ferrite—wire BMMPA unit cell. Front view, side view, and structure parameters are presented; (b) The absorption band characteristics under different magnetic biases. (c) SEM image of the fabricated crossed trapezoid arrays (left) and a single unit cell of crossed trapezoid (right). Scale bars are 500 and 100 nm, respectively; (d) Measured, and (e) Simulated extinction spectra using digitized SEM images (inset) for different incident electric field polarization angles (inset). a and b: Reproduced from Ref.^[119] with permission from IOP publishing, copyright 2012. c-e: Reproduced from Ref.^[24] with permission from Springer Nature, 2011.

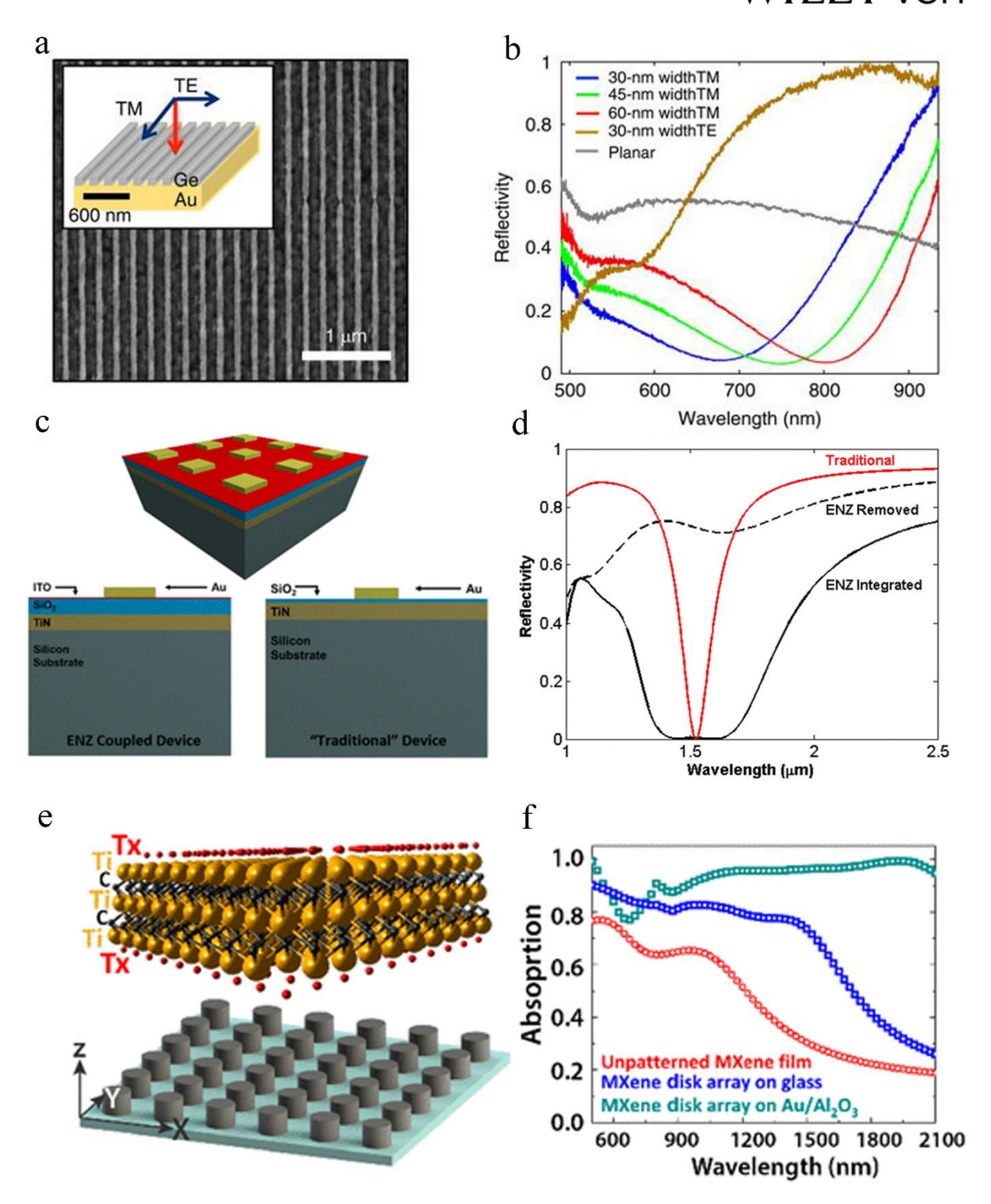


Figure 13. (a) Top-view SEM image of a fabricated metafilm with Ge beams, with a 200-nm-period and 0.3-duty cycle. Scale bar, 1 μ m; (b) Measured reflectivity spectra for TM polarized light for metafilms constructed from nanobeams with a width of 30 (blue), 45 (green) and 60 nm (red). The reflectivity spectra for TE polarized light of the array with 30-nm-wide beams (brown) and a planar Ge film (grey)

are shown for reference. (c) Schematic (top) and cross section of the device consisting of a TiN metallic thick film, a SiO2 dielectric layer, an ITO nanofilm, and a patterned periodic array of metal squares, all on top of a Si substrate, and a schematic of a reference "traditional" perfect light absorber without an ENZ layer; (d) Simulated reflectivity curves for a perfect absorber with integrated ENZ (solid black line), absorber without ENZ layer (dashed black line), and an optimized "traditional" gap-plasmon perfect light absorber without ENZ layer (solid red line). (e) Schematic of the BMMPA fabricated using two-dimensional titanium carbide (Ti3C2Tx) MXene; (f) Comparison of experimental absorption spectra of the two types of disk arrays and unpatterned MXene film (incident light is TE polarized; angle of incidence is 20°). a and b: Reproduced from Ref. [130] with permission from Springer Nature, 2015. c and d: Reproduced from Ref. [122] with permission from American Chemical Society, 2018. e and f: Reproduced from Ref. [177] with permission from American Chemical Society, 2018.

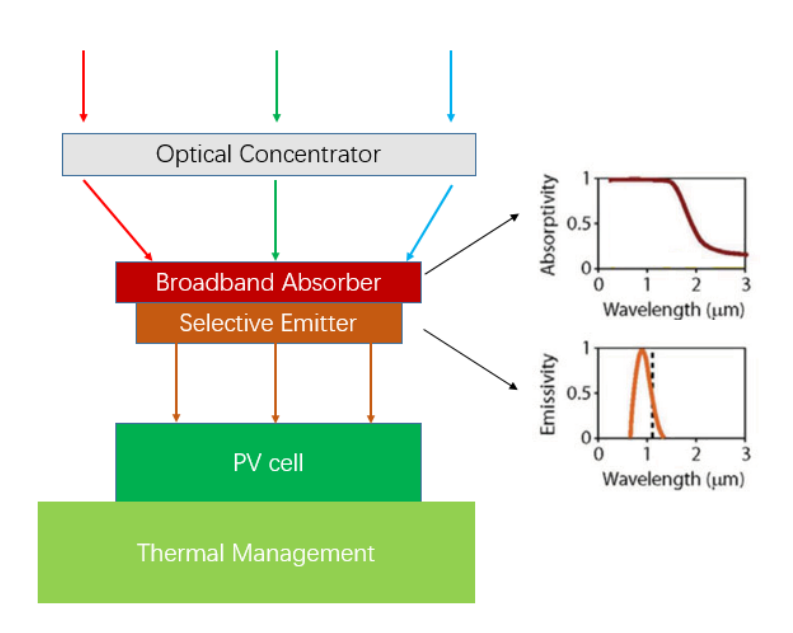


Figure 14. Schematic of STPV systems. The absorber and emitter typically operate above 1000 K while the PV cell operate at room temperature.

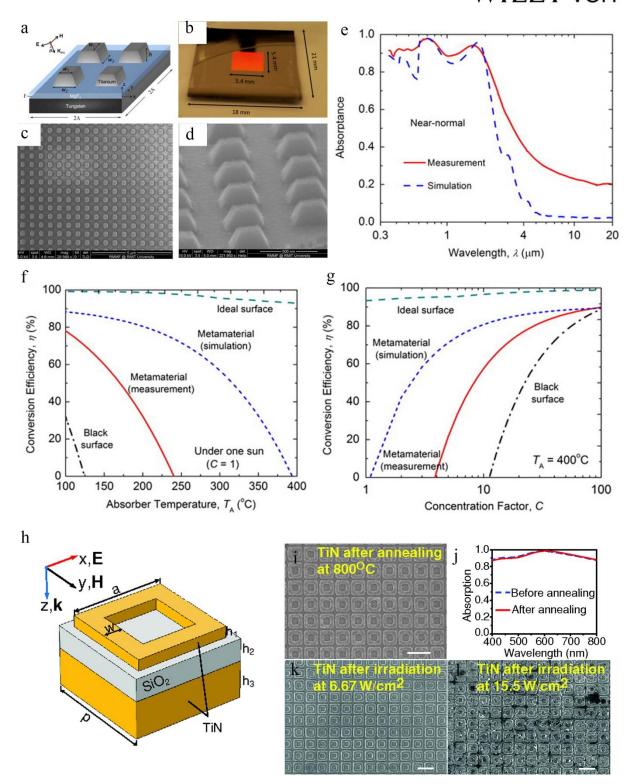


Figure 15. (a) Structure schematic for proposed MM solar absorber. K_{inc} represents the incident wavevector, and the incidence angle θ is defined as the angle between K_{inc} and the surface normal. The plane of incidence (POI) is defined as the xz plane. The E field is in the POI for TM incidence, while it is perpendicular to the POI for TE incidence; (b) A photo of the fabricated sample for optical

characterization. SEM images of the fabricated absorber sample from (c) top view and (d) side view; (e) Measured and simulated room-temperature spectral absorptance of the MM solar absorber; (f) Predicted solar-to-heat conversion efficiencies of an ideal selective surface, the MM solar absorber (with optical properties either measured or simulated), and a black surface as a function of absorber temperature absorber temperature (T_A) under 1 sun; (g) Solar-to-heat conversion efficiency for all three surfaces as a function of concentration factor C at an absorber temperature of T_A =400 °C. (h) Schematic representation of a unit cell of the three-layer TiN MMPA with dimensions of α = 250 nm, w = 50 nm, p = 300 nm, h_1 = 30 nm, h_2 = 60 nm, and h_3 = 150 nm; SEM image (i) and the measured absorption (j) of the TiN absorber after annealing at 800 °C for 8h, as well as the reference measured absorption of TiN before annealing; SEM images for the TiN absorber after being illuminated by a laser with an intensity of 6.67 W/cm² (k) and 15.5 W/cm² (l). a-g: Reproduced from Ref. [64] with permission from Elsevier B.V., copyright 2015. h-l: Reproduced from Ref. [16] with permission from John Wiley & Sons, copyright 2014.

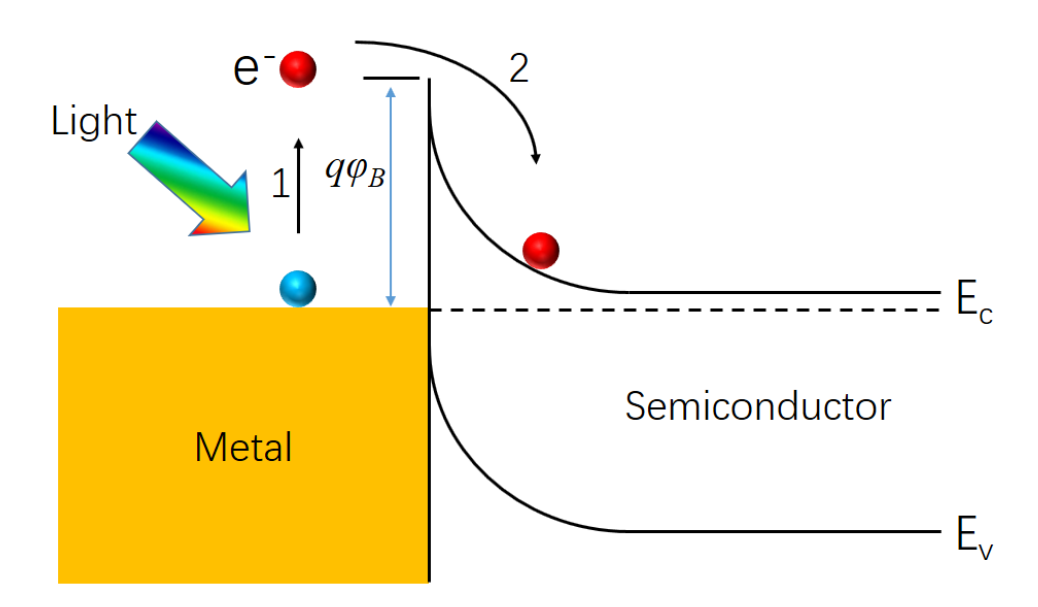


Figure 16. Energy band diagram for plasmonic hot electrons over a metal–semiconductor Schottky barrier, $q\varphi_B$.

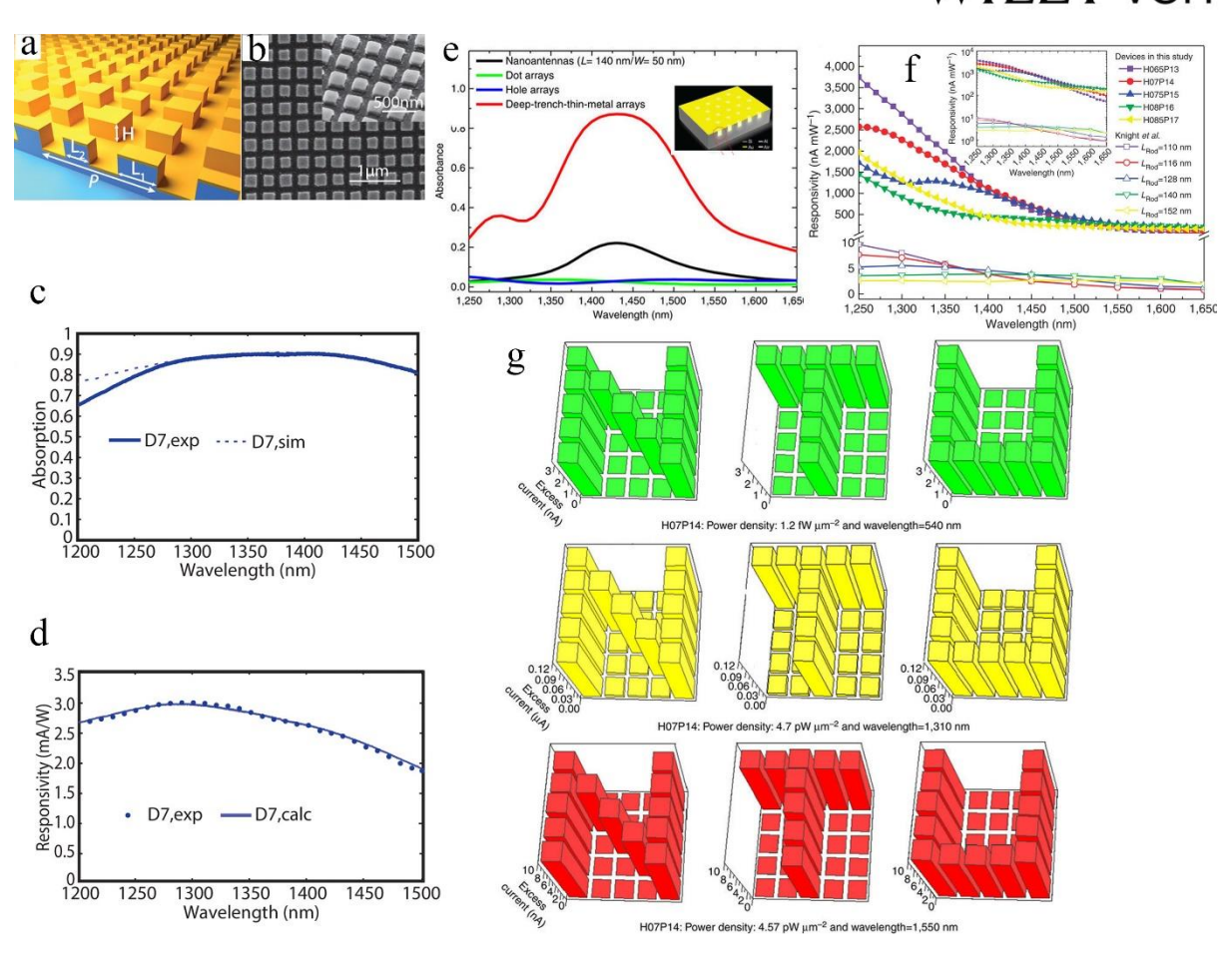


Figure 17. (a) Schematic of the BMMPA photodetector. The dimensions of the photodetector are $L_1 = 185$ nm, $L_2 = 225$ nm, P = 680 nm, H = 160 nm; (b) SEM image of the fabricated device; (c) Experimentally measured (solid) and simulated (dashed) absorption spectra of the BMMPA detector; (d) Experimentally measured (circles) and calculated (line) photoresponsivity spectra of the BMMPA photodetector. (e) Simulated absorption spectra of the four types of antenna structures. Among them, the DTTM arrays exhibited the largest absorption in the broadband regime. The inset is the illustration of the detector structure; (f) Responsivity spectra of the proposed DTTM devices, in comparison with the nanoantenna-based devices reported by Knight *et al.* [150]; (g) Bar charts displaying excess current obtained by the H07P14-containing DTTM device under an applied bias voltage of 0 V, detected at wavelengths of 540, 1310 and 1550 nm. The images were constructed based on the existence or absence of a photocurrent during the point-by-point scanning of the DTTM device. Clear images of the capitalized letters 'NTU' were obtained, even though the incident power density was low; in particular, 4.7 pW/μm² at a wavelength of 1310 nm and 4.57 pW/μm² at a wavelength of 1,550 nm. The pixel size

is 5 mm. **a-d**: Reproduced from Ref. [148] with permission from American Chemical Society, copyright 2014. **e-g**: Reproduced from Ref. [30] with permission from Springer Nature, copyright 2014.

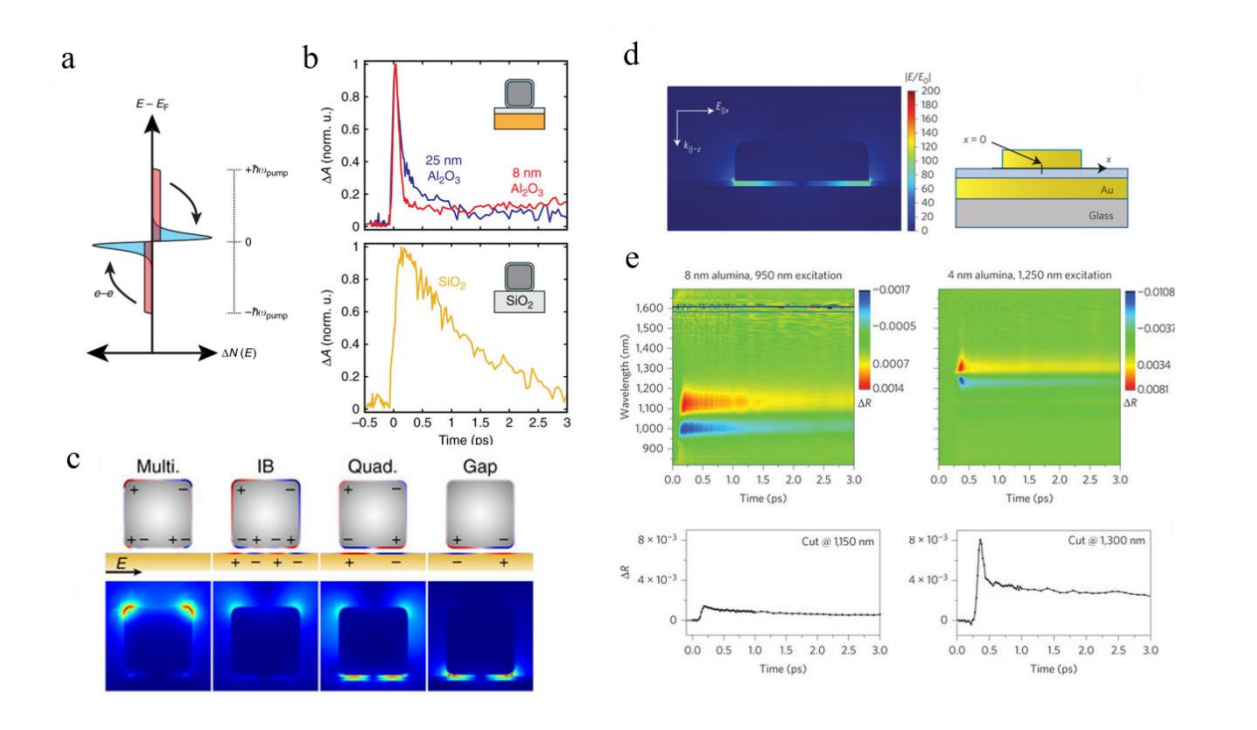


Figure 18. (a) Hot electron distribution from plasmon excitation. Nonthermal (red) carriers initially form a symmetric step-wise distribution relative to the Fermi energy upon excitation. After electron–electron scattering, a thermalized electron population (cyan) with a Fermi–Dirac distribution is formed from the nonthermal electrons, with an electronic temperature above that of the lattice. (b) (top) Kinetic trace of normalized differential absorbance for Ag nanocubes on an 8 nm Al_2O_3 spacer compared to a 25 nm Al_2O_3 spacer at the gap resonance and (bottom) to bare Ag nanocubes on SiO_2 in transmission mode, which exhibits no ultrafast (~100 fs) decay of the response, arising from the relaxation of highly energetic nonthermal carriers. (c) Cross section of the surface charge (top) and electric field profiles (bottom) at the peaks of the interband (IB) transition and plasmon modes for an electric field oriented in-plane. The field strength scale is up to $20 \times$ free space for the multipolar (Multi) mode, IB transition, and quadrupolar (Quad) mode and $100 \times$ free space for the gap mode. (d) (left) Electromagnetic field distribution inside the nanostructure (defined as $|E/E_0|$), showing strong

plasmonic hot spots at the edges of the nanodisk and (right) geometry of the system; (e) Two-dimensional map of the time evolution of the plasmonic spectral change in 8-nm-thick (left) and 4-nm-thick (right) alumina spacer samples, and (bottom) cuts at 1115 nm (left) and 1300 nm (right) showing the time dynamics of the corresponding data in the above panels after excitation of the plasmon. The time dynamics in the 4-nm-thick spacer are drastically different to the thicker spacer, with a new ultrafast component following the excitation near its resonance at 950 nm. **a-c**: Reproduced from Ref. [152] with permission from Springer Nature, copyright 2017. **d** and **e**: Reproduced from Ref. [151] with permission from Springer Nature, copyright 2015.

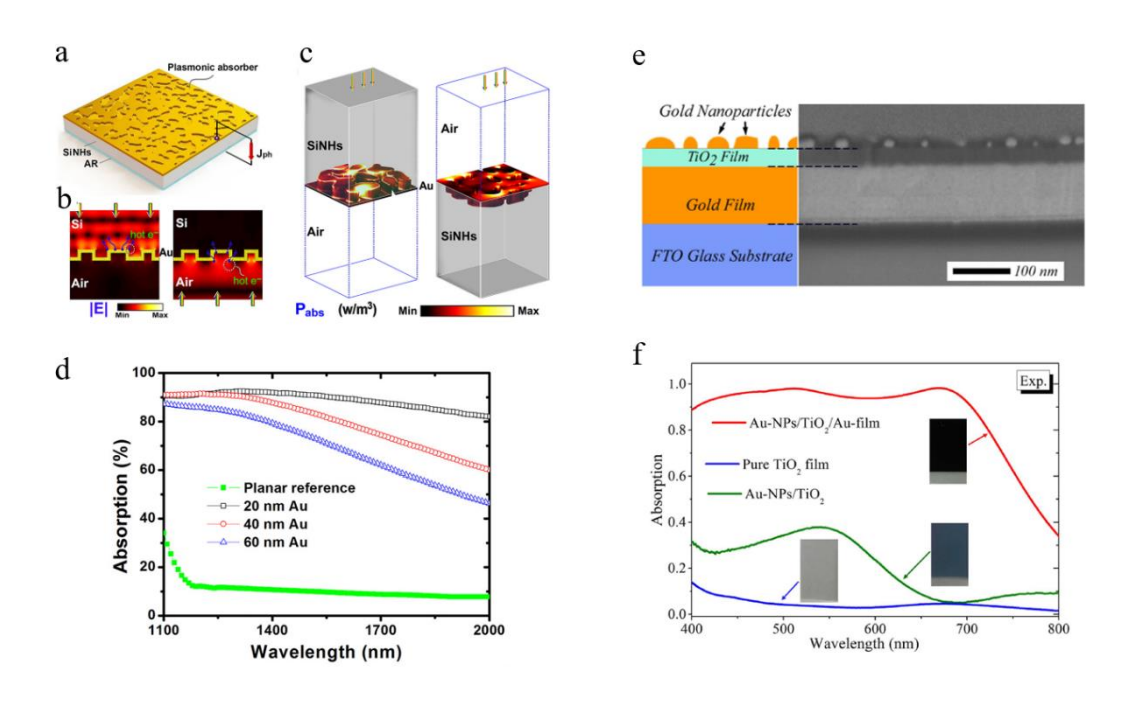


Figure 19. (a) Schematic of the proposed plasmonic hot electron photodetector; (b, c) Field and volumetric power absorption (P_{abs}) distributions of the device operating at the front and back-illumination modes, from simulations replicating a typical morphology of Au/SiNHs from the experiments; (d) Measured absorption spectra under back illumination of the Au/SiNH devices with different thicknesses of Au coatings. The result of a planar reference device with 20 nm thick Au deposited on nonstructured sample is also included. (e) (left) Schematic of the metal-dielectric-metal nanostructure that is composed of (from bottom to the top) a FTO glass substrate coated with an optically thick Au film (~150 nm) followed by a thin TiO_2 film acting as the spacer layer and at the very

top, a monolayer of Au NPs with random size dispersion and spatial distribution. (right) Side-view SEM image of the optimized Au-NPs/TiO₂/Au-film nanostructure prepared with a 5-nm-thick Au film predeposited on a 50-nm-thick TiO₂ spacer layer; (f) Experimentally measured absorption spectra of the Au-NPs/TiO₂/Au-film nanostructure, the pure TiO₂ film, and the Au-NPs/TiO₂ nanostructure. The insets show the photographic images of the prepared samples. **a-d**: Reproduced from Ref. [162] with permission from American Chemical Society, copyright 2017. **e** and **f**: Reproduced from Ref. [159] with permission from Springer Nature, copyright 2016.

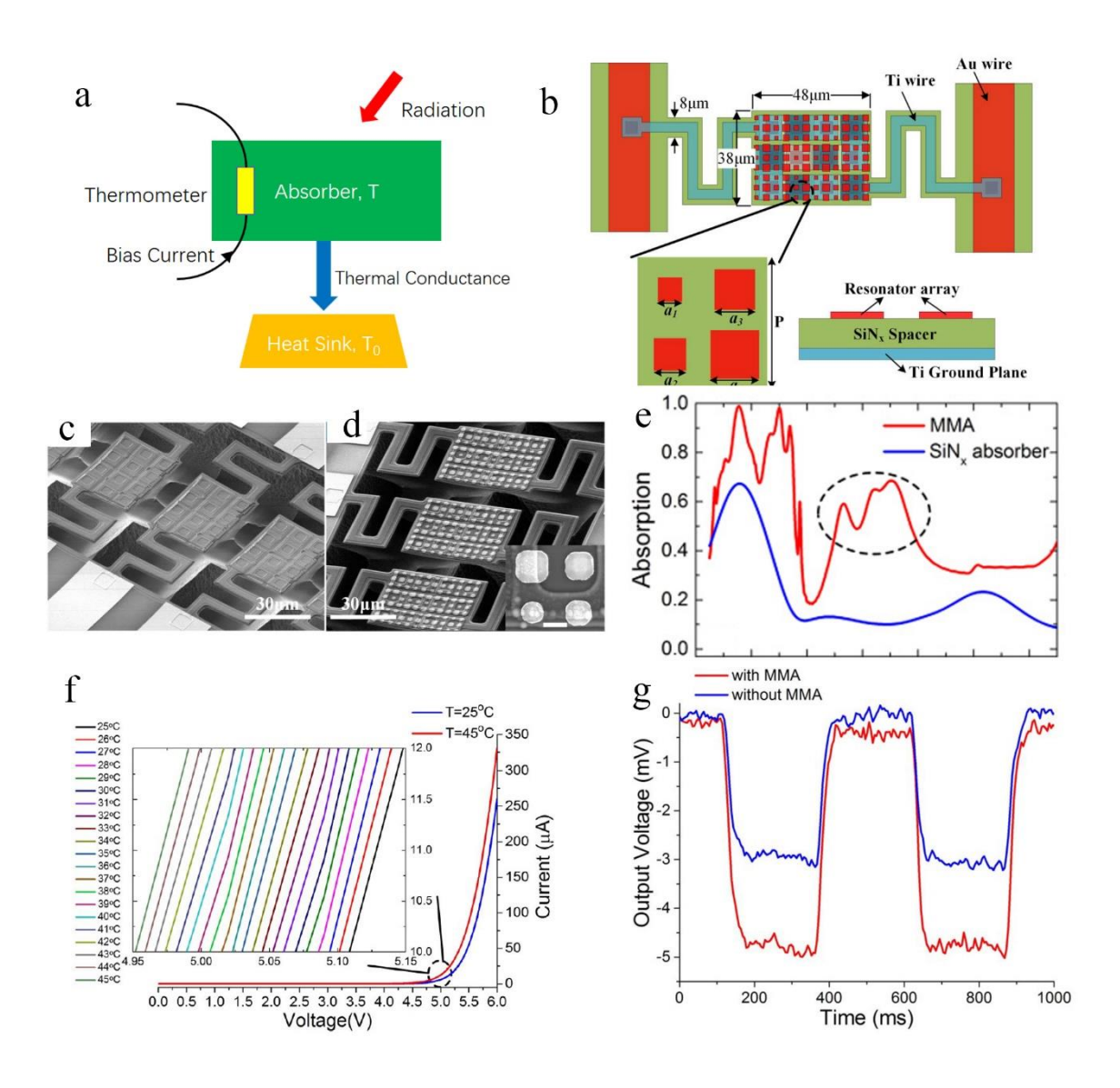


Figure 20. (a) A typical bolometer structure including a BMMPA. (b) Top view of the designed microbolometer; SEM pictures of the fabricated microbolometers (c) without and (d) with BMMPA. The zoomed-in picture in (d) is the unit cell of the resonator array (scale bar: 2 μm); (e) Simulated

absorption of BMMPA and the ordinary SiNx absorber; (f) I-V characteristics of the fabricated microbolometer at the two different device temperatures of 25°C and 45°C, respectively. The inset is the zoomed-in view of different I-V curves with a 1°C step around a 10 μ A bias; (h) Transient responses of the microbolometers under modulated IR incidence at a bias current of 10 μ A. **b-g**: Reproduced from Ref. [167] with permission from Optical Society of America, copyright 2016.

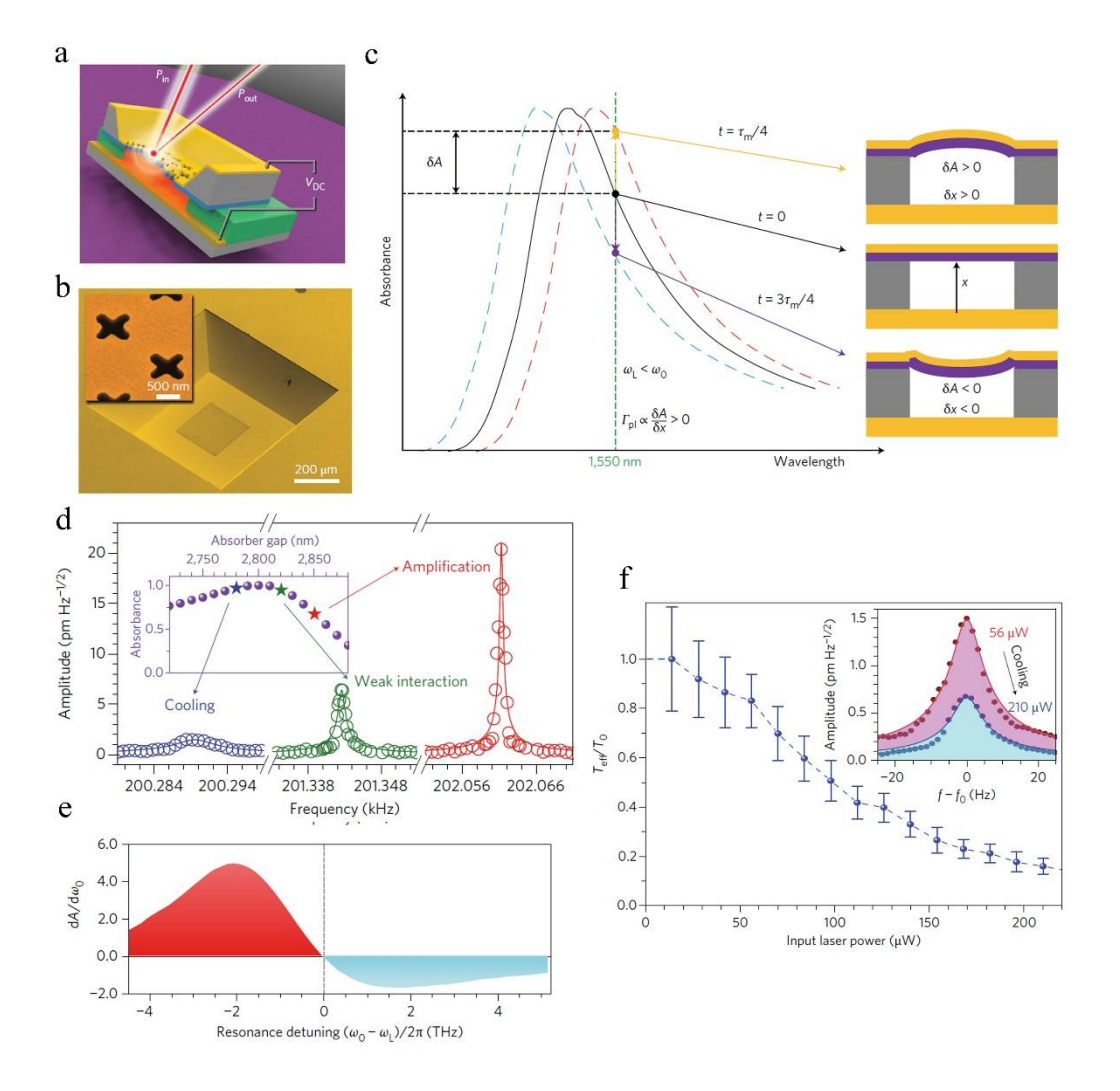


Figure 21. (a) Schematic of a MMPA with a mechanically compliant bilayer (Au (25 nm)/SiN (100 nm)) membrane component decorated with a nanoantenna array; (b) The false-color SEM image of the fabricated cross-shaped nanoslot (length (360 nm)/width (150 nm)) antenna array (period 800 nm) that covers an area of 250 μm by 250 μm at the center of the 500 μm by 500 μm membrane. Inset: close-up SEM of the array; (c) Plasmomechanical coupling: when the MM is illuminated with a pump laser at ω_L corresponding to a wavelength of 1,550 nm, tuned slightly to the red side of the Fano

resonance frequency ω_0 , the natural oscillation of the membrane of amplitude δx at its mechanical resonance frequency $(1/\tau_m)$ leads to a dynamic modulation of total absorbance (δA). As δA varies between positive and negative values, this leads to a dynamic modulation on the thermal expansion of the membrane. As illustrated here for positive resonance detuning, i.e., $\omega_L < \omega_0$, the light-induced mechanical damping $\Gamma_{\rm pl} \propto \delta A/\delta x$ is always positive, which dampens the mechanical resonance; (d) The thermomechanical Brownian noise spectra for the fundamental mechanical resonance measured at a pump power of ~17 μW for different absorber gap values corresponding to weak (unperturbed), positive (amplification) and negative (cooling) absorption-induced forces. The inset shows the MM absorbance as a function of absorber gap at 1,550 nm pump wavelength near the Fano resonance; (e) Differential spectral absorbance ($dA/d\omega_0$) versus the detuning between the Fano resonance frequency (ω_0) and the fixed 1,550 nm pump laser frequency (ω_L) ; (f) The effective temperature $T_{\rm eff}$ of the fundamental mechanical mode is proportional to the area under its peak thermomechnical noise spectrum, exemplified in the inset. The absorber gap has been tuned at 5.5 V, corresponding to the maximum $|dA/d\omega_0|$ on the red side of the Fano resonance. At 210 μW pump power, $T_{\rm eff}$ for the Brownian motion of the mechanical mode is reduced below 50 K from room temperature (T_0 =300 K). Reproduced from Ref. [18] with permission from Springer Nature, copyright 2016.

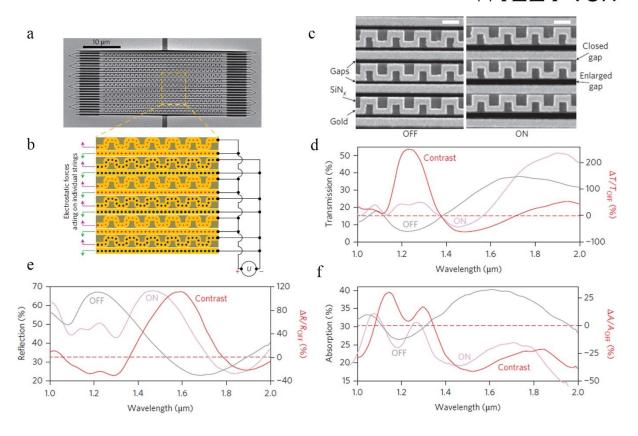


Figure 22. (a) SEM image of the device; (b) Schematic of the driving circuit (black) and a section of the MM pattern consisting of a gold nanostructure (yellow) supported by silicon nitride strings (brown). The driving voltage *U* causes positive (red) and negative (blue) charging and thus electrostatic forces acting in opposite directions (pink and green); (c) SEM images of the MM in its OFF and ON states. Scale bar, 500 nm; Transmission (d), reflection (e) and absorption (f) spectra of the device in the OFF and ON states (left axis) and the corresponding switching contrast (right axis). Reproduced from Ref.

Table 1 Metal and dielectric choice in BMMPA design

Metal	Dielectric

		,,,	
Ag	[24, 26]	Ge	[39, 78]
Au	[6, 9, 10, 21, 29, 39, 58, 59]	Si	[30]
Cu	[37, 60, 61]	SiC	[79]
Al	[62]	ZnS	[39, 80]
Мо	[35]	FR-4	[37, 50, 54, 61, 81, 82]
W	[63]	SiN	[18] [83]
Ti	[64]	GaAs	[39]
Pd	[65]	SiO ₂	[11, 35, 58, 60, 84]
Cr	[66, 67]	Al_2O_3	[6, 9]
Ni	[68]	MgF_2	[10, 29, 73]
Та	[68]	Water	[85]
ITO	[69]	TMM4	[86]
TiN	[16]	Kapton	[21]
AZO	[68]	Epoxy glass	[87]
Ta ₂ N ₃	[70]	Polyimide	[88] [59, 62, 89]
Graphene	[14, 71-74]	Photoresist SU-8	[66]
Black phosphorus	[75]	Benzocyclobutane	[33]
Nanocomposite	[11, 76]	Polydimethylsiloxane (PDMS)	[90]
$Ti_3C_2T_x$	[77]	Polytetrafluoroethylene (PTFE)	[11, 76]
		Polyethylene glycol terephthalate	(PET) [69]
		Liquid crystal 4'-n-pentyl-4-cyano	biphenyl ^[15]

Method Mechanism		Working frequency	Fabrication	Cost	_
Planar arragement	Merge peaks	UV to GHz	Easy or Hard	Depends	_
Vertical stacking	Merge peaks or slowlight waveguide modes	UV to GHz	Hard	High	
Welding lumped elements	Reduce Q-factor	Only GHz	Easy	low	
Using nanocomposites	Plasmonic effect	UV to NIR	Easy	low	

Table 3. A summary of methods to achieve BMMPA; NR is not reported and NA is not applicable in the table.

Methods	FWHM	Operating frequency	Resonator	Resonator material	Dielectric material	Average absorption (%)	Ref.
	2.16 μm	3–5 μm	Cross	Gold	SiO ₂	≥ 50	[58]
	1.15 THz	6.24-7.04 THz	Square	Copper	SiO ₂	~ 90	[60]
	2.8 GHz	9–13 GHz	Circle	Copper	Epoxy glass	≥95	[87]
	NR	0.5–0.7 μm	Square hole	Gold	SiO ₂	> 95	[92]
Horizontal	NR	9.79–11.72 GHz	Dendritic	NR	FR-4	≥90	[55]
integration	NR	8.3–17.4 GHz	Windmill	ITO	PET&PMMA	≥90	[69]
	NR	0.65–1.45 THz	SRR & disk	Gold	PDMS	≥80	[90]
	5.66 GHz	12.38–22.28 GHz	SRR & SMP	Copper	FR-4	≥ 60	[82]
10.1 THz	31.0–37.0 THz	Circle	Gold & Graphene	Polyimide	≥ 90	[71]	
	2.3 GHz	8.8–10.8 GHz	Ring	Copper	FR-4	≥80	[95]
	1.72 μm	3.0–5.5μm	Sawtooth slab	Gold	Germanium	≥95	[78]
	NR	8.37–21 GHz	Loop	Copper	TMM4	≥ 90%	[86]
Vertical stacking NR 8–100 THz NR 46.2–62.8µ	2.40 THz	4.08-5.94 THz	Cross	Gold	Polyimide	≥ 60	[89]
	NR	8–100 THz	Frustum pyramid	Graphene	n=3 ^{1/2}	~ 90	[74]
	46.2–62.8μm	Ribbon	ВР	n=1.7	≥90	[75]	
	4–12 THz	Asymmetric void	Graphene	n=2.5 ^{1/2}	≥ 90	[101]	
	700 MHz.	2.2-3.0 GHz	ELC-SRR	Copper	FR4	≥ 60	[50]
1.38 GHz > 4.56 GHZ Welded with lumped elements NR	1.38 GHz	3.1–5.6 GHz	Split-coin	Copper	FR4	≥90	[105]
	8.87–16.47 GHz	Double-circle ring	Copper	FR4	≥ 90	[131]	
	7.93–17.18 GHz	Double octagonal rings	Copper	PEC	≥90	[106]	
	NR	8.45–9.3 GHz 9.2–10.45 GHz	Jerusalem-cross	Conductor	FR4	≥ 90	[110]
	NR	400–2500 nm	NA	Ag NPs	Teflon AF*	≥ 60	[114]
Nanocomposite	NR	Visible range	NA	Au NPs	SiO ₂	~ 100	[11]

	NR	Visible range	NA	Cu NPs	PTFE	≥ 97.5	[76]
СММ	NR	1.3–2.5 μm	Sheet with square hole	Molybdenum	SiO ₂	NR	[35]
GA	NR	1.77–4.81 μm	GA-based	Palladium	Polyimide	≥ 98	[65]
Fractal space-filling curve	1.3 THz	0.5–1.8 THz	Hilbert curve	Aluminium	n=3 ^{1/2}	≥ 90	[123]
Resonator material tailoring	> 1.55 μm	500-2500nm	Disk	Titanium Carbide	Al_2O_3	~ 90	[77]
Crossed trapezoidal arrays	NR	400–700 nm	Crossed trapezoid	Silver	SiO ₂	≥71	[24]
Lossy metal	1.94 THz	1.0-2.43 THz	Ring	Chromium	Polyimide	≥90	[67]

Vitae



Peng Yu is currently a Ph.D. researcher in group of Prof. Zhiming Wang in the Institute of Fundamental and Frontier Sciences of University of Electronic Science and Technology of China. He obtained his bachelor's degree in Microelectronics in 2012 and master's degree in Electronic Information Materials and Components in 2015. His current research interests include metamaterial absorber, quantum dot photovoltaic devices, plasmonic applications.



Lucas V. Besteiro is a joint Postdoctoral Fellow of the Institute of Fundamental and Frontier Sciences of University of Electronic Science and Technology of China (UESTC) and the Institut National de la Recherche Scientifique - Énergie, Matériaux et Télécommunications (INRS-EMT). He performs theoretical research in the fields of plasmonics and nanophotonics, and his current research interests

include hot carrier generation in plasmonic nanostructures, photonic metamaterials, circular dichroism spectroscopy and the fundamental physics of light-matter interaction in the nanoscale.



Dr. Yongjun Huang received the M.S. and Ph.D degrees from the University of Electronic Science and Technology of China (UESTC), Chengdu, China, in 2010 and 2016 respectively. From 2013 to 2015, he was a visiting scholar with the Solid-State Science and Engineering, and Mechanical Engineering, Columbia University, New York City, NY, USA, and a visiting project scientist with the Electrical Engineering, University of California at Los Angeles (UCLA), Los Angeles, CA, USA. He has been an assistant professor with UESTC since Feb. 2017. His research interests include plasmonic metamaterials, the applications for wavefront controling, and photonic crystal based cavity optomechanics.



Jiang Wu received his B.S. degree from University of Electronic Science and Technology of China, and M.S. and Ph.D. degrees from the University of Arkansas-Fayetteville, USA, in 2008 and 2011 respectively. He is currently a full professor in the Institute of Fundamental and Frontier Sciences of University of Electronic Science and Technology of China (UESTC). His research interests include Molecular Beam Epitaxy growth and optoelectronic devices, including photovoltaic cells, lasers, photodetectors and metamaterial absorber.



Dr. Lan Fu received MSc degree from the University of Science and Technology of China in 1996 and PhD degree from the Australia National University in 2001. Dr. Lan Fu is currently an Associate Professor at the Dept. of Electronic Materials Engineering, Research School of Physics and Engineering, ANU..



Hoe Tan is a Senior Fellow with the Department of Electronic Materials Engineering in the ANU College of Physical and Mathematical Sciences. His research interests include: epitaxial growth of low dimensional semiconductor structures and device; ion implantation of semiconductors for optoelectronic applications; and device fabrication/processing and testing/characterisation of optoelectronic devices.



Chennupati Jagadish is currently a Distinguished Professor and Head of Semiconductor Optoelectronics and Nanotechnology Group in the Department of Electronic Materials Engineering, Research School of Physical Sciences and Engineering, the Australian National University. He received the bachelor's degree in 1977, the master's degree in 1980 and the M.Phil. and Ph.D. degrees in 1982 and 1986, respectively. He did post-doctoral research in 1988-90. His research interests covering compound

semiconductor nanotechnology, compound semiconductor materials science and high efficiency compound semiconductor photovoltaics.



Zhiming Wang is currently a professor in the Institute of Fundamental and Frontier Sciences of University of Electronic Science and Technology of China. He obtained his bachelor's degree in Applied Physics in 1992, his master's degree in Semiconductor Physics in 1995, and his Ph.D. degree in Condensed Matter Physics in 1998. He did postdoctoral studies in Paul-Drude-Institute for Solid State Electronics in 2000. His current research interests focus on epitaxial crystal growth, molecular beam epitaxy, quantum dots, surface, interface, nanostructures, nanoscience and nanotechnology



Alexander O. Govorov is a Distinguished Professor of Theoretical Physics at Ohio University in Athens, United States. He received his PhD in 1991 from the Institute of Semiconductor Physics in Novosibirsk, Russia. In 2001 he moved to the U.S. and joined Ohio University. His research focuses on the theory of optical and electronic properties of nanostructures, metamaterials and bio-assemblies.